DEVELOPMENT OF ULTRA-SENSITIVE FLUIDIC SENSORS AND MOLECULAR DYNAMICS STUDIES OF ION AND WATER DISTRIBUTION IN NANOCHANNELS

By

Dongyan Xu

Dissertation

Submitted to the Faculty of the

Graduate School of Vanderbilt University

in partial fulfillment of the requirements

for the degree of

DOCTOR OF PHILOSOPHY

In

Mechanical Engineering

August, 2008

Nashville, Tennessee

Approved:

Professor Deyu Li

Professor Leonard C. Feldman

Professor Yongsheng Leng

Professor Ronald D. Schrimpf

Professor Greg Walker

ACKNOWLEDGEMENTS

I am grateful to all of those who made this dissertation possible. First and foremost, I would like to express my sincere gratitude to my advisor, Dr. Deyu Li, for his guidance and help during my whole Ph.D. period. Appreciation also goes to other members of my dissertation committee, especially Professor Leonard C. Feldman for his guidance and valuable discussions on the experimental work of developing fluidic sensors, Dr. Yongsheng Leng for his instruction on the molecular dynamics simulation work, and I would also like to thank Professor Ronald D. Schrimpf for valuable discussions about the MOSFET, Dr. Greg Walker for his disclosure of high performance computing in engineering. In addition, I want to thank Professor Dongqing Li for allowing me to do experiments in his laboratory. Valuable help from fellow graduate students Manoj Sridhar, Yuejun kang, Saumitra K. Vajandar, Yaonan Wang, Xudong Wu, Jiashu Sun, and Scott Waltermire is also highly appreciated.

This work would not have been possible without the financial support from NSF (Award # CTS-0507903 and CBET-0645383). A portion of this work was conducted at the Center for Nanophase Materials Sciences, which is sponsored at Oak Ridge National Laboratory by the Division of Scientific User Facilities, U.S. Department of Energy.

TABLE OF CONTENTS

Page

LIST OF TABLES

LIST OF FIGURES

LIST OF NOMENCLATURE

A_{ClH}	parameter in the interaction potential between Cl and H atoms
A_{ClO}	parameter in the interaction potential between Cl and O atoms
A_F	amplification factor from the nanofluidic sensor
A_M	amplification factor from the MOSFET in sub-threshold regime
A_{NaH}	parameter in the interaction potential between Na and H atoms
A_{NaO}	parameter in the interaction potential between Na and O atoms
A_1	amplification factor from the fluidic circuit
A_2	amplification factor from the MOSFET in saturation regime
A_3	amplification factor from the MOSFET in sub-threshold regime
a	coefficient constant in Eq. (2.8)
$\mathbf{a}$	acceleration vector
b_{ClH}	parameter in the interaction potential between Cl and H atoms
b_{ClO}	parameter in the interaction potential between Cl and O atoms
b_{NaH}	parameter in the interaction potential between Na and H atoms
b_{NaO}	parameter in the interaction potential between Na and O atoms
C_{bulk}	ion concentration in the bulk region
C_{ClO}	parameter in the interaction potential between Cl and O atoms
C_{NaO}	parameter in the interaction potential between Na and O atoms

C_{Na^+}	concentration of Na^+ ions in the nanochannel
C_{Cl^-}	concentration of Cl^- ions in the nanochannel
D	diameter of a cylindrical pore or constant in the Lennard-Jones potential
D_{NaO}	parameter in the interaction potential between Na and O atoms
d	diameter of a non-conducting sphere
d_{ox}	thickness of the MOSFET gate oxide
E	constant in the Lennard-Jones potential
f	fraction of the volume occupied by spheres in the suspension
$\mathbf{f}_i$	force on atom i
I	baseline ionic current
I_D	drain current of the MOSFET
I^*	ionic current with a particle in the sensing aperture
ΔI	change of the ionic current
k	Boltzmann's constant
k_{sat}	coefficient constant for the MOSFET in saturation regime
k_{sub}	coefficient constant for the MOSFET in sub-threshold regime
$\mathbf{k}$	a vector in reciprocal space
L	length of a cylindrical pore or length of the simulation box
L_D	extrinsic Debye length
L_x	length of the simulation box in the x direction
L_y	length of the simulation box in the y direction

L_z length of the simulation box in the z direction

m_i mass of atom i

N total number of atoms in a molecular system

$\mathbf{n}$ lattice vector

q elementary electric charge

q_i charge on atom i

q_j charge on atom j

R electrical resistance of the pore containing the pure solution

R_A electrical resistance of the microchannel connecting to reservoir A

R_D electrical resistance of the microchannel connecting to reservoir D

R_c cutoff radius

R_e parameter in the interaction potential between Cl and H atoms

R_s skin radius

R_t total resistance

R_1 electrical resistance of the connecting microchannel on the right side

R_2 electrical resistance of the connecting microchannel on the left side

R' electrical resistance of the pore containing a non-conducting sphere

ΔR increase in electrical resistance of the sensing pore

r_i coordinates of atom i

r_{ij} separation between atoms i and j

r_j coordinates of atom j

r_k coordinates of atom k

r_N coordinates of the atom with a rank of N

r_1 coordinates of the atom with a rank of 1

r_2 coordinates of the atom with a rank of 2

$\mathbf{r}$ position vector

$\mathbf{r}_i$ position vector of atom i

T temperature

T_0 prescribed temperature of the system

t time

δt time step

V applied voltage across the aperture or potential energy function

V_{DS} drain-source bias

V_{FB} flat-band voltage

V_G gate potential of the MOSFET without a particle in the sensing channel

V_G^* gate potential of the MOSFET with a particle in the sensing channel

ΔV_G change of the gate potential

V_T threshold voltage of the MOSFET

V_+ positive bias applied at one end of the fluidic device

V_- negative bias applied at the other end of the fluidic device

v^C Coulomb potential

v_1 potential in an external field

v_2 pair potential

v_2^{LJ} Lennard-Jones potential

v_3 three-body potential

$\mathbf{v}$ velocity vector

Z z coordinate

z z coordinate

Greek Symbols

α Ewald convergence parameter

ε_{ij} depth of the potential well between atoms *i* and *j*

ε_{ii} depth of the potential well of atom *i*

ε_{jj} depth of the potential well of atom *j*

ε_{ox} permittivity of the oxide

ε_{s} permittivity of the semiconductor

ϕ^{LJ} Lennard-Jones potential

ϕ_{ClH} interaction potential between Cl and H atoms

ϕ_{ClO} interaction potential between Cl and O atoms

ϕ_{NaH} interaction potential between Na and H atoms

ϕ_{NaO} interaction potential between Na and O atoms

λ scaling factor

θ angle between the normal vector of the lower plate and the dipole momentum of the water molecule

ρ resistivity of the electrolyte

ρ_{eff} effective resistivity

σ standard deviation of the diameter of microbeads or standard deviation of the drain current modulation of the MOSFET

σ_{ij} effective diameter between atoms *i* and *j*

σ_{ii} effective diameter of atom *i*

σ_{jj} effective diameter of atom *j*

$\sigma_{\max}$ maximum of the effective diameters for all atom pairs in the system

σ_s surface charge density

τ coupling time constant

ψ_S surface potential of the MOSFET electronic channel

Subscripts and superscripts

A reservoir A

bulk bulk electrolyte

C Coulomb

ClH between Cl and H atoms

ClO between Cl and O atoms

Cl^- chlorine ion

c	cutoff
D	drain terminal of a MOSFET or Debye or reservoir D
DS	drain-source
eff	effective
F	fluidic device
FB	flat-band
G	gate
LJ	Lennard-Jones
max	maximum
N	number of atoms in the system
NaH	between Na and H atoms
NaO	between Na and O atoms
Na^+	sodium ion
ox	oxide
S	surface
s	surface or skin or semiconductor
sat	saturation
sub	sub-threshold
T	threshold
t	total
x	x direction

y	y direction
z	z direction
0	prescribed
+	positive
-	negative

CHAPTER I

INTRODUCTION

Resistive Pulse Sensing

The Coulter counter, first invented by W. H. Coulter in 1948 and formally patented in 1953 (Coulter, 1953), is a commercially available device used to count and size biological cells and other small particles suspended in a conducting fluid. Conventional Coulter counters operate based on the resistive pulse sensing principle and is able to detect particles with a diameter in the wide range of 0.4 μm to 1200 μm (Beckman Coulter, Inc., 2007) using apertures of different sizes. In Coulter counters, a small aperture is embedded between two fluidic cells and a baseline ionic current is induced by applying an electrical bias across the aperture (Fig. 1.1 (a)). When a non-conducting particle flows through the electrolyte-filled aperture, it displaces a volume of electrolyte equivalent to its own volume, and hence increases the electrical resistance of the aperture temporarily (Bunville, 1984). This resistance modulation will lead to a corresponding decrease of ionic current (Fig. 1.1 (b)) or increase of the electrical voltage drop across the sensing channel, which can be measured and used as an indicator of the presence of the particle. The Coulter principle, or resistive pulse sensing, is also known as the electrical sensing zone method.

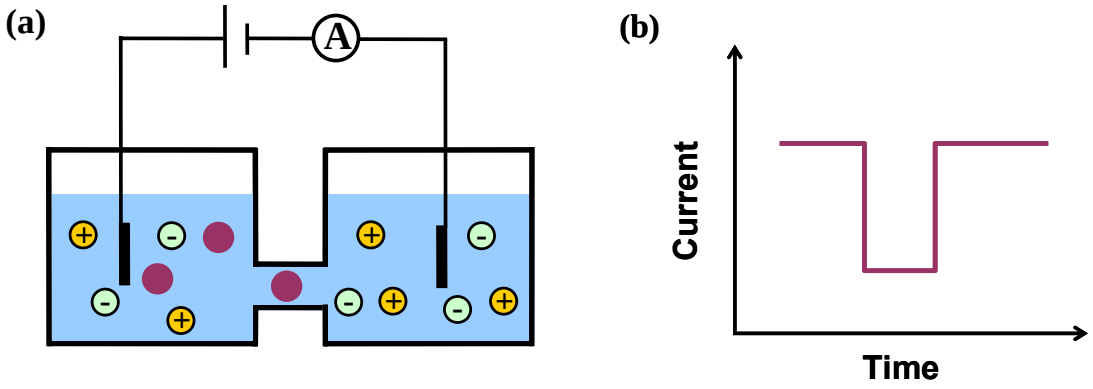

Figure 1.1 Working mechanism of a Coulter counter. (a) Schematic of the basic components of a Coulter counter – an aperture separating two fluid cells and a baseline ionic current through the aperture is induced by applying an electrical bias across the aperture; (b) Schematic of the typical signal of a Coulter counter. The magnitude of the current pulses can be used to determine the size of the analyzed particles; the number of pulses per second represents the particle concentration.

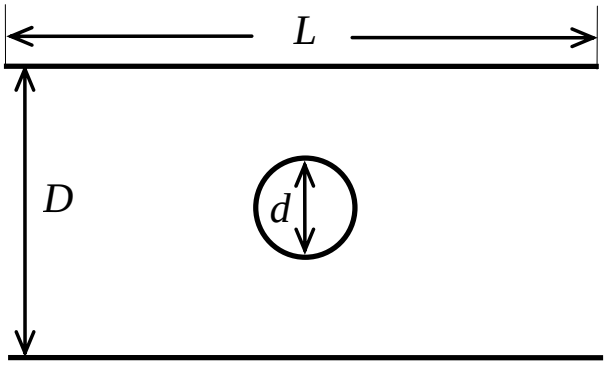

Figure 1.2 Schematic of an electrolyte-filled cylindrical pore of diameter D and length L containing a non-conducting sphere of diameter d.

Maxwell first tackled the problem of the electrical resistivity increase caused by non-conducting spheres infinitely diluted in a solution of resistivity ρ and obtained an expression for the effective resistivity ρ_{eff} as (DeBlois & Bean, 1970)

$$\rho_{eff} = \rho(1 + 3f/2 + \cdots), \tag{1.1}$$

where f is the fraction of the volume occupied by the spheres in the suspension. Considering a cylindrical pore of diameter D and length L filled with a fluid of resistivity ρ (as shown in Fig. 1.2), the electrical resistance of the pore containing the pure ionic solution can be calculated as

$$R = 4\rho L/\pi D^2, \tag{1.2}$$

in the limit $L >> D$. When a non-conducting sphere is inserted in the pore, the volume fraction is

$$f = 2d^3/3D^2L. \tag{1.3}$$

If the diameter of the sphere is much smaller than the diameter of the pore (thus the pore surface is far from the sphere), the current problem is equivalent to Maxwell's model and the electrical resistance of the pore containing a non-conducting sphere can be obtained as

$$R' = (4\rho L/\pi D^2)(1 + d^3/D^2L + \cdots). \tag{1.4}$$

Thus the increase in the electrical resistance of the sensing pore is given by

$$\Delta R = R' - R = 4\rho d^3/\pi D^4. \tag{1.5}$$

The relative change of the pore resistance is therefore

$$\Delta R/R = d^3/D^2 L\,. \tag{1.6}$$

In resistive pulse sensing, the ionic current through the sensing aperture is normally monitored to detect the translocation of the particles. If there is no particle inside the pore, the baseline ionic current I can be calculated by

$$I = \frac{V}{R}\,. \tag{1.7}$$

Here V is the applied voltage across the aperture. When a particle is passing through the aperture, the ionic current will decrease, which can be calculated as

$$I^* = \frac{V}{R+\Delta R} = I\left(1+\frac{\Delta R}{R}\right)^{-1}\,. \tag{1.8}$$

If $\Delta R/R << 1$, the ionic current modulation can be approximated by

$$\frac{\Delta I}{I} \approx \frac{\Delta R}{R}\,. \tag{1.9}$$

According to the above equation, the ionic current modulation is approximately the same as the pore/aperture resistance modulation. Therefore, successful resistive pulse sensing requires the size of the analyzed particles be comparable to the size of the sensing aperture. The conventional Coulter counter consists of an aperture typically tens of microns in diameter and Coulter (1956) first demonstrated the counting of micron-sized red blood cells with this kind of device at a high throughput of ~ 6000 particles/s. Later, the capability of resistive pulse sensing technique was extended to count and size bacterial cells with a size of microns or sub-micron by using a smaller glass pore of 10 μm in diameter and 50 μm in length (Kubitschek, 1958). Since then, a major trend in the field of the Coulter counting is to invent new fabrication methods to make smaller

apertures for detection of smaller particles. Counting rate/throughput is the other important parameter for assessing the performance of the Coulter counter and has also gained some researchers' attention.

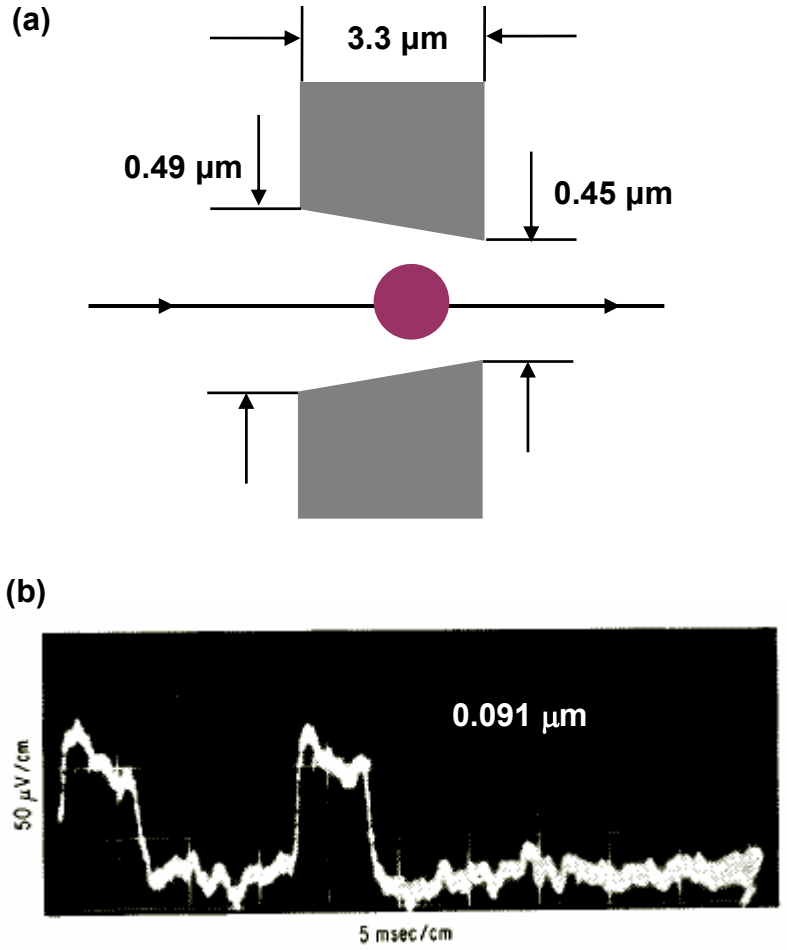

Figure 1.3 (a) Schematic of a tapered submicron-sized pore used by DeBlois and Bean (1970) as the sensing aperture. (b) Voltage modulation recorded for two polystyrene spheres with a diameter of about 91 nm passing through the same pore. (DeBloise & Bean, 1970)

Counting of particles much smaller than 1 µm was first achieved by DeBlois and

Bean in 1970 with a device containing a submicron-sized pore in a membrane. The pores were prepared through a two-step process: first, a polycarbonate plastic sheet was irradiated by a high energy nuclear particle source; then the damage tracks left on the sheet by the particles were etched through with a chemical solution to obtain a single pore of submicron-size. It was shown that a minimum volume ratio of ~ 0.06% can be detected by measuring the voltage modulation across a tapered pore with end diameters of 490 nm and 450 nm as polystyrene beads of 91 nm in diameter flowed through the pore (Fig. 1.3). DeBlois and Bean (1970) also developed a theory to predict the upper limit for the change in the electrical resistance when a particle flowed through the sensing channel. Later, DeBlois and Wesley (1977) showed that the resistive pulse sensing technique could be used to determine the size and concentration of viruses by comparing the voltage modulation observed when viruses flowed through a submicron-sized sensing pore with the voltage modulation measured when standard 109 nm-diameter latex spheres flowed through the same pore. Thus, they were able to determine the sizes of several different types of viruses ranging from 110 nm to 140 nm.

As the optimization of the Coulter counter device further continued, Sikdar and Webster (1980) showed that they were able to count particles at a high rate and measure the mean and variation of particle size distribution accurately. Berge and co-workers (1989) developed a technique that enabled them to reverse the flow of particles through the sensing channel of the Coulter counter by reversing the pressure drop across the sensing channel. This allowed them to study the dissolution of air bubbles and radial

migration of particles as a function of time.

A salient trend of the Coulter counter development since the 1990s is to develop disposable 'Microchip Coulter counter.' Larsen and colleagues (1997) were the first to report the design and fabrication of microchip Coulter counters fabricated on a silicon substrate by using standard microfabrication techniques. Hydrodynamic focusing technique was implemented in their devices for the purpose of focusing the sample fluid and improving the sensitivity. Koch and co-workers (1999) later reported a similar micromachined Coulter counter, also built on the silicon substrate but without the hydrodynamics focusing system. However, both of them did not report detailed experimental characterization of their devices. Saleh and Sohn (2001) fabricated a microchip Coulter counter on a quartz substrate, which enabled them to sense individual nanoscale colloids down to a minimum diameter of 87 nm in a sensing channel that was 8.3 μm long with a cross-sectional area of 0.16 μm^2. Later, they developed a PDMS-based device with a sensing channel of 200 nm in diameter and 3 μm long and showed that they were able to detect DNA translocation through this channel (Saleh & Sohn, 2003). Carbonaro and Sohn (2005) fabricated a PDMS-based device with multiple sensing channels and used the device to detect the size change of 490 nm-diameter latex colloids upon antigen-antibody binding on the antibody-coated colloid surface. In this way, they could simultaneously detect two kinds of human antigens on a single chip. Zhang and co-workers (2005) developed a microchannel-based Coulter counter with 100-200 μm-diameter microchannels to detect pollen particles of 17-25 μm

in diameter. Both current enhancement and current blockage were observed for Secale Cerale grass pollen particles in their experiments and they explained this phenomenon by taking account of the particle size and surface charges. Jagtiani and colleagues (2006) designed and fabricated a multi-aperture microfluidic Coulter counter and improved the counting efficiency substantially as compared to a single-channel Coulter counter. Most recently, Zhe and co-workers (2007) reported another multi-channel microfluidic Coulter counter and the crosstalk between different microchannels was circumvented in their new design by placing the electrodes in the center of the microchannel. Rodriguez-Trujillo and co-workers (2006) fabricated a PDMS-based microfluidic Coulter counter with hydrodynamic focusing implemented in their device.

Another trend in the development of Coulter counters since the 1990s is using nanoscale pores as the sensing aperture to detect single macromolecules or nanoparticles, i.e. the so-called 'Molecular Coulter counter' (Bezrukov, 2000). The naturally occurring ion channels are first combined with the resistive pulse sensing technique to explore the possibility of sensing particles in the nanometer scale and DNA molecules. Bezrukov et al. (1994) demonstrated the counting of polymer molecules as they passed through a single alamethicin pore of ~5 nm in length and ~2 nm in diameter. Kasianowicz and co-workers (1996) detected individual strands of DNA and RNA with α-hemolysin, a transmembrane protein nanopore. As shown in Fig. 1.4, the α-hemolysin nanopore was embedded in a lipid bilayer membrane separating two fluid cells and a baseline ionic current was induced by applying an electrical bias across the nanopore. When single

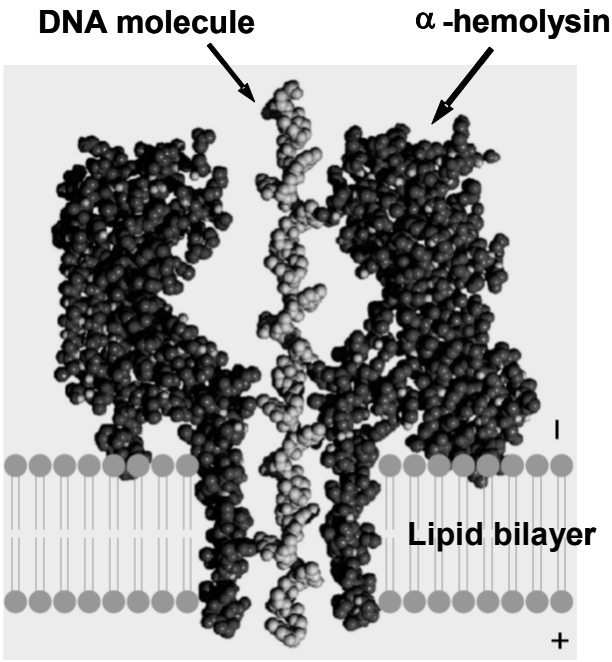

Figure 1.4 A DNA molecule flowing through an α-hemolysin nanopore inserted in a lipid bilayer (Deamer & Akeson, 2000)

stranded DNA molecules were translocated through the nanopore, the baseline ionic current was partially blocked, making an extremely sensitive single molecule detector. These promising results sparked many studies of DNA translocation and dynamics in biological nanopores (Bezrukov, 2000; Bayley & Martin, 2000; Deamer & Akeson, 2000; Bayley & Cremer, 2001; Meller & Branton, 2002; Peterman et al., 2002; Meller, 2003; Nakane et al., 2003). However, the sensors based on biological nanopores are not very robust (the supporting biological membranes tend to rupture in a few hours), and hence are precluded from applications in practical sensing devices. In addition, the dimension of the protein nanopores is not tunable, which also limits their usage. Therefore, robust,

size-tunable, inorganic nanopores are highly desired to overcome the above-mentioned limitations.

In the past decade, various solid-state nanopores/nanotubes have been fabricated and used for single molecule/nanoparticle sensing (Goldberger et al., 2006; Rhee & Burns, 2007), which are reviewed as follows. Kobayashi and Martin (1997) fabricated gold nanotubules with diameters less than 2 nm and used them to measure the concentration of divalent cations, $Ru(bpy)_3^{2+}$ and methylviologen (MV^{2+}). Sun and Crooks (2000) used a multi-wall carbon nanotube-based device to sense 60-100 nm-diameter polystyrene particles as they flowed through a 150 nm-diameter carbon nanotube. This method was then improved by members of the same group to determine sizes and surface charges of polystyrene particles simultaneously (Ito et al., 2003; Ito et al., 2004). Li and co-workers (2001; 2003) were the first to fabricate solid-state nanopores using ion and electron beam technologies and to use the fabricated pores to study DNA translocation and dynamics. Similar devices based on artificially fabricated solid-state nanopores in various silicon-based materials like silicon nitride and silicon oxide were then developed by the same group (Fologea et al., 2005) and also other groups to detect DNA translocation (Chen et al., 2004; Chang et al., 2004; Heng et al., 2004; Storm et al., 2005; Smeets, et al., 2006). Chen and co-workers (2004) fabricated silicon nitride nanopores of ~ 15 nm in diameter and showed that coating the nanopore surface with alumina helped to suppress the electrical noise and enabled them to measure a larger number of DNA translocation events per nanopore. Chang and colleagues (2004) studied DNA

translocation through silicon dioxide nanopores of 50-60 nm long, 4-5 nm in diameter and demonstrated that the ionic current in the nanopore could increase due to the mobile counter ions attracted by the DNA itself. Heng and colleagues (2004) made silicon nitride nanopores with a diameter around 1 nm and reported that they were able to distinguish single-stranded DNA from double-stranded DNA and resolve the length of the molecule based on the ionic current modulations measured. Storm and co-workers (2005) studied the translocation of double-stranded DNA fragments of different lengths through a 10 nm silicon dioxide pore, and found a power-law scaling of the translocation time with the DNA length. Fologea and colleagues (2005) reported that they were able to slow down DNA translocation by a factor of ten through 4-8 nm-diameter silicon nitride nanopores by controlling the electrolyte temperature, salt concentration, viscosity, and the bias voltage across the nanopore. In addition to the short, small nanopores, long silicon dioxide nanotubes (~20 μm in length) with a much larger inner diameter of 40-60 nm were also shown to be able to sense the translocation of DNA molecules (Fan et al., 2005). With this nanotube-based device, Fan and co-workers (2005) found that the ionic current could either decrease or increase as DNA molecules were translocated through the nanotube, depending on the concentration of the electrolyte used. Later, the same phenomena were also observed in a device based on a 10 nm-diameter silicon dioxide nanopore (Smeets et al., 2006).

Despite all the great success in the fabrication of nanoscale features leading to a dramatic reduction in the volume of the sensing channel, the lowest detectable volume

ratio using the resistive pulse sensing technique, has been 0.06% (DeBlois & Bean, 1970), which is approximately the same as the amplitude of the ionic current modulation. Indeed, a survey of all the single molecule detection based on the ionic current modulation shows that the relative modulation is higher than 0.06%, indicating that the detected volume ratio is larger than 0.06%. This detection limit requires the fabrication of very small fluidic channels, which may be difficult if the analyzed molecules are very small. In addition, the spectrum of the sensor, i.e., the range of particle sizes that is detectable with a specific device, is limited. Different from the aforementioned Coulter counters, we have developed a new sensing scheme to detect the translocation of particles through a fluidic channel, which integrates the fluidic circuit with a MOSFET and monitors the MOSFET drain current to sense the resistance modulation of the sensing channel. We demonstrate that amplification can be achieved from both the fluidic circuit and the MOSFET, and a minimum volume ratio of 0.006%, 10 times smaller than the lowest volume ratio reported in the literature, can be achieved.

Molecular Dynamics Simulations in Nanofluidics

With the emergence of numerous nanofluidic devices, fundamental studies of nanofluidics have attracted significant attention because the success of nanofluidic devices depends on a thorough understanding of the fluidic, ionic and molecular behavior in highly confined nanochannels. For example, as mentioned above, in the experiments of detecting DNA molecules with nanofluidic sensors based on the resistive pulse sensing

technique, both ionic current enhancement and blockade events were observed depending on the concentration of the electrolyte used. The ionic current blockade is expected from the Coulter principle. The ionic current enhancement at low electrolytic concentration is normally attributed to the channel conductance increase because of the additional mobile counter ions adsorbed on the DNA molecules to shield the charges of its backbone. However, the crossover from current enhancement to current blockade occurred at different electrolytic concentrations in different experiments (~ 0.79 M in Fan et al., 2005; 0.4 M in Smeets et al., 2006), indicating that the complex charge interactions inside the nanopore/nanochannel may not be fully reflected with the simple models presented in the literature. Moreover, current blockade instead of current enhancement occurred in Saleh and Sohn's work (2003) even though the concentration of the buffer used (0.1 M) is lower than the crossover concentrations given above. In addition, it has been experimentally shown that the ion conductance in nanochannels could be very different from the prediction based on the bulk ion concentration and can be tuned with a gate voltage (Stein et al., 2004; Karnik et al., 2005), which is due to the comparable size of the nanochannel and the Debye screening length. Therefore, understanding the ion concentration and distribution inside a nanochannel corresponding to a bulk electrolyte of certain given concentration is critical to the design and application of nanofluidic devices.

When an electrolyte is in contact with a solid surface, a layer of fixed surface charges and a layer of mobile counter-ions will form an electric double layer structure. In nanochannels, the double layer thickness could be comparable to the size of the

nanochannel, and hence double layers from different channel walls could overlap, which may lead to very different fluidic properties compared to those of the bulk fluid. With DNA or protein molecules present in the nanochannel, the system becomes even more complex since they will attract counter-ions to shield charges on their backbones and alter the ion distribution in the nanochannel.

The ion concentration and distribution in nanochannels depend on the surface chemistry and the structure of the electric double layers. In nanochannels, the electric double layers may overlap, and the classical Poisson-Boltzmann equation may not be applicable since the Boltzmann equation can not be used to describe the ion distribution in the channel. However, an accurate and well-accepted model has not been developed yet. In the past decade, molecular dynamics simulation method has developed to be a powerful tool to study the ion distribution in electric double layers, electroosmotic flow, and macromolecule translocation through nanochannels. Quite a few MD simulations (Mattke & Kecke, 1998; Spohr, 1999; Spohr, 2002; Freund, 2002; Spohr, 2003; Qiao & Aluru, 2003; Zhu et al., 2005; Qiao & Aluru, 2004; Qiao & Aluru, 2005) have been performed to study the ion and potential distributions in the nanochannel with separated or overlapped electric double layers for different ion concentrations and different surface charge densities. Spohr (1999; 2002; 2003) modeled a single electric double layer formed with 2.2 mol/kg aqueous NaCl and CsF solutions near a metallic electrode that is either uncharged, positively or negatively charged with a surface charge density of 9.9 $\mu C/cm^2$. Even though the total simulation system is relatively small (400 water

molecules and a total of 32 ions), the obtained water and ion profiles in the electric double layer fit the expectation based on the classical theory. In the simulation, Spohr first assigned the numbers of mobile cations and anions and then calculated surface charges as the number difference between these two kinds of ions. The solution concentration used (2.2 mol/kg) was based on the neutral solution when there was no surface charge and it was assumed to be the same even when the numbers of cations and anions are changed to be unequal to each other. Mattke and Kecke (1998) modeled the ion and potential distribution for single, overlapped, and sheared electric double layers formed in-between two aluminosilicate kaolinite surfaces with electrolytes of different concentrations. It was shown that the overlap of electric double layers could lead to significant change of the ion and potential distribution. In their simulation, the local anion concentration was taken as the electrolyte concentration. Freund (2002) modeled the electroosmotic flow of a 0.01 M Cl^- solution and found that the viscosity near the wall could be six times higher than the bulk viscosity. Only Cl^- ions were considered in the simulation without any justification even though the Debye length was only 3.04 nm, less than half of the channel width (6.5 nm) of the simulation domain. Zhu et al. (2005) studied the electroosmotic flow of a simplified electrolyte model (non-polar solvent) in nanochannels and found that the continuum theory had to be corrected to agree with the molecular dynamics simulation results. The cation and anion numbers in the simulation were 31 and 12, respectively, but no discussion as to why these numbers were selected was presented. Qiao and Aluru (2003; 2005) further examined the ion distribution in the

nanochannel with different surface charge densities and found that the near-wall ion distribution could be significantly different from the prediction of the classical theory. More interestingly, in another simulation performed by Qiao and Aluru (2004), it was found that under high surface charge density, the charge distribution in nanochannels could show an inversion, i.e., a higher co-ion concentration than the counter-ion concentration, in the region of 0.53 nm away from the channel wall, which is totally contradictory to the classical theory. In these simulations, either only counter-ions (Qiao & Aluru, 2003) were considered or the concentration of co-ions was assumed to be the electrolyte concentration and the number of counter-ions is the sum of co-ions and the surface charges (Qiao & Aluru, 2004; Qiao & Aluru, 2005).

Although significant progress has been made on molecular dynamics studies of phenomena in nanochannels, one important and fundamental issue remains unsolved, i.e. the assignment of the number of counter-ions and co-ions in the simulation domain seems arbitrary. So far, attention has been paid to meet the requirement of overall charge neutrality among surface charges and mobile ions in the electrolyte. However, since both counter-ions and co-ions may exist in the electrolyte, and neither the concentration of the counter-ions nor that of the co-ions is the same as the bulk concentration, the number of counter-ions and co-ions cannot be derived solely from the requirement of charge neutrality. In the literature, it is common that the concentration of the co-ions is taken as the bulk value, whereas the number of the counter-ions is determined by balancing the sum of surface charges and co-ions, which might not be accurate. For the

cases of high electrolyte concentrations, which have small Debye lengths, only considering counter-ions in the simulation domain does not correspond to any real situation. For the development of nanofluidic devices, it is important to model more accurately the cation and anion concentrations inside nanochannels corresponding to a certain bulk concentration to elucidate experimental phenomena such as different current modulations under different electrolyte concentrations for the experiments of DNA detection (Chang et al., 2004; Fan et al., 2005; Smeets et al.). In this dissertation, this fundamental problem is investigated by extending the MD simulation domain to include two bulk regions sandwiching the nanochannel region of interest. Using this approach, when the system reaches equilibrium, the concentration of the electrolyte in the bulk region and the number of both counter-ions and co-ions in the nanochannel region emerge naturally.

In addition to the ion distribution in nanochannels, the structure of water molecules at the solid and liquid interface has also attracted significant research interest (Verdaguer et al., 2006; Cheng et al., 2001). It is well-known that the water near solid interfaces is significantly more aligned than the bulk liquid (Verdaguer et al., 2006). For example, water density oscillations adjacent to a solid wall have been well reported in the literature (Mattke & Kecke, 1998; Spohr, 1999; Spohr, 2002; Freund, 2002; Spohr, 2003; Qiao & Aluru, 2003; Zhu et al., 2005; Qiao & Aluru, 2004; Qiao & Aluru, 2005), which is normally attributed to the non-electrostatic interactions between solid atoms and water molecules and exists no matter if the surface is charged or not. It is believed that the

structure of water molecules within a few nanometers of a solid surface determines the wetting properties, i.e. hydrophobicity or hydrophilicity, and other solid-liquid interfacial properties such as solute adsorption, dielectric properties, and so on (Cheng et al., 2001). The layering of water molecules in the near wall region may also affect the thermal transport through a solid-liquid interface due to the fact that the thermal conductivity of a material with highly order crystal structures is typically much higher than the amorphous material. In this dissertation, we also performed extensive molecular dynamics simulations to study the effects of surface charge densities and solid surface structures on the ion and water distribution profiles near charged (100) and (111) silicon surfaces.

Organization of the Dissertation

This dissertation will present both the experimental work on development of ultra-sensitive fluidic sensors and molecular dynamics studies of ion and water distribution in nanochannels. The organization of the dissertation is as follows. Chapter I reviews previous work in the development of resistive pulse sensing technique and Molecular Dynamics simulations in the field of nanofluidics, and discusses the motivation of the current research. Chapter II presents a new sensing scheme and describes the design, fabrication, and detailed characterization of a MOSFET-based microfluidic resistive pulse sensor. This sensing scheme is also implemented at nanometer scale for detecting nanoparticles and all related work is presented in Chapter III. Chapter IV describes the molecular dynamics simulation method and the simulation

results of ion and water distribution in nanochannels. Finally, Chapter V summarizes the conclusions that have been drawn from the work in this dissertation.

CHAPTER II

MOSFET-BASED MICROFLUIDIC RESISTIVE PULSE SENSORS

This chapter describes a new mechanism based on resistive pulse sensing to detect particles flowing through the sensing channel. Different from traditional resistive pulse sensors, the new sensing scheme integrates the fluidic circuit with a MOSFET and monitors the modulation of the MOSFET drain current to detect the translocation of particles. Theoretical analysis shows that compared to the ionic current modulation, the percentage modulation of the MOSFET drain current can be amplified by both the fluidic circuit and the MOSFET, and hence the sensitivity of the device can be improved substantially. This sensing scheme was first implemented at the microscale level with a polydimethylsiloxane(PDMS)-based microfluidic chip. The performance and capability of this MOSFET-based microfluidic sensor were extensively tested with various micron-sized particles including polystyrene beads, glass beads, and white blood cells.

The New Sensing Scheme

The new sensing scheme is based on a three-terminal fluidic device as shown in Fig. 2.1, instead of the common two-terminal layout of resistive pulse sensors. The horizontal fluidic circuit is composed of two large microchannels sandwiching a small

sensing channel. The sensing channel could be microscale or nanoscale depending on the size of the particles to be analyzed. The vertical microchannel is connected with the gate of a MOSFET to detect the change of electrical potential at the end of the sensing channel, which reflects the resistance modulation of the sensing channel upon the translocation of particles. An ionic current is induced by applying an electrical bias ($V_+ - V_-$) across the horizontal channels and particles can be driven through the sensing channel by either electroosmotic flow or electrophoretic migration. The fluidic and MOSFET circuits are commonly grounded.

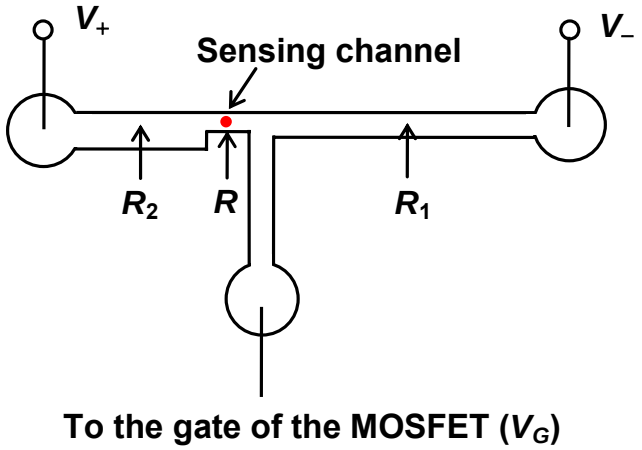

Figure 2.1 Schematic of the fluidic device (not to scale). The resistances of three horizontal channels are denoted by R_2, R, and R_1, respectively.

When a particle travels through the sensing channel, the conductance of the channel decreases because of the excluded volume of the electrolyte. The reduced channel conductance will then lead to a drop of the ionic current through the circuit and the

electrical potential at the downstream end of the sensing channel will also decrease. Instead of directly sensing the ionic current modulation as in traditional resistive pulse sensors, the above potential modulation is monitored with a MOSFET to detect particles. The next section demonstrates theoretically that amplification can be achieved through both the fluidic circuit and the MOSFET.

Theoretical Analysis of the Amplification Effects

If the particles are in a diluted suspension, their effects on the electrical resistances of the large fluidic channels are negligible. Denoting the resistances of the three horizontal channels as R_2, R, and R_1, as labeled in Fig. 2.1, and the increase in the resistance of the sensing channel as ΔR, the ionic current without (I) and with (I^*) a particle in the sensing channel can be written as

$$I = \frac{V_+ - V_-}{R_2 + R + R_1}, \text{ and } I^* = \frac{V_+ - V_-}{R_2 + R + \Delta R + R_1}, \tag{2.1}$$

respectively. The gate potentials of the MOSFET are then

$$V_G = V_- + IR_1 \text{ and } V_G^* = V_- + I^* R_1. \tag{2.2}$$

Assuming the change of the gate potential

$$\Delta V_G = V_G - V_G^*, \tag{2.3}$$

Then the modulation of the gate potential can be derived as

$$\frac{\Delta V_G}{V_G} = \frac{\Delta I R_1}{V_G} = \frac{IR_1}{V_G} \cdot \frac{\Delta I}{I} = \frac{IR_1}{V_G} \cdot \frac{\Delta R}{R_t} = (\frac{IR_1}{V_G} \cdot \frac{R}{R_t}) \cdot \frac{\Delta R}{R}, \tag{2.4}$$

where $\Delta I = I - I^*$ and $R_t = R_2 + R + \Delta R + R_1$. The modulation of the sensing channel resistance, $\Delta R / R$, is approximately equal to the volume ratio of the particle to the sensing channel, when the particle diameter is small compared to the channel size. Equation (2.4) indicates that the modulation of the gate potential can be amplified by a factor of $IR_1 / V_G \cdot R / R_t$ compared to the modulation of the channel resistance. The modulation of the gate potential can then be detected by measuring the MOSFET drain current, which depends on the gate potential and has different function forms when the MOSFET is working in different regimes.

A. Saturation Regime

If the gate potential, V_G, is larger than the threshold voltage of the MOSFET, V_T, and the drain-source bias, V_{DS}, satisfies $V_{DS} > V_G - V_T$, the MOSFET works in the saturation regime. The drain current of the MOSFET, I_D, can be written as (Casey, 1999; Sze, 1981)

$$I_D = k_{Sat} (V_G - V_T)^2 , \tag{2.5}$$

where k_{Sat} is a constant. For a small modulation, ΔV_G, the drain current modulation can be derived by differentiating Eq. (2.5) as

$$\frac{\Delta I_D}{I_D} = \frac{2V_G}{V_G - V_T} \cdot \frac{\Delta V_G}{V_G} . \tag{2.6}$$

As can be seen from Eqs. (2.4) and (2.6), the modulation of the MOSFET drain current can be amplified by two factors $A_1 = IR_1 / V_G \cdot R / R_t$, and $A_2 = 2V_G / (V_G - V_T)$, which are

the amplification factors from the fluidic circuit and the MOSFET, respectively. For the MOSFET, a large amplification factor can be achieved if $V_G - V_T << V_G$, so the gate potential selected should be only slightly higher than the threshold voltage. A factor A_1 larger than 1 can be achieved by carefully designing the microfluidic device and the details will be discussed in next section.

B. Sub-Threshold Regime

The amplification from the MOSFET can be even larger if it is biased in the sub-threshold regime ($V_G < V_T$), for which the drain current changes exponentially with the gate potential as (Sze, 1981)

$$I_D = k_{sub}(1-\exp(-\frac{qV_{DS}}{kT}))\exp(\frac{q\psi_S}{kT})(\frac{q\psi_S}{kT})^{1/2}, \tag{2.7}$$

where k_{sub} is a constant and q, k and T are the elementary electric charge, the Boltzmann's constant and temperature, respectively. ψ_S is the surface potential of the MOSFET electronic channel and is given by

$$\psi_S = V_G - V_{FB} - \frac{a^2 kT}{2q}\left\{[1+\frac{4}{a^2}(\frac{qV_G}{kT}-\frac{qV_{FB}}{kT}-1)]^{1/2}-1\right\}, \tag{2.8}$$

where $a = 2(\varepsilon_s/\varepsilon_{ox})(d_{ox}/L_D)$. ε_s and ε_{ox} are the permittivity of the semiconductor and that of the oxide, respectively. d_{ox} is the thickness of the MOSFET gate oxide, L_D is the extrinsic Debye length, and V_{FB} is the flat-band voltage.

Based on Eqs. (2.4), (2.7), and (2.8), we can derive the theoretical drain current

modulation for the MOSFET working in the sub-threshold regime as

$$\frac{\Delta I_D}{I_D} = \left(\frac{qV_G}{kT} - \frac{V_G}{2\psi_S}\right)\left(\frac{d\psi_S}{dV_G}\right)\left(\frac{IR_1}{V_G}\right)\left(\frac{R}{R_t}\right)\frac{\Delta R}{R}. \tag{2.9}$$

This equation is cumbersome to use as we do not have the necessary information such as the dopant concentration, oxide thickness and flat-band voltage to evaluate the variables a and V_{FB}, and hence ψ_S.

In ideal situations, i.e., if we assume there is no fixed oxide charge, interface traps or difference in work function between the semiconductor and the gate metal, and if the diffusion current can be neglected, then ψ_S is approximately equal to V_G. Eq. (2.9) can then be simplified as

$$\frac{\Delta I_D}{I_D} \approx \left(\frac{qV_G}{kT} - \frac{1}{2}\right)\left(\frac{IR_1}{V_G}\right)\left(\frac{R}{R_t}\right)\frac{\Delta R}{R}. \tag{2.10}$$

Therefore, the amplification factor from the MOSFET in the sub-threshold regime can be written as $A_3 = qV_G/kT - 1/2$. The typical value of q/kT is around 40 at room temperature and for a threshold voltage of 2.1 V, a MOSFET amplification factor of around 80 can be achieved.

Design and Fabrication of the Microfluidic Device

The schematic of the microfluidic device is shown in Fig. 2.1. According to the theoretical analysis in the above section, the amplification factor from the fluidic circuit can be defined as

$$A_1 = \frac{IR_1}{V_G} \cdot \frac{R}{R_t} = \frac{IR}{V_G} \cdot \frac{R_1}{R_2 + R + \Delta R + R_1}. \quad (2.11)$$

Once the dimension of the sensing channel and the electrolyte are selected, its resistance R can be treated as a constant. The ionic current I and the gate potential V_G can be tuned by adjusting the applied electrical bias (V_+ and V_-). As seen from Eq. (2.11), the resistances of two large microchannels (R_1 and R_2) can be designed carefully to maximize the amplification effect from the fluidic device. The ideal device has to satisfy the following conditions: $R_2 = 0$ and $R_1 >> R$, which is not very practical because of the requirement of actual channel layout. To achieve a large total amplification factor, we designed the fluidic circuit as $R_1 = 10R$ and $R_t = 12R$. As long as the voltage drop across the sensing channel, IR, is larger than $1.2V_G$, A_1 is larger than 1.

In our microfluidic sensor, the sensing channel (denoted by its resistance R) is 150 μm long and 16 μm wide, while the left microchannel (denoted by its resistance R_2) is 7.5 mm long and 800 μm wide and the right microchannel (denoted by its resistance R_1) is 15 mm long and 160 μm wide. The dimension of the vertical microchannel connecting the downstream end of the sensing channel to the gate of the MOSFET is not critical and is designed here as 6 mm in length and 300 μm in width. All the channels are 30 μm deep.

The microfluidic device was fabricated by bonding a PDMS slab with microchannels on it to a glass substrate. PDMS microchannels were made through a

molding process. First, a negative SU8 (MicroChem Corp, Newton, MA) master of microchannels and reservoirs was formed on the glass substrate by following the standard soft lithorgraphy techniques (Duffy et al., 1998). Then the PDMS prepolymer and the curing agent (Sylgard 184, Dow Corning Inc, MI) were mixed at a ratio of 10:1 and poured over the SU-8 master. The prepolymer mixture was degassed for 2 hours at 0.001 torr and baked in an oven at 80°C for at least 3 hours. The solidified PDMS slab was then peeled off from the glass substrate and three reservoirs with a diameter of 3 mm were punched through the PDMS to facilitate fluid injection and removal. Finally, the PDMS slab and a clean glass slide were treated with oxygen plasma for about 30 second, and brought into contact quickly to form a sealed microfluidic device.

MOSFET Calibration

The performance of the purchased commercially available MOSFET (2N7000 N-Channel FET, Fairchild Semiconductor Co.) was calibrated separately independent of the fluidic circuit before it was used in the experiments. The basic operating principles of MOSFETs have been studied extensively (Casey, 1999; Sze, 1981), so only the characterized MOSFET performance is presented here. The MOSFET gate voltage was controlled by an accurate voltage source (Keithley 6487). A source-measure unit (Keithley 236) was used to apply a constant drain-source bias, V_{DS}, of either 0.15 V or 0.5 V and to measure the MOSFET drain current.

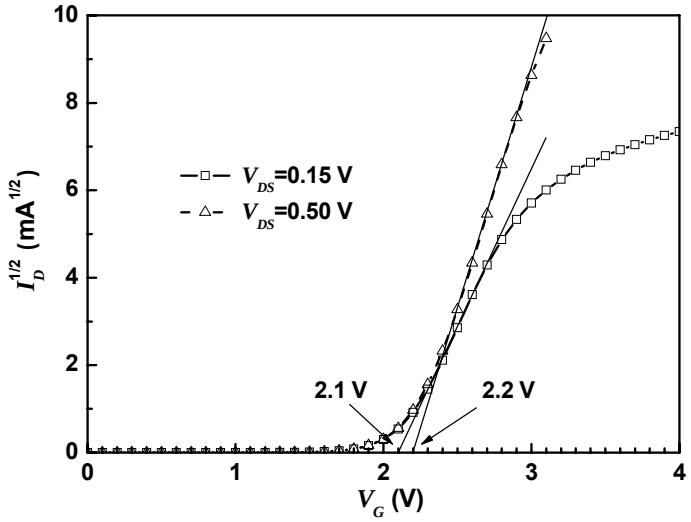

Figure 2.2 $I_D^{1/2}$-V_G curves of the MOSFET for different drain-source biases. The threshold voltage is determined as 2.10 V for V_{DS} =0.15 V and 2.20 V for V_{DS} =0.50 V.

The MOSFET source terminal is commonly grounded with the voltage source and the source-measure unit. Figure 2.2 shows the measured $I_D^{1/2}$-V_G curves for the MOSFET when V_{DS} = 0.15 V and 0.50 V, respectively. The threshold voltage of the MOSFET, V_T, is determined from the x-intercepts of the $I_D^{1/2}$-V_G curves to be ~ 2.10 V when V_{DS} = 0.15 V, and ~ 2.20 V when V_{DS} = 0.50 V. The slight shift of the threshold voltage observed for different drain-source biases can be attributed to the substrate bias effect (Casey, 1999). The typical commercial MOSFET we used has only three terminals for the source, drain and gate electrodes and no terminal to control the substrate bias. Therefore, the substrate is floating and causes the threshold voltage to shift when the drain-source bias is changed. However, this feature does not affect our

measurements as long as we keep the drain-source bias constant in each experiment as the threshold voltage can be determined after V_{DS} is selected.

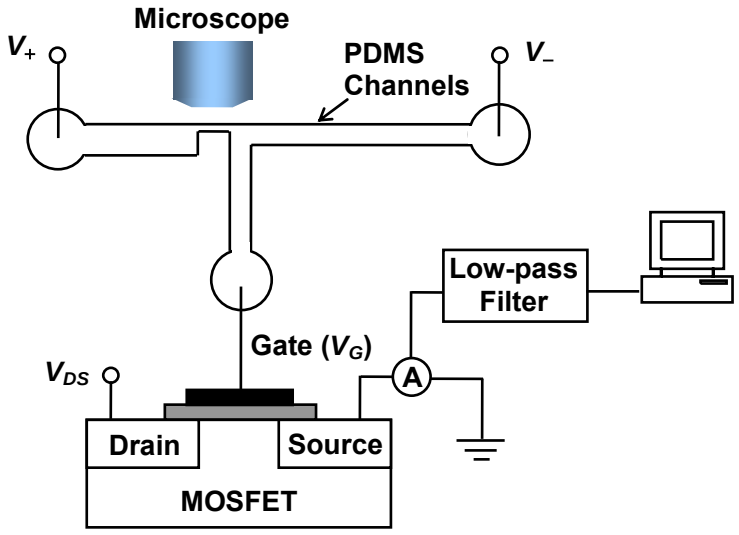

Figure 2.3 Schematic of the experimental set up (not to scale). The fluidic and MOSFET circuits are commonly grounded.

Experimental Details

Figure 2.3 shows the schematic of the experimental set up, which is not to scale. Electroosmotic flow is induced in the horizontal channels by applying an electrical bias ($V_+ - V_-$), which is used as the transport mechanism for particles to pass through the sensing channel. To facilitate the adjustment of the gate potential, thus the working regime of the MOSFET, we apply a positive voltage (V_+) at one end (left side) of the fluidic circuit and a negative voltage (V_-) at the other end (right side). The drain-source

bias (V_{DS}) of the MOSFET is held as a constant for each experiment. Platinum wires were used as the electrodes to connect the fluidic and electronic circuits and the power supplies for V_+, V_-, and V_{DS} were commonly grounded with the current preamplifier. An inverted optical microscope (Nikon Eclipse TE-2000U) was used in the experiments to confirm that the electrical signal was truly associated with the particle translocation.

Three kinds of microparticles were tested in our experiments: polystyrene microbeads of different sizes, 4.8 μm-diameter glass beads, and CD4+ T lymphocyte cells. 7.5 mM sodium borate buffer solution with a PH value of 9.45 was used as the electrolyte to prepare the particle suspension. Before each test, the channels and reservoirs were primed with the buffer solution and then the positive reservoir (denoted by V_+ in Fig. 2.3) was replaced with the particle suspension. When a particle presents in the small sensing channel, the electrical potential distribution in the fluidic circuit will be modified, which will lead to a modulation of the gate potential of the MOSFET, and hence modify the drain current of the MOSFET.

Characterization of the MOSFET-Based Microfluidic Sensor

The detailed characterization of the above MOSFET-based microfluidic sensor is given in this section.

Amplification Effects in Different Working Regimes

As discussed in the section 'Theoretical Analysis of the Amplification Effects', the

amplification factors from the MOSFET are different when it works in different regimes. The characterization results with polystyrene beads of 9.86 μm in diameter are reported here for the MOSFET working in both the saturation regime and sub-threshold regime.

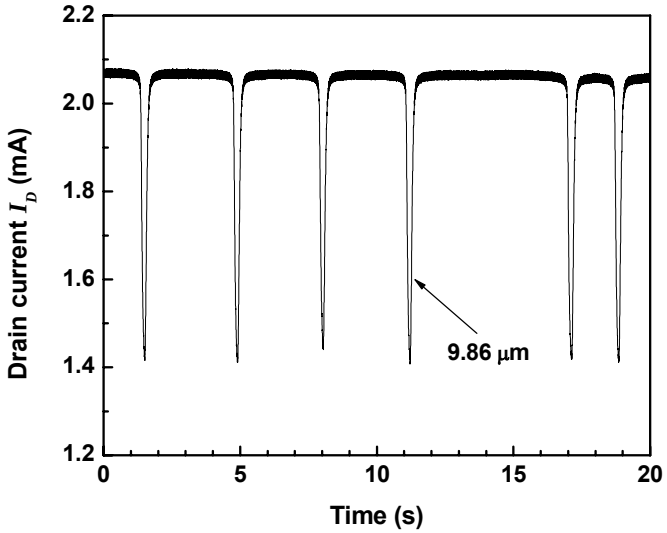

Figure 2.4 Drain current of the MOSFET measured for a particle suspension containing 9.86 μm polystyrene beads. MOSFET is working in the saturation regime.

A. Saturation Regime

Figure 2.4 shows the measured MOSFET drain current when 9.86 μm-diameter polystyrene beads were translocated through the small sensing channel. Each downward peak indicates one particle flowing through the channel, as verified by concurrent optical observation. In this experiment, V_{DS} was set as 0.50 V with $V_{-} = -29\,\mathrm{V}$ and $V_{+} = 11.98\,\mathrm{V}$, respectively. The gate potential of the MOSFET was inferred from the I_D-V_G curve of the MOSFET as ~2.28 V and the MOSFET was

working in the saturation regime. Figure 2.4 shows that a 9.86 μm polystyrene bead leads to a decrease of the MOSFET drain current from 2.07 mA to 1.45 mA, or 30% modulation. The volume ratio of a 9.86 μm polystyrene bead to the sensing channel is about 0.7%, which is approximately the same as the resistance modulation of the sensing channel. Comparing the MOSFET drain current modulation with the resistance modulation of the channel, an amplification of 43 times is achieved.

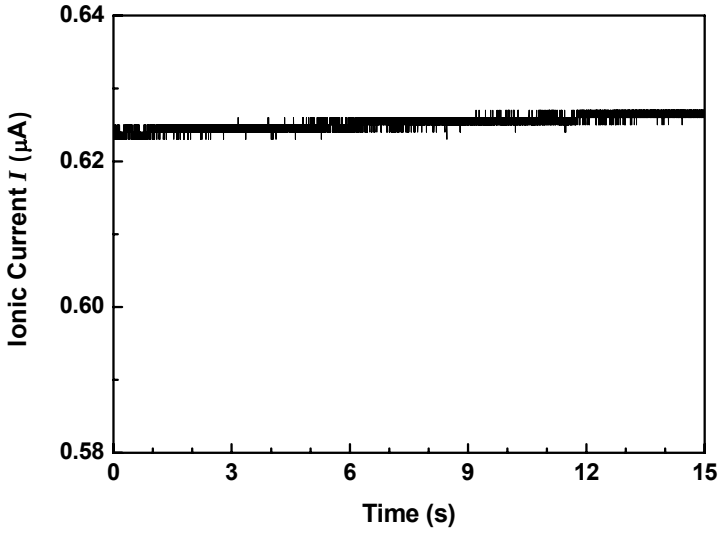

Figure 2.5 Ionic current in the fluidic circuit measured for a particle suspension containing 9.86 μm polystyrene beads.

The resistance modulation will also lead to a corresponding ionic current modulation, which is the widely used sensing mechanism in Coulter-type devices. In order to investigate whether the translocation of 9.86 μm beads can be detected by monitoring the ionic current modulation, we also measured the ionic current though the fluidic circuit, as shown in Fig. 2.5. It can be seen that no discernible downward peaks were observed

when 9.86 μm beads passed through the channel, while the beads translocation was confirmed by the concurrent optical observation. It is worth noting that the noise level of the ionic current is about 0.3% of the baseline ionic current, and the ionic current modulation should be observable since the volume ratio of the 9.86 μm bead to the small sensing channel is about 0.7%, which will lead to an ionic current modulation of 0.7%. However, in our case, because of the two large and long connecting microchannels on each side of the sensing channel, the total resistance of the fluidic circuit is about 12 times that of the sensing channel, so the ionic current modulation is about one-twelfth of the volume ratio, i.e., 1/12×0.7% ~ 0.058%, which is too small to be distinguished from the noise.

B. Sub-threshold Regime

As mentioned in the section 'Theoretical Analysis of the Amplification Effects', even higher amplification factor can be achieved when the MOSFET works in the sub-threshold regime, which is confirmed by the experimental measurement as shown in Fig. 2.6. In this case, V_{DS}, V_{-}, and V_{+} are set as 0.15 V, -29 V, and 11.81 V, respectively. The gate potential of the MOSFET inferred from the I_D-V_G curve is ~ 1.88 V, smaller than the threshold voltage (2.10 V) and thus the MOSFET is working in the sub-threshold regime. The drain current modulation for a 9.86 μm polystyrene bead is ~46%, corresponding to a total amplification factor of 65, higher than that in Fig. 2.4

since the MOSFET is more sensitive in the sub-threshold regime.

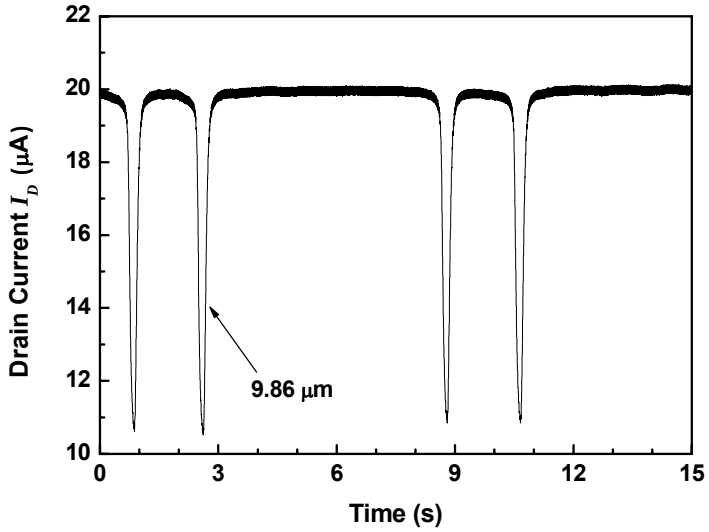

Figure 2.6 Drain current of the MOSFET measured for a suspension containing 9.86 μm polystyrene beads. MOSFET is working in the sub-threshold regime.

Detection of Polystyrene Beads of Different Sizes

To explore the detection limit of our devices, polystyrene beads of different sizes were used for the performance characterization. Figure 2.7 (a) shows the MOSFET drain current recorded for a mixture of 4, 6, and 9.86 μm polystyrene beads. V_- and V_{DS} applied in this experiment are the same as those used for Fig. 2.4, while V_+ is set as 11.92 V. The gate potential is calculated as 2.31 V and the MOSFET is working in the saturation regime. Different-sized beads caused different downward peaks and for the 9.86 μm bead, the drain current modulation is ~28%, which is slightly lower than that in Fig. 2.4 (30%). This lower modulation can be attributed to the higher gate potential (as reflected from the higher baseline drain current of the MOSFET) since the amplification

factor ($A_1 \cdot A_2$) is inversely proportional to $(V_G - V_T)$. The amplification factor in this case is 40. An optical snapshot of the sensing region during the experiment is given in Fig. 2.7 (b), showing the optical image of the polystyrene beads.

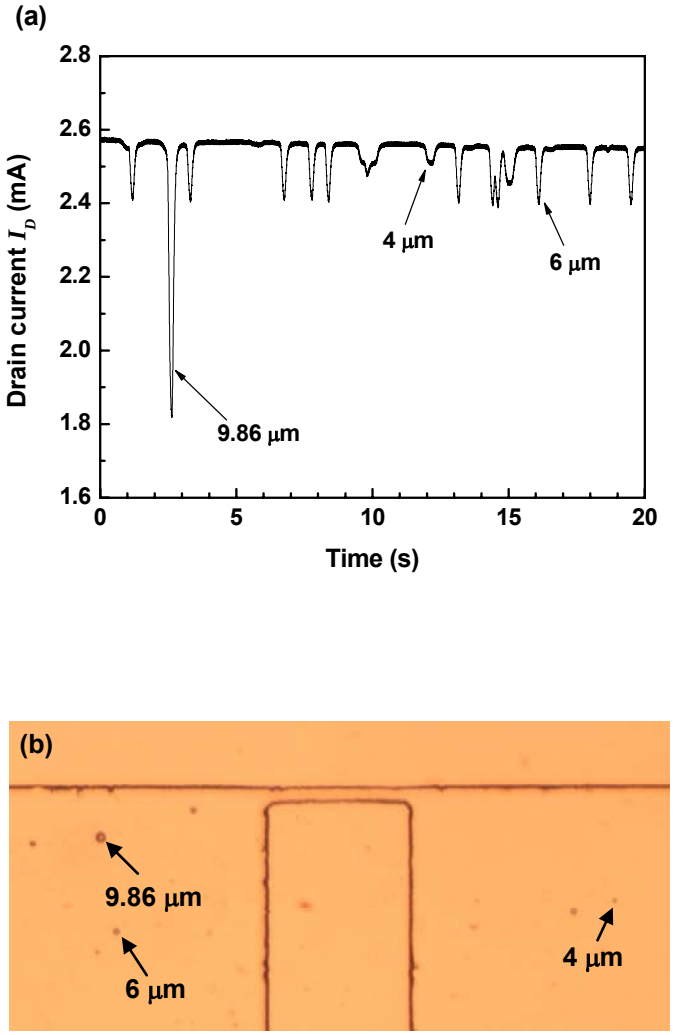

Figure 2.7 (a) Drain current of the MOSFET measured for a mixture of 4 μm, 6 μm, and 9.86 μm polystyrene beads and (b) the photograph of the sensing channel with beads. MOSFET is working in the saturation regime.

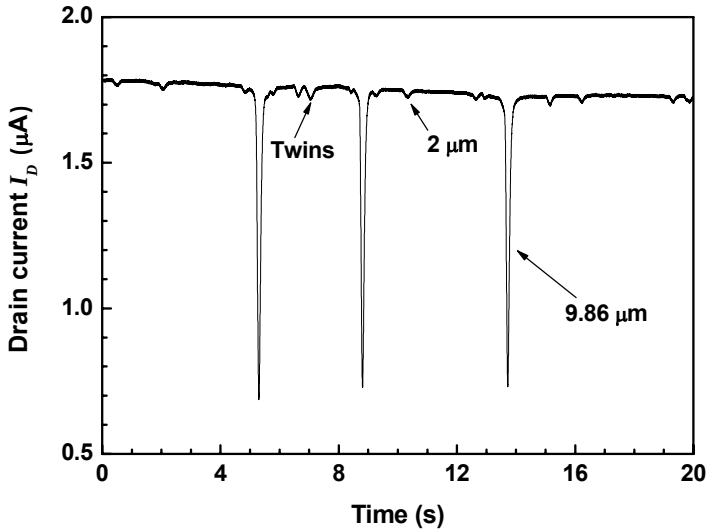

Figure 2.8 Drain current of the MOSFET measured for a mixture of 2 μm and 9.86 μm polystyrene beads. MOSFET is working in the sub-threshold regime.

Figure 2.8 shows the measured MOSFET drain current, I_D, for a mixture of 2 μm and 9.86 μm polystyrene beads when V_{DS} =0.15 V, V_- =-58 V and V_+ =19.56 V, respectively. The gate potential determined from the $I_D - V_G$ curve is 1.70 V, smaller than V_T =2.1 V, and therefore the MOSFET works in the sub-threshold regime. The drain current modulation for a 9.86 μm bead is 56%, corresponding to a total amplification factor of 80, which is much higher than that in Fig. 2.6 (65). The higher amplification factor in this case can be attributed to the higher applied electrical bias across the fluidic circuit, i.e. a higher ionic current. According to Eq. (2.11), the amplification factor from the fluidic circuit, A_1, is larger when the ionic current (I) is higher, resulting in a larger drain current modulation. In this case, we detected 2 μm beads, corresponding to a volume ratio of 0.006%, a much lower limit than that realized from the traditional Coulter-type sensing method (0.06%).

Detection of Particles of Similar Sizes but Different Surface Charges

The ability of the MOSFET-based microfluidic senor to distinguish two similar-sized microbeads with different surface charges was tested with polystyrene beads of a nominal diameter of 4.84 μm and glass beads of a nominal diameter of 4.8 μm. Glass beads are known to have relatively large negative surface charge density (Behrens & Grier, 2001) in aqueous electrolyte solutions and will experience an electrostatic force that opposes the electroosmotic flow of the microbeads (Li, 2004). Therefore, the net speed of the glass beads passing through the small sensing channel will be reduced and the translocation time of the glass beads should be longer than that of the polystyrene beads, which have much lower surface charges. Figure 2.9 shows the MOSFET drain current as a function of time when a mixture of the above-mentioned polystyrene and glass beads is added into the channel. The power supply settings are $V_{-} = -29.10\,\mathrm{V}$, $V_{+} = 11.52\,\mathrm{V}$, and $V_{DS} = 0.15\,\mathrm{V}$. The MOSFET gate potential is ~ 1.84 V so the MOSFET is operating in the sub-threshold regime.

As expected, the magnitude of drain current modulation observed for both types of microbeads are very similar because of their similar sizes. The glass microbeads took a longer time to translocate through the sensing channel compared to the polystyrene microbeads as evidenced by their wider drain current pulses, which is also confirmed by the concurrent optical observation with the optical microscope. In fact, the time taken for the glass microbeads to translocate through the sensing channel was estimated to be ~ 600 ms, in comparison with ~ 400 ms for the polystyrene microbeads. This experiment

demonstrated the ability of the MOSFET-based microfluidic sensor to distinguish particles of similar sizes but different surface charges.

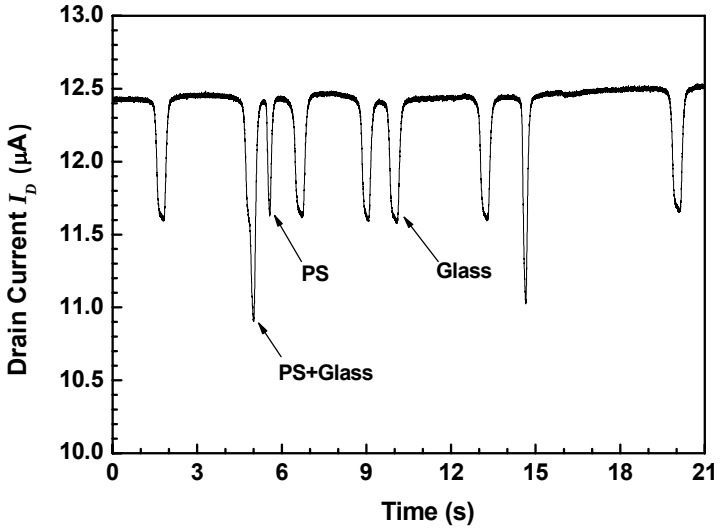

Figure 2.9 MOSFET drain current as a function of time for a mixture of 4.8 μm-diameter glass and 4.84 μm-diameter polystyrene beads with $V_- = -29.10\,\mathrm{V}$, $V_+ = 11.52\,\mathrm{V}$, and $V_{DS} = 0.15\,\mathrm{V}$. The gate potential of the MOSFET is determined to be ~1.84 V so the MOSFET is operating in the sub-threshold regime.

Device Sensitivity as a Function of the Gate Potential

As demonstrated in the sub-section 'Amplification Effects in Different Working Regimes', the MOSFET drain current modulation is a function of the MOSFET gate potential and depends on the MOSFET operating regime, which has been characterized as shown in Fig. 2.10. The characterization was performed with 9.86 μm-diameter polystyrene beads and the setting of the power supplies was $V_{DS} = 0.15\,\mathrm{V}$ and $V_- = -29\,\mathrm{V}$. During the experiment, the gate potential of the MOSFET was varied by

adjusting V_+. It can be clearly seen from Fig. 2.10 that the drain current modulation (%) varies continuously as the gate voltage changes and the amplification effect is more significant when the MOSFET works in the sub-threshold regime. In the sub-threshold regime, the drain current modulation only changes marginally with the MOSFET gate potential, while in the regime above the threshold voltage, the drain current modulation decreases as the MOSFET gate potential increases.

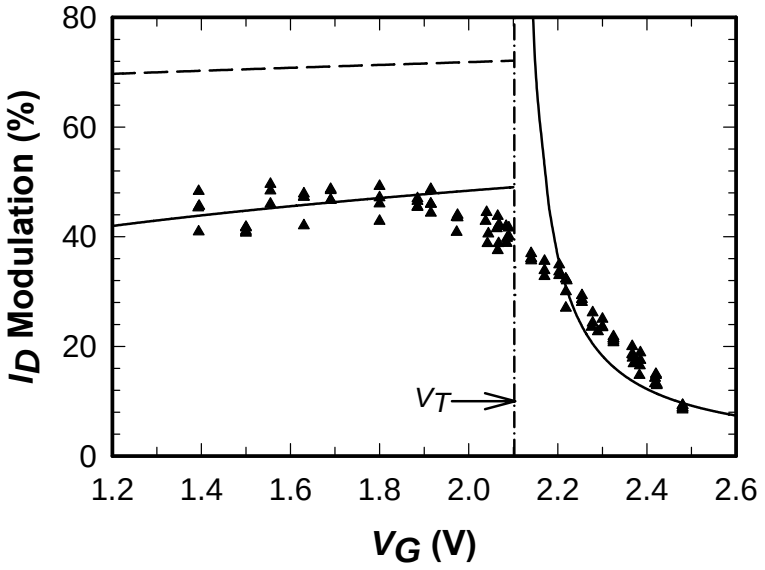

Figure 2.10 Drain current modulation for 9.86 μm-diameter polystyrene beads as a function of the gate potential with $V_- = -29\,\mathrm{V}$ and $V_{DS} = 0.15\,\mathrm{V}$. V_+ is adjusted to obtain different gate potentials on the MOSFET. The points represent experimental data and the solid curves represent theoretical prediction from Eqs. (2.6) and (2.9). The dashed line represents the approximate theoretical prediction in the sub-threshold regime from Eq. (2.10).

The theoretical prediction of the MOSFET drain current modulation as a function of the gate potential is also calculated and presented in Fig. 2.10. In the saturation regime, the theoretical curve based on Eq. (2.6) fits the experimental results very well except in the transition region close to the threshold voltage. However, significant difference is observed between the experimental results and the theoretical prediction based on Eq. (2.10), when the MOSFET works in the sub-threshold regime. This discrepancy indicates that the assumption of $\psi_S \approx V_G$ is not a good approximation in this case. Therefore, we fitted the experimental data in the sub-threshold regime to Eq. (2.9), which reflects the more realistic performance of the MOSFET. A set of fit parameters of $a = 6.6$ and $V_{FB} = -0.3\,\mathrm{V}$ yielded an acceptable theoretical curve that fits the experimental data well. These values are reasonable as the typical value of a ranges from 0.3 – 30, and V_{FB} depends on the material used for the gate metal and typically ranges from -0.5 to 0.5 V (Sze, 1981).

One more point we would like to point out is that the vertical spread of the experimental data can be attributed to the intrinsic size dispersion of the 9.86 μm polystyrene beads used. It is worth noting that the vertical spread of the data is greater in the sub-threshold regime compared to that in the above-threshold regime, which indicates that the device is more sensitive to the resistance change caused by the bead size dispersion when the MOSFET is operating in the sub-threshold regime since the total amplification factor is larger in this region as shown in the previous sub-section.

Device Sensitivity as a Function of the Electrical Bias

As seen in Eq. (2.11), the amplification factor is also a function of the ionic current through the fluidic circuit, and hence a function of the applied electrical bias. The device sensitivity is expected to vary linearly with V_- because ideally, the IR_1 term in Eq. (2.11), is equal to $V_G - V_-$. The drain current modulation from the approximate expression in Eq. (2.10) when the MOSFET is operating in the sub-threshold regime is then

$$\frac{\Delta I_D}{I_D} \approx \left(\frac{q}{kT} - \frac{1}{2V_G}\right)(V_G - V_-)\left(\frac{R}{R_t}\right)\frac{\Delta R}{R}. \tag{2.12}$$

The dependence of the drain current modulation on V_- is similar in the saturation regime because the IR_1 substitution made in Eq. (2.12) is the same.

The drain current modulation of 9.86 μm-diameter polystyrene beads is measured as a function of V_-, while holding the MOSFET gate potential constant at about 1.81 V. The MOSFET is operating in the sub-threshold regime. In this experiment, when V_- is changed, the constant gate potential is achieved by adjusting V_+ accordingly to keep the measured MOSFET drain current constant. Figure 2.11 shows the performance of the microfluidic device as a function of V_- and a linear relationship between the drain current modulation and V_- is clearly observed as expected.

Theoretical prediction based on Eq. (2.12) is also presented in Fig. 2.11 as the dashed line and again, significant discrepancy exists between the experimental results and the theoretical curve, which confirms the observation in the previous sub-section that the

approximation leading to Eq. (2.10) may not be suitable for our experiments. We then performed the theoretical prediction based on Eq. (2.9) with the same fitting parameters ($a = 6.6$, $V_{FB} = -0.3$ V) as in the previous sub-section, shown in Fig. 2.11 as the solid line, and a much better match between theory and experiment is observed. We are unable to measure the drain current modulation for $|V_-| < 29$ V since the electroosmotic flow is very slow and most of the beads stick to the channel walls after a short time of experiment.

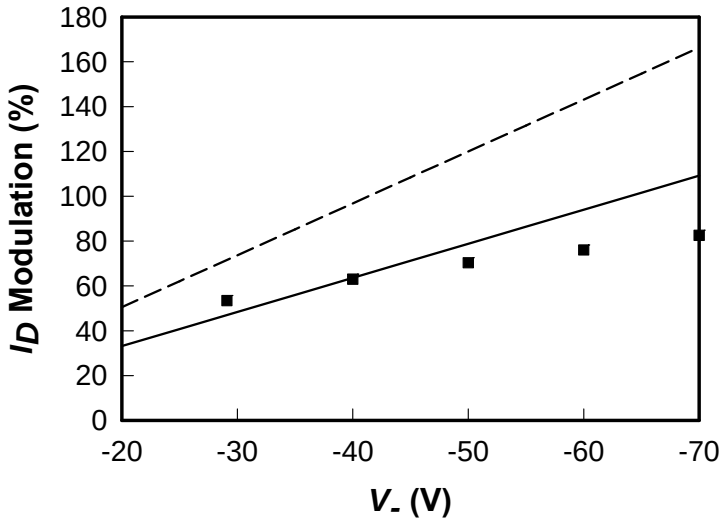

Figure 2.11 Drain current modulation for 9.86 μm polystyrene beads as a function of V_-, for constant gate potential of ~1.81 V and $V_{DS} = 0.15$ V. The points represent experimental data; the solid line represents theoretical prediction from Eq. (2.9) and the dashed line represents theoretical prediction from Eq. (2.10).

Characterization of the Size Distribution of Microbeads

One function of standard Coulter counters is to determine the size of small particles.

To characterize the MOSFET-based sensor's ability of determining the size distribution of microbeads, we measured the size distribution of the nominally monodisperse 9.86 μm-diameter polystyrene beads with the MOSFET-based microfluidic sensor. We also measured the diameter distribution of the polystyrene beads with a scanning electron microscope (Raith eLiNE SEM). The manufacturer of microbeads (Bangs Laboratories, Inc.) quoted nominal mean sphere diameter of the beads as 9.86 μm with a standard deviation of 0.65 μm, as measured with a Coulter Principle-based particle sizer. The measurement with the MOSFET-based microfluidic sensor was performed with the following parameters: $V_{-} = -29\,\mathrm{V}$, $V_{+} = 11\,\mathrm{V}$, and $V_{DS} = 0.15\,\mathrm{V}$, leading to $V_G \sim 1.79\,\mathrm{V}$. Thus, the MOSFET was working in the sub-threshold regime.

Figure 2.12(a) shows the size distribution of the 9.86 μm-diameter beads obtained with the SEM, in which the vertical bars represent a histogram of experimental data and the curve represents a Gaussian fit to the data. The diameters of 199 microbeads in total were directly measured using the SEM, and a mean microbead diameter of 9.82 μm with a standard deviation of $\sigma = 0.29$ μm was obtained from the Gaussian fit to the experimental data. Thus, the direct SEM measurements showed that the size distribution of the 9.86 μm beads was about half of the quoted value from the bead manufacturer. Figure 2.12(b) shows the distribution of drain current modulation observed using the MOSFET-based microfluidic sensor when 9.86 μm in diameter polystyrene beads were translocated through the sensing channel. The total number of sample particles was kept the same as that for the SEM measurement, and from the

Gaussian fit to the data, a mean drain current modulation of 54.4%, with a standard deviation of $\sigma = 1.95\%$, was obtained.

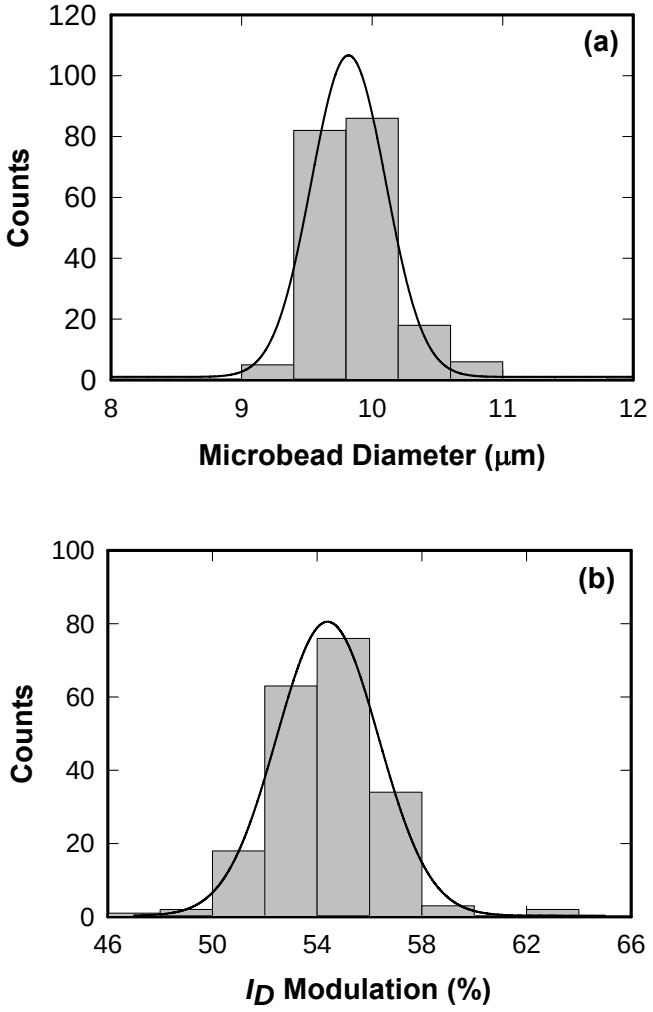

Figure 2.12 (a) Size distribution of 9.86 μm-diameter polystyrene beads obtained from SEM measurements, (b) Distribution of drain current modulation observed for 9.86 μm-diameter beads. Vertical bars represent a histogram of experimental data and lines represent a Gaussian fit to the data.

To enable a direct comparison between the size distribution determined by the SEM measurement and that obtained from the drain current modulation measurement with the

MOSFET-based microfluidic sensor, experimental data were normalized by the mean of

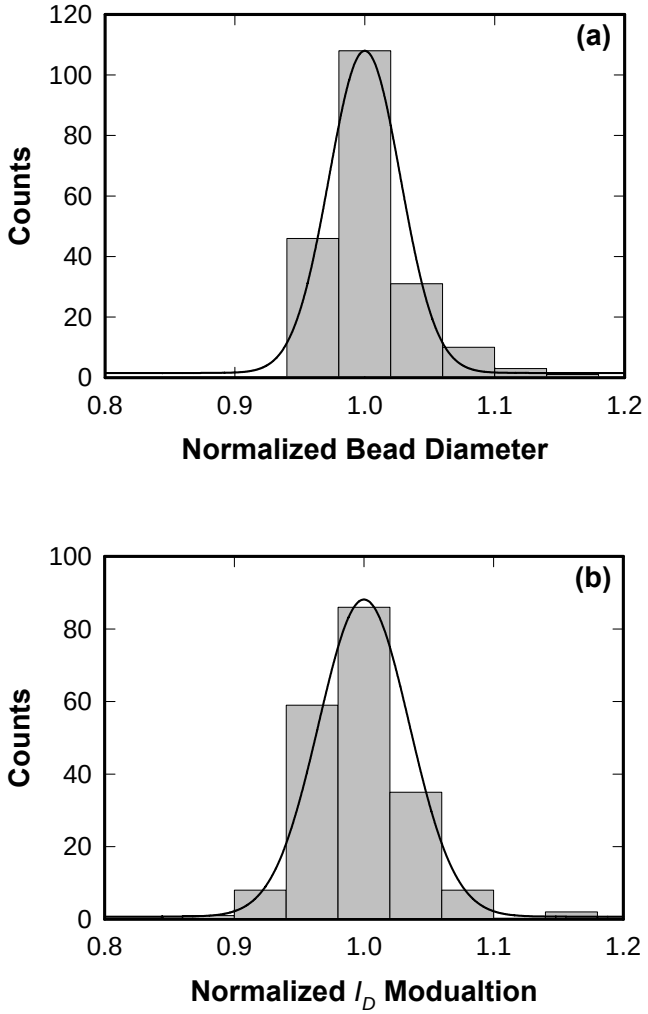

Figure 2.13 (a) Normalized size distribution of 9.86 μm-diameter beads obtained by the direct SEM measurement. The normalized mean was 1.0 and the standard deviation was 0.028. (b) Normalized size distribution of 9.86 μm-diameter beads obtained using the MOSFET-based microfluidic sensor. The normalized mean and standard deviation were 1.0 and 0.035 respectively.

the respective Gaussian distribution: 9.82 μm for the SEM data and 54.4% for the MOSFET drain current modulation. Figure 2.13(a) shows the normalized data from the

SEM measurement and Fig. 2.13(b) shows the normalized data from the MOSFET-based microfluidic sensor measurement. Because of the normalization, the means in both Fig. 2.13(a) and 2.13(b) are 1.0. The standard deviation for the normalized SEM data shown in Fig. 2.13(a) is 0.028 and the corresponding value for the normalized MOSFET-based microfluidic sensor data shown in Fig. 2.13(b) is 0.035. Therefore, the size distribution of 9.86 μm in diameter beads measured with the above two techniques matches with each other very well.

It is worth noting that for the normalized size distribution of spherical particles, we expected the standard deviation from the MOSFET-based microfluidic sensor to be 3 times of the standard deviation from the diameter measurement through a SEM, as the signal from the microfluidic sensor is proportional to the volume of the beads. However, the observed standard deviation from the microfluidic sensor is only slightly higher than that from the SEM measurement. A full analysis of this difference will depend on understanding the intrinsic resolution of each probe and the manner in which the resolution function couples to the actual data.

Cell Counting

We also performed cell counting with our MOSFET-based microfluidic device, which is a major application of the traditional Coulter counter. Figure 2.14 shows the measured MOSFET drain current, I_D, for CD4+ T lymphocyte cells when

$V_{DS} = 0.15\,\text{V}$, $V_{-} = -29.0\,\text{V}$, and $V_{+} = 6.0\,\text{V}$, respectively. The gate potential determined from the I_D-V_G curve is ~ 1.6 V, smaller than $V_T = 2.1\,\text{V}$, and therefore the MOSFET is working in the sub-threshold regime. It is interesting to note that the drain current modulation for some cells shows an enhancement-blockade pattern (labeled as I), i.e. an upward drain current peak immediately followed by a drain current dip when a cell passes through the sensing channel, in contrast to the normal blockade pattern (labeled as II). The ionic current enhancement modulation has been reported in the literature for the translocation of DNA molecules though nanochannels (Chang et al., 2004; Fan et al., 2005; Smeets et al., 2006) and several recent measurements (Jagtiani et al., 2006; Zhe et al., 2007) reported the decrease of the sensing channel resistance for Juniper tree pollens, which is equivalent to an ionic current enhancement. However, we have not found a good explanation of the enhancement-blockade pattern in the literature.

We believe that this phenomenon can not be explained in the same way as in the above literature, i.e., the enhancement is due to the increase of the counter-ions in the channel that are shielding surface charges of the cell. The typical electric field in the electric double layer surrounding a small particle is on the order of 10^5 V/cm, while the applied electric field in the sensing channel is only around 300 V/cm. The applied electric field is orders of magnitude smaller than the electric field of the electric double layer, and it is doubtable that the applied electric field will strip off the counter-ions adsorbed on the cell surface to contribute to the total number of mobile ions in the electrolyte. A more possible reason is probably related to the special property of the cell

surface. The cell membrane has many ion channels that ions and molecules can transport through. When the cell moves into the small sensing channel, the cell experiences a sudden change of the applied electric field. This might lead to release of extra conducting molecules or ions into the electrolyte, and hence enhance the conductance of the channel. After these released conducting molecules or ions move out of the channel under the applied electric field, the slow moving cell will lead to the reduced conductance and hence a current dip. While the above explanation is not confirmed by any solid experimental evidence, the true underlying mechanism of the current enhancement-blockade pattern is not clear yet and is an interesting topic for further research.

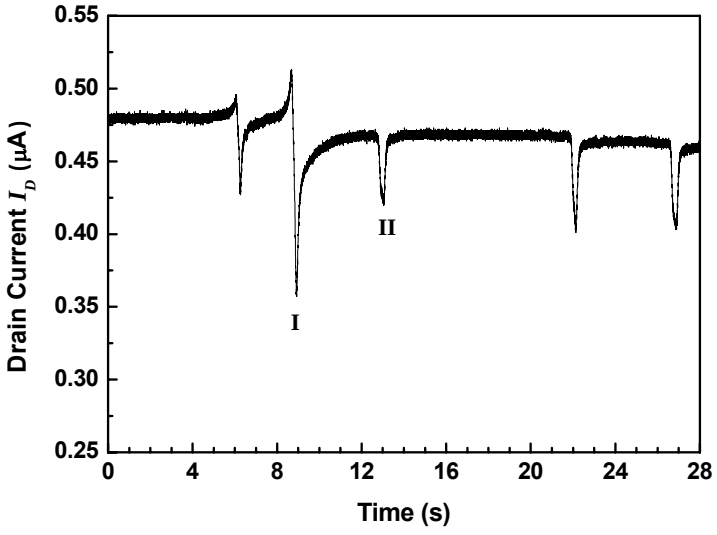

Figure 2.14 Drain current of the MOSFET for the CD4+ T lymphocyte cells. MOSFET is working in the sub-threshold regime.

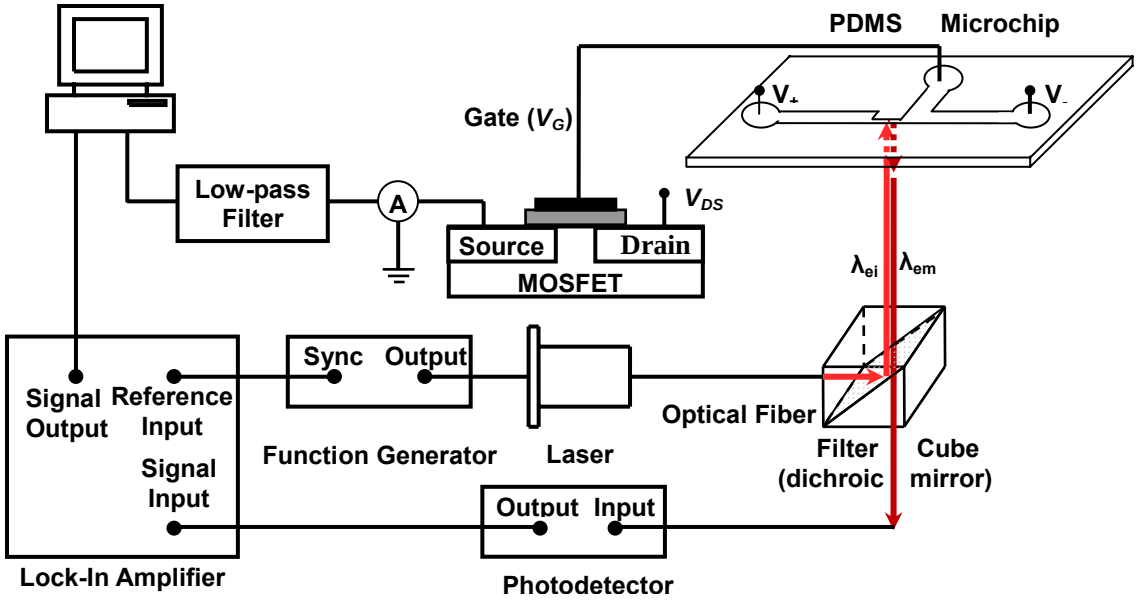

Figure 2.15 Schematic of the experimental setup combining the MOSFET-based microfluidic sensor with a fluorescence detection system (schematic courtesy of Yao-Nan Wang, Vanderbilt University)

In addition to the pure counting of cells, we have integrated the MOSFET-based sensing technique with a laser-induced fluorescence detection technique (implemented by Dr. Dongqing Li's group), and demonstrated the ability to determine the percentage of the CD4+ T cells tagged with a specific fluorescent dye. Figure 2.15 shows the schematic of the experimental setup integrating the two techniques. Since the MOSFET-based sensing technique has been extensively discussed above, here we will only briefly describe the fluorescence detection system.

As shown in Fig. 2.15, the microfluidic device is mounted horizontally on a hollow metal platform. An optical fiber (200 μm in diameter, Silicon Lightwave Technology, CA) is fixed in a movable cartridge that is installed underneath the platform. The open

tip of the optical fiber is arranged orthogonally opposing the left end of the sensing channel. The precise alignment between the sensing region and the optical fiber is achieved by an XYZ 3-axis travel translation stage and an XY translator (Thorlabs, Newton, NJ). An optical microscope (SMZ800, Nikon Instrument Inc.) with high intensity polarizing attachment illuminator (NI 150, Nikon Instrument Inc.) and a CCD camera (Qimaging, Vancouver, British Columbia, Canada) are used to monitor the alignment.

The fluorescence excitation is achieved with a 25 mW single mode diode laser (wavelength of 635 nm, Blue Sky Research, CA) and is modulated by a function generator (DS 350, Stanford Research Systems, Sunnyvale, CA) at a frequency of 13 Hz. The synchronous signals of the function generator are fed into a lock-in amplifier (SR 850, Stanford Research Systems, Sunnyvale, CA) as a reference input. The modulated laser goes through a filter cube (OZ Optics, Canada) and is reflected into the sensing fiber by a dichroic filter. The laser beam is focused at the upstream end of the sensing channel. When the stained cells pass through the sensing channel, the fluorescent tag is excited. The incident emission penetrates the glass substrate and is transmitted by the fiber back to dichroic filter and a band pass filter (670 nm). The optical signal is converted into electrical signal by a photo-detector (C5460-01, Hamamatsu, Japan) and detected by the lock-in amplifier. The output signal is recorded and visualized by a custom-made LABVIEW® code through a data acquisition board (PCI 6281, National Instruments, Austin, TX).

In this experiment, V_+, V_-, and V_{DS} were set as 8.9 V, -29 V, and 0.15 V, respectively. When a cell is passing through the sensing channel, whether the cell is fluorescently tagged or not, it will generate a pulse in the MOSFET drain current since it modulates the conductance of the sensing channel. But only those cells tagged with a fluorescent dye will simultaneously show a peak in the fluorescence signal.

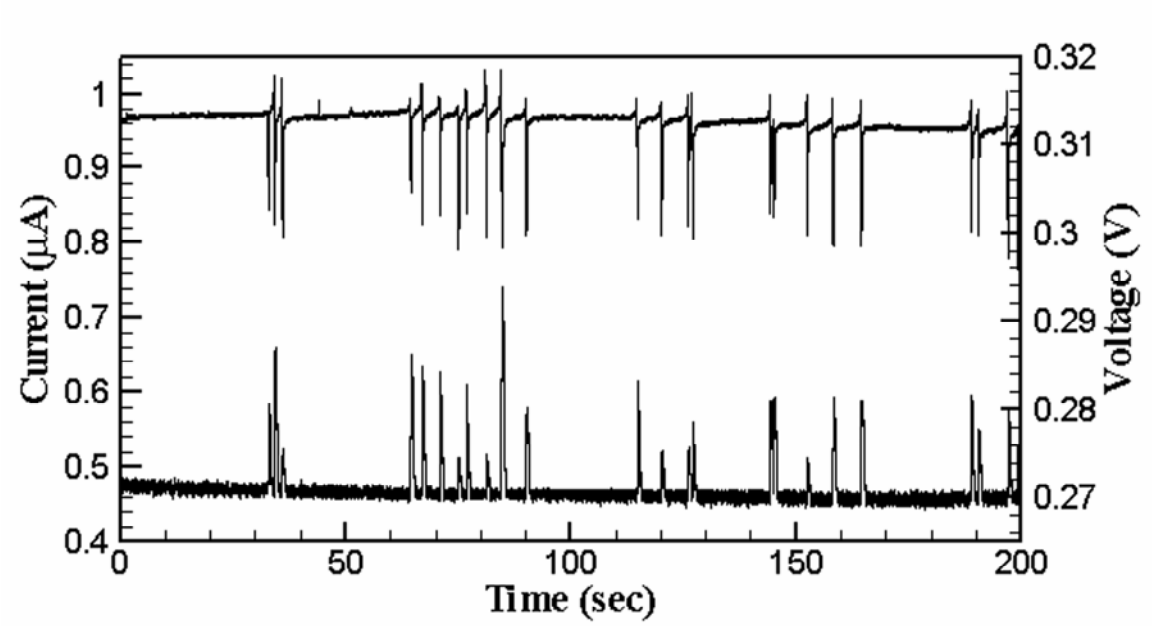

Figure 2.16 Drain current of the MOSFET (upper) and fluorescence intensity (lower, given in voltage) recorded for 100% stained CD4+ T cells.

In order to test the performance of our system, 100% stained CD4+ T cell suspension is first added in the microfluidic device and the typical MOSFET drain current signal and the corresponding fluorescence signal are given in Fig. 2.16. For the MOSFET drain current, each downward spike indicates a cell and the depth of the spike is proportional to the volume ratio of the cell to the sensing channel. Important

information such as the total number and the size distribution of the cells passing through the sensing channel within a specific period of time can be derived from the drain current monitoring. For the fluorescence signal (given in voltage), each spike denotes a fluorescence-tagged cell and its amplitude indicates fluorescent light intensity. Combining the results from these two systems, we can obtain the total number of the cells and also the percentage of a cell subset tagged with a specific fluorescent dye. Since all the cells are fluorescent in this experiment, each MOSFET drain current pulse corresponds to a fluorescence signal spike. The one-to-one correspondence of the signals from the two sub-systems can be clearly seen from Fig. 2.16, indicating that two sub-systems are highly synchronous.

50% stained cell suspension is also driven through the fluidic device to test the accuracy of percentage determination and the recorded MOSFET drain current and fluorescence signals are shown in Fig. 2.17. MOSFET signal shows the total number of the cells, whereas the fluorescence signal only shows those cells tagged with a fluorescent dye. From these results, we can justify exactly which cell is fluorescent and the percentage of the labeled cells in total cells can be determined. Five tests were conducted individually with each one lasting about 11~12 minutes and the results are listed in Table 2.1. The average percentage of the stained cells is 48.7% which matches the exact percentage quoted from a commercial flow cytometer (BD Immunocytometry Systems, San Jose, CA) for the same sample, 46.1%, very well. The gate potential of

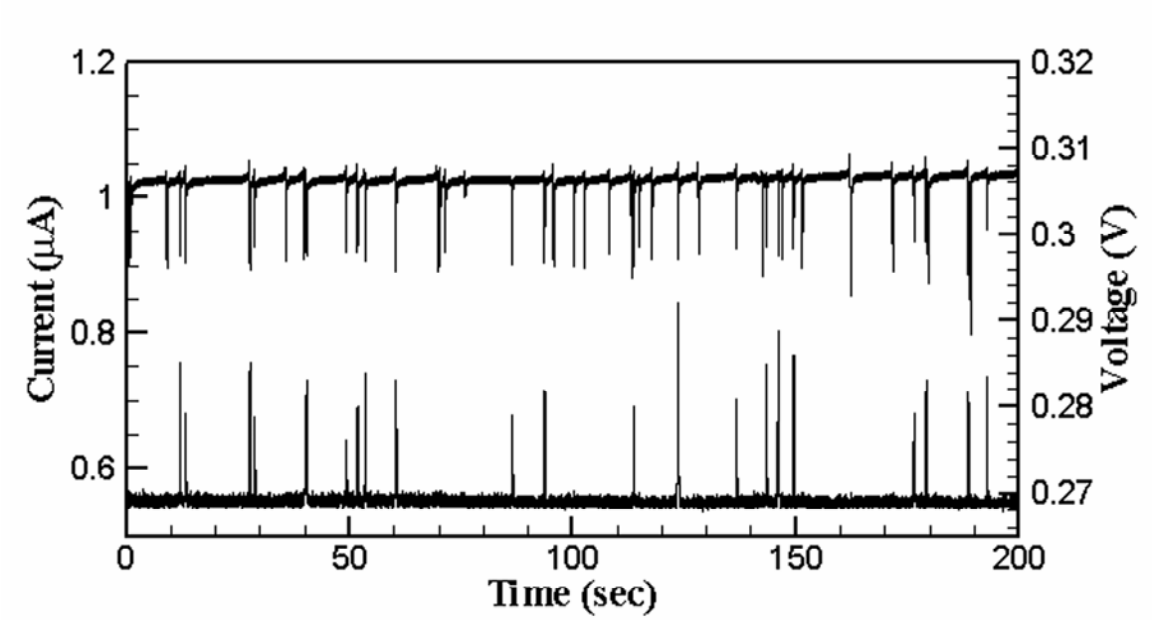

Figure 2.17 Drain current of the MOSFET (upper) and fluorescence intensity (lower, given in voltage) recorded for nominally 50% stained CD4+ T cells.

Table 2.1 Percentage of fluorescence-tagged cells determined by five individual tests

Test	I	II	III	IV	V	Total
Stained cells #	111	128	155	92	82	568
Total cells #	222	262	290	211	181	1166
Stained cells %	50.0%	48.9%	53.4%	43.6%	45.3%	48.7%

the MOSFET, inferred from the I_D-V_G curve, is about 1.66 V, with the MOSFET working in the sub-threshold regime. As shown in the upper plot in Fig. 2.17, different cells generate different pulses in the MOSFET drain current, which indicates that the sizes of cells are not very uniform, and the baseline drain current (1.02 μA) can decrease to a wide range of 0.8 μA ~ 0.95 μA, or 7~20% modulation. Since the typical amplification factor in sub-threshold regime is about 65 (as seen in the section

'Amplification Effects in Different Working Regimes'), the channel resistance modulation $\Delta R/R$ can be calculated by using Eq. (2.9), which ranges from 0.11% to 0.31%. The volume ratio of the cell to the channel is approximately the modulation of the sensing channel resistance, when the cell diameter is small compared to the channel cross-section. Therefore, the diameter of the cell can be roughly determined to be 5.33 μm ~ 7.53 μm.

Noise Analysis

The sensitivity of any experimental measurement is ultimately limited by noise and a more sensitive sensing scheme has to provide a higher signal to noise ratio. The MOSFET-based microfluidic sensor provides a higher percentage modulation to the baseline MOSFET drain current compared to the percentage modulation to the baseline ionic current signal for traditional Coulter-type sensors. However, the concept will work only if the noise level does not increase to the same extent. If we define the noise level as the ratio of the peak to peak value of the noise to the average baseline value of the signal (either ionic current or MOSFET drain current), then in our measurement, the noise level of the ionic current through the fluidic circuit we observed is about 0.3% (as seen in Fig. 2.5), and the noise level of the MOSFET drain current is around 0.5-0.9% (as seen from Figs. 2.4, 2.7, and 2.8, etc.), which varies from one experiment to another. Note that the noise level of the ionic current in the literature ranges from ~ 0.02% (DeBlois & Bean, 1970) to more than 10% (Heng et al., 2004), so the noise level we

observed is comparable to those reported in the literature. As discussed in the last section 'Characterization of the MOSFET-Based Microfluidic Sensor', the percentage of modulation can be magnified from 40 to 80 times depending on the working regime of the MOSFET and applied electrokinetic bias. In comparison, the noise level of the MOSFET drain current is only 2 to 3 times higher than that of the ionic current through the fluidic channel. So compared to the traditional Coulter counters, the reported MOSFET-based microfluidic sensor demonstrates an enhanced sensitivity of up to 40 times. (The sensitivity here is defined as the ratio of the percentage modulation from the particles to the noise level).

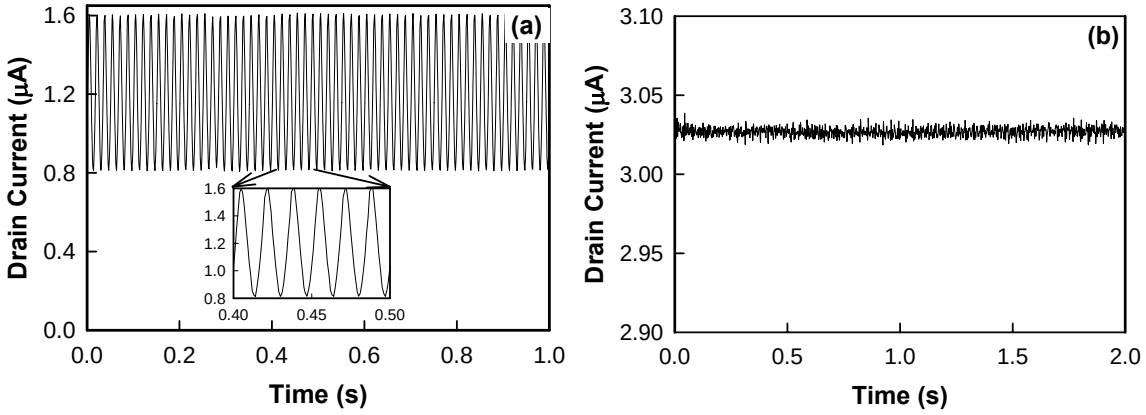

Figure 2.18 Recorded noise when the rise time of the current pre-amplifier is set as 0.3 ms. (a) Without a Faraday cage, the noise is ~67% of the baseline signal and is mainly 60 Hz. The inset shows that six peaks appear within 0.1 s. (b) With a Faraday cage, the noise is less than 0.66% of the baseline drain current.

It is worth noting that we did not shield our experimental setup using a Faraday cage in all the experiments reported in the last section, because at the experimental

characterization stage we wanted to perform concurrent optical observation to validate the electrical signals. The noise suppression in all the above experiments is mainly achieved by using a relatively large rise time of the current preamplifier (100 ms) and a low cut-off frequency (30 Hz) of the low-pass filter, which may not be desirable for some applications. Further noise characterization shows that if shorter rise time is used, the observed noise is mainly 60 Hz noise, which can be eliminated by using a Faraday cage. As shown in Fig. 2.18(a), if the rise time of the current preamplifier is set to be 0.3 ms, the noise level is 67% of the baseline MOSFET drain current without a Faraday cage and the noise is mainly 60 Hz noise. However, if we shield the measurement set up with a Faraday cage, the noise level is only about 0.66% of the baseline MOSFET drain current, as shown in Fig. 2.18(b). This noise can be further reduced by applying a low-pass filter, and using Ag/AgCl electrodes, etc. For example, using a low-pass filter with a 1 kHz cutoff frequency reduces the noise from ~0.66% to ~0.4%, which is nearly the same as that of the ionic current. These methods allow the new sensing scheme to be applied to the applications with a short particle translocation time.

We also tried to detect the translocation of 6 μm-diameter polystyrene beads through the same microfluidic device with the experimental setup shielded by a Faraday cage and the recorded drain current of the MOSFET is shown in Fig. 2.19 (a). In this experiment, the power supplies were set as $V_{DS} = 0.15$ V, $V_{+} = 9.03$ V, $V_{-} = -26.3$ V. The rise time of the current preamplifier was 0.3 ms and the cutoff frequency of the low-pass filter

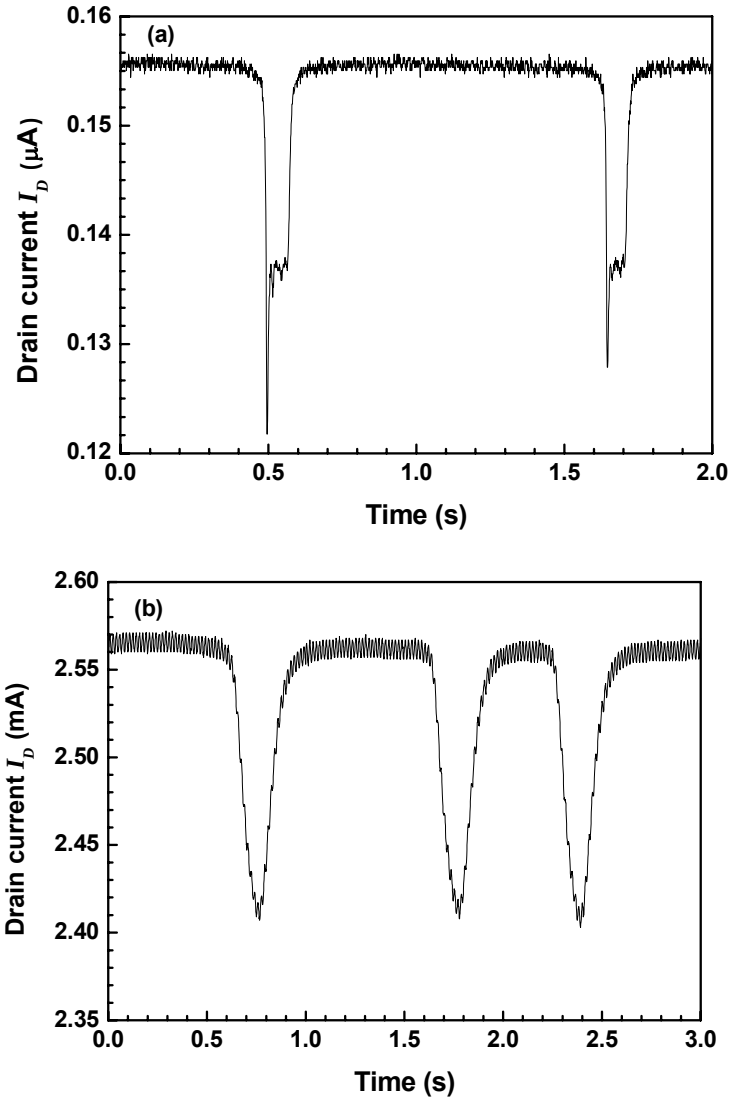

Figure 2.19 Drain current of the MOSFET recorded for a suspension containing 6 μm-diameter polystyrene beads. (a) The setup is shielded with a Faraday cage. The rise time of the current preamplifier is set as 0.3 ms and the cutoff frequency of the low-pass filter is 100 Hz. (b) The setup is not shielded with a Faraday cage. The rise time of the current preamplifier is set as 100 ms and the cutoff frequency of the low-pass filter is 30 Hz.

was 100 Hz. The previous result recorded for the 6 μm polystyrene beads is also shown in Fig. 2.19 (b) for the purpose of comparison. In this case, the experimental setup was not shielded with the Faraday cage and the rise time of the current preamplifier and the

cutoff frequency of the low-pass filter were set as 100 ms and 30 Hz, respectively. Figure 2.19 shows that the pulse shape recorded with a short rise time of 0.3 ms is very close to the ideal square pulse, while the signal obtained with a long rise time of 100 ms is severely distorted and almost a triangle pulse. On the other hand, the overshooting of the drain current pulse is observed when a particle is entering the sensing channel, which may be due to the sudden resistance and capacitance change caused by the particle.

The true advantage of the MOSFET-based microfluidic sensor is that the design amplifies the percentage of the resistance modulation locally. The noise of a Coulter-type sensor can come from three sources, i.e., the electrical noise from the measurement instruments external to the fluidic circuit, the noise from the electrodic interactions at the electrode-electrolyte interface, and the fluidic circuit itself. Recently, there have been several discussions about the noise of nanopore-based Coulter-type sensors (Siwy & Fulinski, 2002; Chen et al., 2004; Smeets et al., 2006; Tabard-Cossa et al, 2007). All of these reports indicate that low-frequency (1/f) flicker noise is the dominant source of noise in nanopore-based Coulter-type sensors. The origins of this noise remains unknown but surface effects like the inhomogeneity of the surface charge on the pore wall (Chen et al., 2004), nanobubble formation (Smeets et al., 2006), and the underlying motions of biological membrane channels (Siwy & Fulinski, 2002) have been proposed as possible sources for the flicker noise.

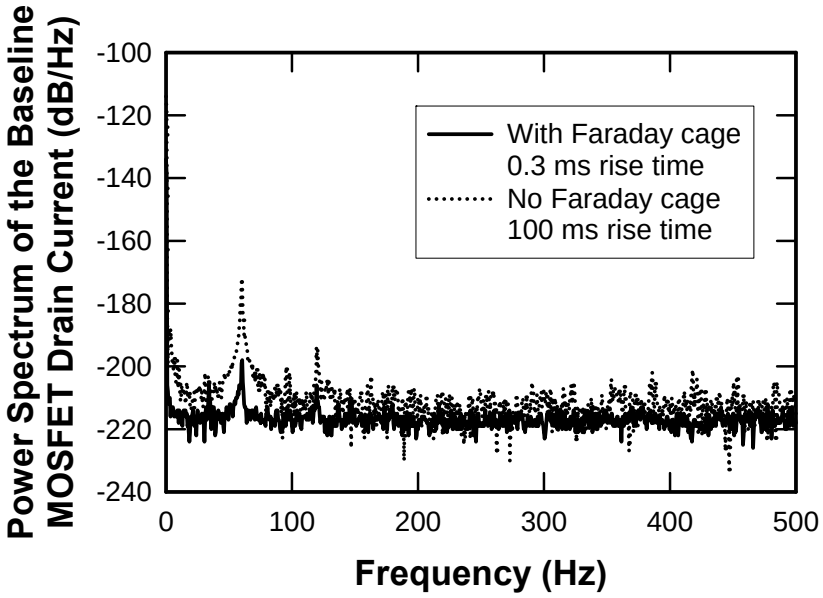

Figure 2.20 Power density spectrums (PDS) of the baseline MOSFET drain current with and without a Faraday cage.

To better understand the noise source in our measurement system, we performed spectral analysis of our data. Figure 2.20 shows the power spectra of measured baseline MOSFET drain current for two cases: no Faraday cage with 100 ms rise time setting for the current preamplifier, and with Faraday cage with 0.3 ms rise time setting for the current preamplifier. The power spectra are in the unit of db with a reference of 1 A^2. The solid line shows the power density spectrum (PDS) of the baseline MOSFET drain current when the experimental setup was shielded with a Faraday cage, and the dotted line shows the power density spectrum of the baseline MOSFET drain current when a Faraday cage was not used. Figure 2.20 indicates that in addition to the 1/f flicker noise at very low frequency (<10 Hz), noise at 60 Hz and its harmonic frequencies presents in our measurement. Figure 2.20 also shows that the 60 Hz noise can be reduced to an

acceptable level by either using a long rise time for the current preamplifier or using a Faraday cage.

Summary

In summary, a new sensing scheme has been developed by integrating a three-terminal fluidic circuit with a MOSFET and detects particles by measuring the drain current of the MOSFET, instead of directly measuring the ionic current in the fluidic circuit. Theoretical analysis shows that the resistance modulation of the sensing channel due to the presence of the particle can be amplified by both the fluidic circuit and the MOSFET and the sensitivity can be improved substantially. This new sensing scheme is first implemented at the microscale level and a MOSFET-based microfluidic sensor made of PDMS channels has been fabricated and extensively tested with various micron-sized particles. We experimentally demonstrate that amplification can be achieved from both the fluidic circuit and the MOSFET. The lowest volume ratio detected with the microfluidic device is 0.006%, ~10 times lower than the detection limit based on the traditional Coulter principle as reported in the literature. The device is shown to be able to distinguish particles of similar sizes but different surface charges. By integrating with a fluorescence detection system, the device can also be used to determine the percentage of the cells tagged with a specific fluorescence dye.

CHAPTER III

MOSFET-BASED NANOFLUIDIC SENSORS

One important trend in the development of the resistive pulse sensing technique is to design and fabricate various nanofluidic sensors to detect nanoparticles or single DNA molecules. In chapter II, it has been demonstrated that the new MOSFET-based sensing scheme can improve the sensitivity substantially by tuning the design of the fluidic device and the working regimes of the MOSFET. The same sensing scheme is also implemented at the nanoscale to detect nanoparticles as detailed in this chapter.

Design and Fabrication of the Nanofluidic Device

Different from the three-terminal design of the microfluidic sensor we used before, a four-terminal layout is adopted in the nanofluidic device as shown in Fig. 3.1. Two microchannels, which connect to each end of the sensing nanochannel, were originally designed for the assistance of the particle delivery through the sensing channel. Since there is a nanochannel in between the inlet and outlet reservoirs (A and B), it was expected that the flow rate of the electroosmotic flow in the horizontal channel would be low which might not be strong enough or would take a really long time to deliver nanoparticles through the sensing channel. Therefore, we adopted the current design with four terminals. The large microchannels either between reservoirs B and D or

between A and C can be used to first deliver nanoparticles quickly to the vicinity of the sensing nanochannel by applying an electrical bias to generate electroosmotic flow; then the electrical bias can be switched to reservoirs A and B to drive particles through the sensing channel. However, experiments show that it is still difficult to deliver nanoparticles by electroosmotic flow even with the way described above since the particles tend to stick on the bottom of the fluidic channel very easily. As a result, we carefully choose sample nanoparticles with high negative surface charge densities and deliver the particles with electrophoretic motion. Another favorable feature of the current design is that either of two vertical microchannels can be connected with the gate of a MOSFET and it is more flexible when tuning the working regime of the MOSFET.

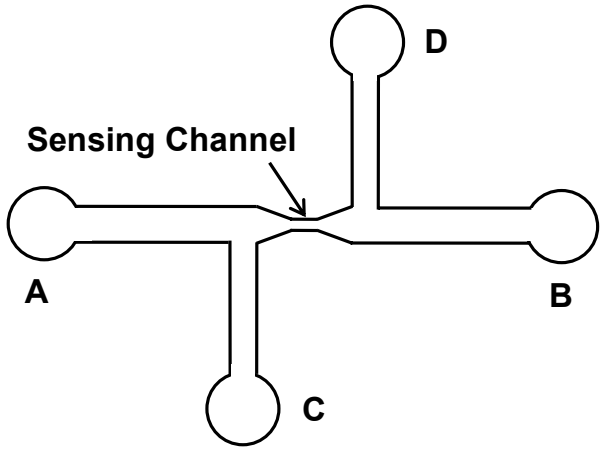

Figure 3.1 Schematic of the nanofluidic device (not to scale). The sensing channel is 5 μm long with a cross section of 500 nm by 500 nm.

In the nanofluidic device, the sensing channel is 5 μm long with a cross section of

500 nm by 500 nm. The microchannel connecting to reservoir A is 10 mm long and 10 μm wide. The channel connecting to reservoir B is 5 mm in length and 50 μm in width. The dimensions of two vertical channels are same and the channel length and width are 2 mm and 100 μm, respectively. The shapes of the joint segments between the nanochannel and microchannels are not well-specified and the dimension is not given here. The reflection image of the sensing region of the nanofluidic device is shown in Fig. 3.2, which is taken under an inverted optical microscope. The depth of all the microchannels is 5 μm, while the nanochannel and the joint segments are 500 nm deep.

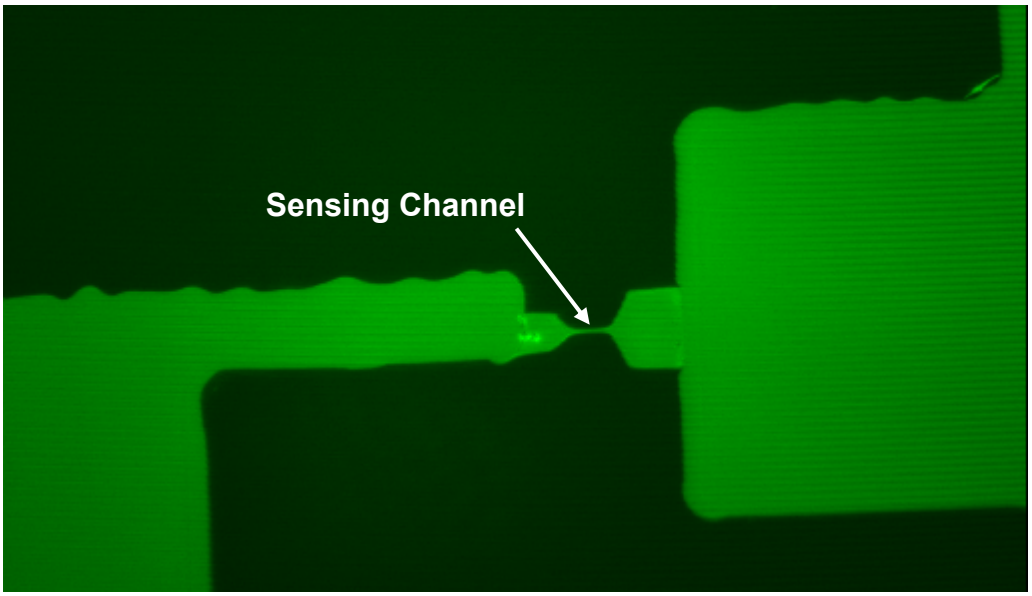

Figure 3.2 Image of the sensing channel region of the nanofluidic device taken under an inverted optical microscope

Similar to the microfluidic sensor, the nanofluidic device is also fabricated by the

micromolding method. First, a negative master of the nanochannel, connecting microchannels, and reservoirs is created on a silicon substrate. Then the pattern is transferred onto a slab of PDMS. Finally, the PDMS slab is bonded with a glass substrate after being treated with oxygen plasma to form the nanofluidic device. The difference in fabricating nanofluidic devices and microfluidic devices is that the master fabrication for nanofluidic devices is a two-step process:

Step 1: patterning the nanochannel and the joint segments on a silicon substrate;

Step 2: forming the SU8 master for the microchannels and reservoirs.

In order to successfully fabricate the nanofluidic device, mask alignment is required between the above two steps. Therefore, alignment marks also need to be patterned on the silicon substrate in step 1 and alignment windows are designed on the photomask for step 2.

P1: A silicon wafer after Piranha cleaning

P2: Spincoat a thin film of PMMA resist with a thickness of ~ 325 nm

P3: Patterning nanochannels, joint segments, and global marks by electron beam Lithography (EBL) including exposure, development, and bake

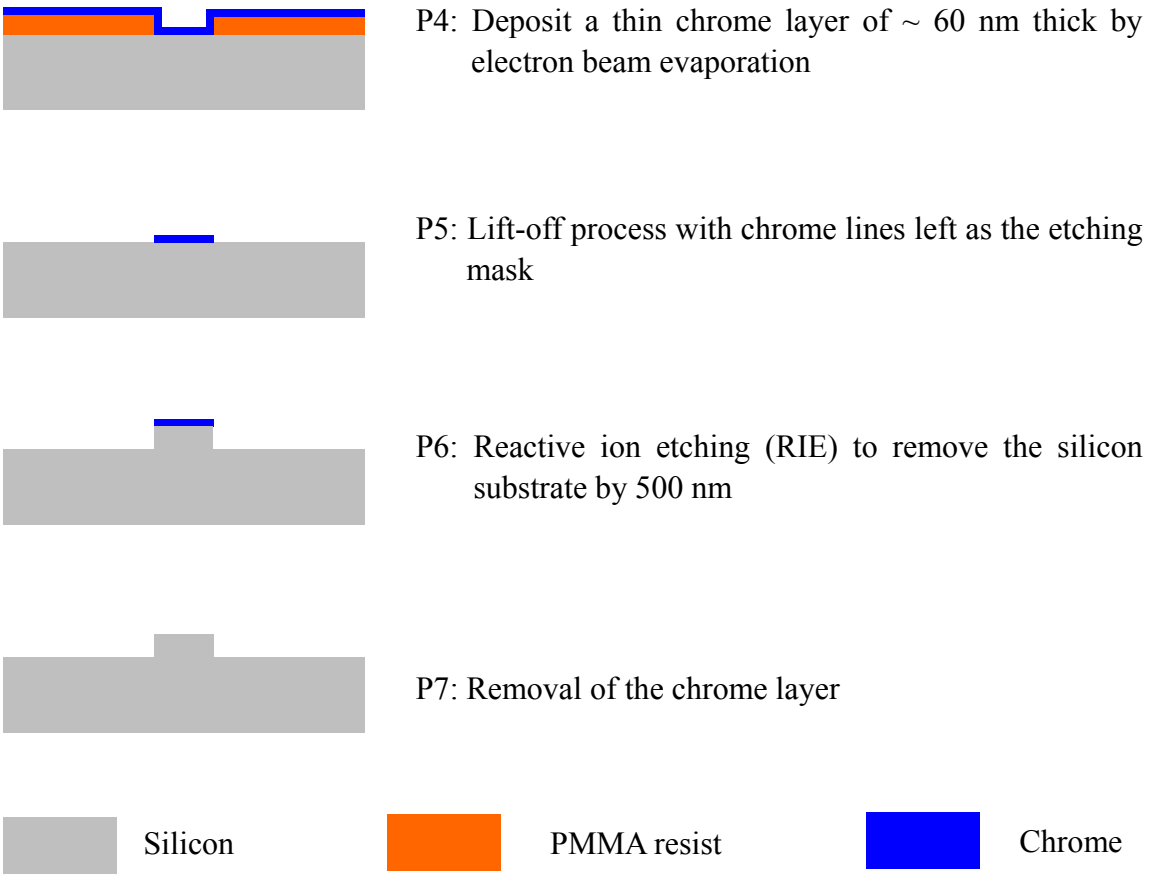

Figure 3.3 Step-by-step fabrication process of a 500 nm-thick negative master of nanochannels and joint segments on a silicon substrate

Figure 3.3 shows the schematic of the step-by-step fabrication process for creating a negative master of nanochannels and joint segments on a silicon substrate. Then, photolithography is used to pattern SU8 photoresist on the same substrate to form the master for microchannels and reservoirs. The fabrication of the mold for nanofluidic devices is now complete and saline treatment is conducted as the last step on the mold to assist PDMS peeling-off. The nanofluidic device can be fabricated by following the same PDMS casting and bonding processes as described in chapter II.

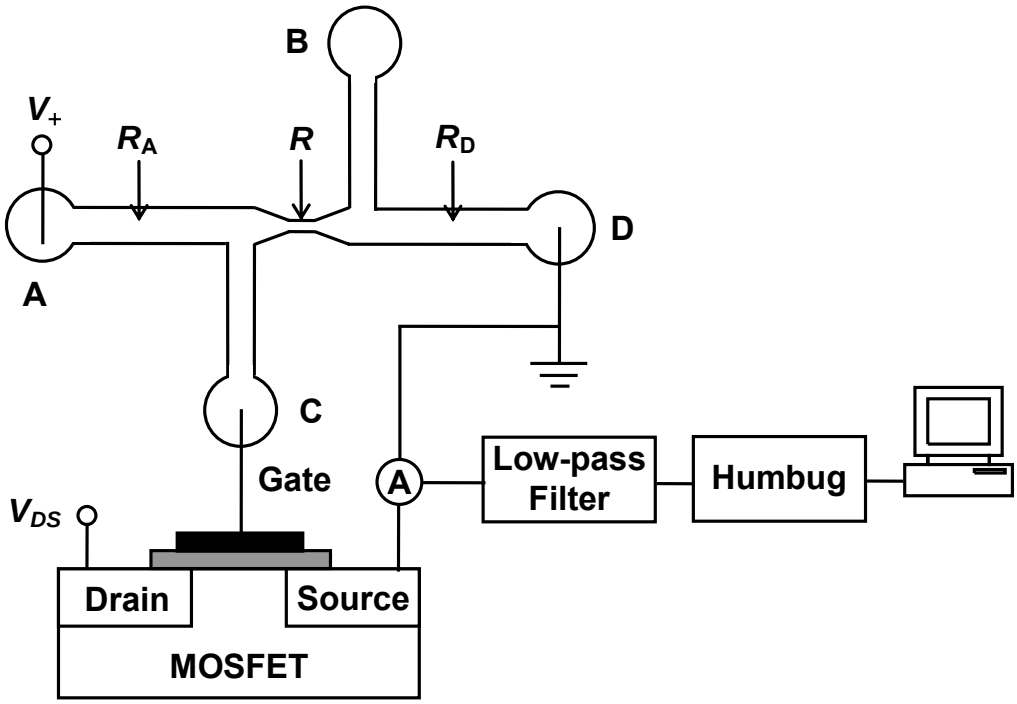

Figure 3.4 Schematic of the experimental setup (not to scale). Power supplies and current preamplifier are commonly grounded.

Experimental Details

Figure 3.4 shows the schematic of the experimental setup for characterizing the nanofluidic sensor, which is not to scale. 100 mM KCl, 10 mM Tris with 1mM EDTA buffer (PH value of 8.0) is used as the conducting medium in the fluidic device. Platinum electrodes are used to connect the fluidic circuit and the electronic circuit. A positive voltage V_+ is applied to reservoir A and reservoir D is electrically grounded. Both reservoirs B and C can be used as the gate branch, although in our current experiments, reservoir C is connected with the gate terminal of the MOSFET to monitor

the change of the local electrical potential. In our experimental setup, the MOSFET drain current is measured by a current preamplifier and the signal passes through a low-pass filter and a Hum Bug noise eliminator in sequence before it is fed into the digital data acquisition system. The Hum Bug constructs a replica of noise present on the input signal and continuously subtracts this replica from the signal and therefore can effectively eliminate 50/60 Hz noise and harmonics. Rise time of the current preamplifier is set as 1 ms and the cutoff frequency of the low-pass filter is 1 kHz. Power supplies for applying V_+ and V_{DS}, reservoir D, and the current preamplifier are commonly grounded in our experiments.

Fluorescent polystyrene nanoparticles of 210 nm in diameter were chosen to test the nanofluidic sensor. The surface of the polystyrene nanoparticles is functionalized with carboxyl groups (COOH/1), so the particles have relatively high negative surface charges and can be delivered by electrophoretic migration. At the beginning of each test, particle suspension prepared with the KCl/Tris/EDTA buffer solution was added into reservoir D and particles were translocated through the sensing nanochannel from reservoir D to reservoir A. In order to assist the visualization of the particle translocation through the fluidic channel, fluorescent particles with dragon green color was chosen and all experiments were conducted under an inverted fluorescent microscope. When nanoparticles are passing through the sensing channel, it will modulate the nanochannel resistance and change the electrical potential at reservoir C locally. As a result, the drain current of the MOSFET will be modulated. We also

presented a theoretical model for the nanofluidic sensor as detailed in the next section.

Theoretical Analysis

In our experiments, the particle suspension is very dilute to prevent from blocking the sensing nanochannel. Therefore, the effect of nanoparticles on the electrical resistances of the microchannels is very small and can be neglected. Denoting the resistances of the three segments of the horizontal channel as R_A, R, and R_D, as shown in Fig. 3.4, when the nanochannel is only filled with the buffer solution, the ionic current (I) in the fluidic circuit can be calculated by

$$I = \frac{V_+}{R_A + R + R_D}, \tag{3.1}$$

and the gate voltage (V_G) of the MOSFET can be written as

$$V_G = V_+ - IR_A. \tag{3.2}$$

Assuming that the resistance of the sensing nanochannel is increased by ΔR upon the translocation of a nanoparticle, the ionic current (I^*) can be expressed as

$$I^* = \frac{V_+}{R_A + R + \Delta R + R_D}, \tag{3.3}$$

and the gate voltage (V_G^*) is correspondingly changed to be

$$V_G^* = V_+ - I^* R_A. \tag{3.4}$$

When a particle is translocated through the sensing channel, the channel is partially blocked and the ionic current in the fluidic circuit will decrease, i.e. $I^* < I$ as seen from Eq. (3.3). As a result, the gate voltage will increase and an upward spike is expected to

be observed in the drain current of the MOSFET, which is different from the downward-pulse signals of the microfluidic sensor in chapter II. Different signals are due to different positions of the gate branch channel. In the current setup for the nanofluidic sensor, the gate branch is close to the positively-biased reservoir, while it is close to the negatively-biased reservoir in the microfluidic sensor. If the reservoir B is connected to the gate of the MOSFET, downward pulses will be also sensed when nanoparticles are passing through the sensing channel.

The relative modulation of the gate voltage can be derived as

$$\frac{\Delta V_G}{V_G} = \frac{V_G^* - V_G}{V_G} = \frac{V_+}{V_G} \cdot \frac{R_A \Delta R}{(R_A + R + R_D)(R_A + R + \Delta R + R_D)}. \tag{3.5}$$

Since $\Delta R << (R_A + R + R_D)$, the above equation can be simplified as

$$\frac{\Delta V_G}{V_G} = \frac{V_G^* - V_G}{V_G} = \frac{V_+}{V_G} \cdot \frac{R_A R}{(R_A + R + R_D)^2} \cdot \frac{\Delta R}{R}. \tag{3.6}$$

In the experiments, the MOSFET is biased in the sub-threshold regime because we would like to use the higher amplification. Similar to Eq. (2.9), we can derive the theoretical drain current modulation for the nanofluidic sensor as

$$\frac{\Delta I_D}{I_D} = (\frac{qV_G}{kT} - \frac{V_G}{2\psi_S}) \cdot \frac{d\psi_S}{dV_G} \cdot \frac{V_+}{V_G} \cdot \frac{R_A R}{(R_A + R + R_D)^2} \cdot \frac{\Delta R}{R}. \tag{3.7}$$

According to Eq. (3.7), the channel resistance modulation can be amplified by two factors. One is the amplification factor from the MOSFET when working in the sub-threshold regime as

$$A_M = (\frac{qV_G}{kT} - \frac{V_G}{2\psi_S}) \cdot \frac{d\psi_S}{dV_G} . \quad (3.8)$$

The other is the amplification factor from the fluidic device and can be defined by

$$A_F = \frac{\Delta V_G / V_G}{\Delta R / R} = \frac{V_+}{V_G} \cdot \frac{R_A R}{(R_A + R + R_D)^2} . \quad (3.9)$$

The amplification factor, A_M, depends on the gate potential of the MOSFET, which can be tuned by adjusting the applied voltage V_+. The amplification factor, A_F, can be maximized by tuning the design of the nanofluidic device, which will be discussed in the section 'Discussion'.

Detection of Nanoparticles

Figure 3.5 shows the recorded MOSFET drain current when 210 nm-diameter fluorescent nanoparticles are passing through the sensing nanochannel. The transmission image of the sensing channel overlaid with the fluorescent image of nanoparticles is shown in Fig. 3.6, which is taken with an inverted fluorescent microscope. In this experiment, V_+ is set as 3.8 V and V_{DS} is set as 0.15 V. As seen in Fig. 3.5, each upward peak indicates one particle flowing through the nanochannel, as verified by the concurrent optical observation. The baseline drain current of the MOSFET is around 0.78 μA and the gate voltage inferred from the I_D-V_G curve is ~ 1.08 V. MOSFET is working in the sub-threshold regime. Figure 3.5 shows that the signals incurred by different particles are not identical and the relative modulation of the MOSFET drain current is in the range from 4.5% to 6.5%. The height difference of

upward peaks may be due to the intrinsic size distribution of the nanoparticles. Different surface charges of different nanoparticles may also affect the signal strength and more thorough experiments need to be performed to clarify this effect. The volume

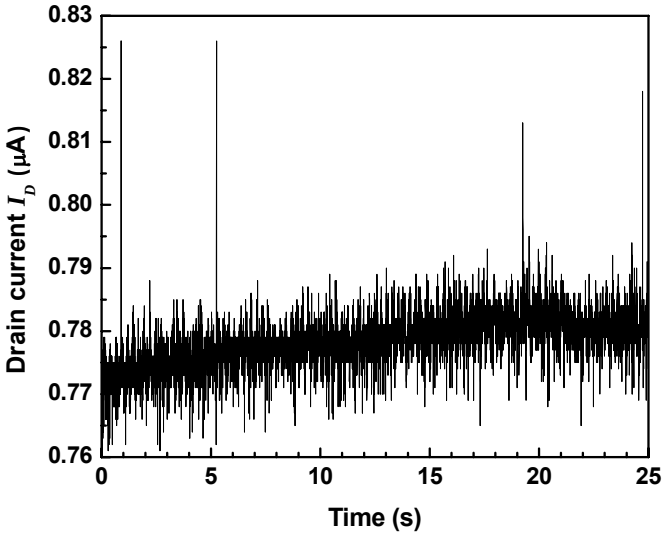

Figure 3.5 Drain current of the MOSFET recorded for a suspension containing 210 nm in diameter fluorescent nanoparticles. MOSFET is working in the sub-threshold regime.

ratio of a 210 nm-diameter nanoparticle to the sensing channel (5 μm long with a cross section of 500 nm by 500 nm) is ~ 0.4% and therefore a total amplification factor of 11-15 has been achieved. The noise level of the measured MOSFET drain current in Fig. 3.5 is relatively high, ~ 2.5% of the baseline signal, since we mounted the fluidic device under a microscope and only shielded the MOSFET part with a faraday cage. Note that the result reported above is just some preliminary test for the first-batch nanofluidic devices and the amplification factor (11-15) is relatively small compared to what we have

achieved with the microfluidic sensor (40-80). We will discuss how to improve the performance of the nanofluidic sensor in the next section.

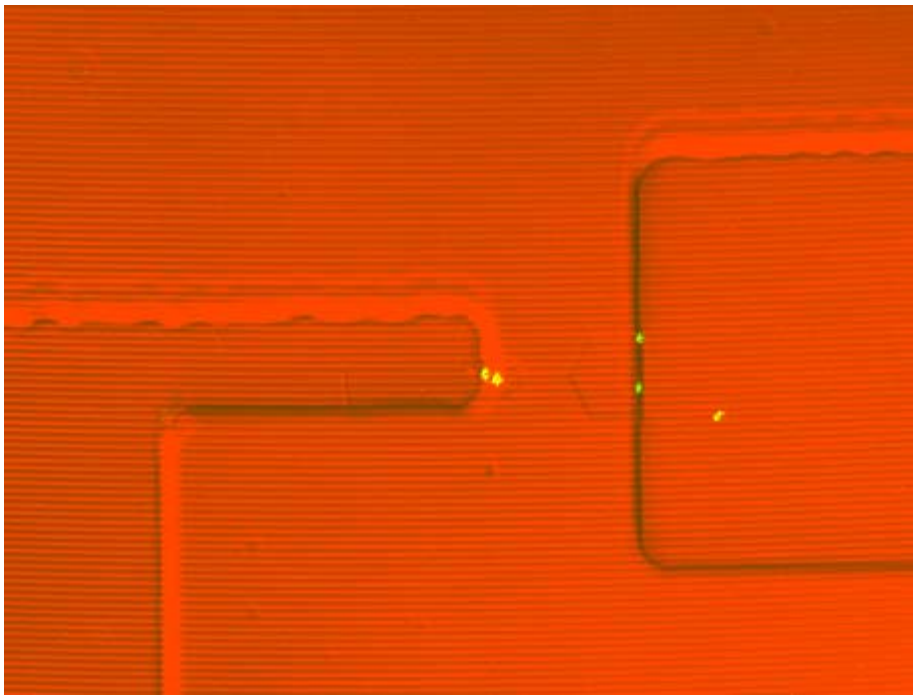

Figure 3.6 Overlay of the transmission image of the sensing nanochannel and the fluorescence image of nanoparticles taken with an inverted fluorescent microscope

Discussion

As mentioned in the section 'Design and Fabrication of the Nanofluidic Device', one difficulty we had during the characterization process of the nanofluidic sensor is how to deliver nanoparticles through the sensing channel. It was found that it was very difficult to deliver plain polystyrene nanoparticles by electroosmotic flow partially due to the low flow rate restrained by the nanochannel. On the other hand, the polystyrene particles inherently have negative surface charges. When applying an electrical field

along the fluidic channel, the electrostatic force acting on a nanoparticle is in the opposite direction of the electroosmotic flow and two transport mechanisms may cancel each other under certain conditions. In our current experiments, we rely on nanoparticles with high negative surface charges and deliver the nanoparticles through the sensing channel by electrophoretic motion. Meanwhile, due to the high surface charges, only a small applied voltage can be used for V_+, ~ 3.8 V for the current device, which limits the amplification factor of the fluidic device as seen in Eq. (3.6). If a better condition is found to deliver nanoparticles and a much high electrical bias can be applied across the fluidic channel, the performance of the nanofluidic sensor will be much better. Another factor is that a nanoparticle with high surface charges will attract a layer of counter-ions near its surface and as a result will bring more ions into the sensing channel, which may increase the channel conductance and reduce the signal strength from the resistive pulse sensing. In order to investigate the effect of surface charges on the resistive pulse sensing signal, electrolytic solutions with different concentrations should be used to prepare the particle suspension and also be used in all tests.

Due to the difficulty of delivering nanoparticles through the nanofluidic device, at the current stage, we conducted all the experiments under an inverted fluorescent microscope in order to visualize the particle motion. The noise level of the MOSFET drain current signal is high since the fluidic device is not shielded by a faraday cage. Once the particle delivery problem is well studied, we can shield the whole experimental setup into a faraday cage and may be able to achieve better sensing results by reducing

the noise to a very low level.

According to Eq. (3.9), the amplification factor from the nanofluidic device not only depends on the applied electrical bias V_+ but also depends on the resistance ratio $R_A R/(R_A + R + R_D)^2$. The dimension of the sensing nanochannel and then its resistance R, will rely on the diameter of the analyzed particles and can be treated as constants. In order to maximize the amplification factor, the resistances of the three segments of the horizontal channel in Fig. 3.4 should satisfy the following condition:

$$R_A = R + R_D, \tag{3.10}$$

which can be achieved by carefully designing the dimensions of the nanochannel and microchannels.

In summary, following tests could be conducted in future research to improve the performance of the nanofluidic sensor:

1) Search for better conditions to deliver plain polystyrene nanoparticles or particles with lower surface charges and increase the applied electrical bias;
2) Investigate the effect of surface charges on the resistive pulse sensing signal with different concentration buffer solutions;
3) Shield both the fluidic device and the MOSFET with a faraday cage to reduce the electrical noise;
4) Maximize the amplification factor of the fluidic circuit by carefully designing the dimensions of the nanofluidic device to satisfy the condition $R_A = R + R_D$.

Summary

We developed a nanofluidic sensor for the detection of nanoparticles based on the new sensing scheme. Fluorescent nanoparticles with high negative surface charges are translocated through the fluidic channels by the electrophoretic migration. All the experiments are conducted under an inverted fluorescent microscope in order to visualize the translocation of nanoparticles. Preliminary results show that a 210 nm-diameter nanoparticle can be detected by using a device with a sensing channel of 5 μm in length, 500 nm in width, and also 500 nm in depth. Future research plans are proposed to further improve the sensitivity of the nanofluidic sensor.

CHAPTER IV

MOLECULAR DYNAMICS SIMULATIONS OF ION AND WATER DISTRIBUTION IN NANOCHANNELS

As discussed in the introduction section, many issues in nanofluidics require fundamental understanding of the interactions among ions, fluid, surface charges, and macromolecules such as DNA segments in highly confined nano-environments. For example, in the experiments of detecting DNA molecules with nanofluidic sensors, both ionic current enhancement and blockade events were observed depending on the concentration of the electrolyte. The ionic current blockade is expected from the Coulter principle. The ionic current enhancement at low electrolytic concentration is normally attributed to the channel conductance increase because of the additional mobile counter ions adsorbed on the negatively charged DNA molecules. However, the crossover from ionic current enhancement to blockade occurred at different electrolytic concentrations in different experiments (~ 0.79 M in Fan et al., 2005; 0.4 M in Smeets et al., 2006), indicating that complex charge interactions inside the nanochannel may not be fully reflected with the simple models presented in the literature. In this chapter, molecular dynamics (MD) study of the ion and water distribution in nanochannels is presented. Three issues have been examined: one is the effect of ion-water interaction potentials on the simulation of ion distribution in nanochannels; another is the

fundamental problem in molecular dynamics simulations, i.e. concentrations of counter- and co-ions in nanochannels corresponding to a certain bulk electrolyte; and the last one is the effect of the surface charge density on the ion and water distribution near a charged surface. This chapter first gives a brief introduction to the molecular dynamics simulation method and then presents the detailed simulation results.

Molecular Dynamics Simulation Method

Molecular dynamics is a deterministic method that reveals the equilibrium and dynamical properties of a system by monitoring the motion of each molecule in the system under certain intermolecular potentials. Molecular dynamics simulation method can be divided into two classes: (i) classical molecular dynamics and (ii) *ab initio* molecular dynamics. Classical molecular dynamics treats molecules as point masses and the interactions between molecules are represented by simple potential functions, which are based on the empirical data or from independent quantum mechanical calculations. The so-called *ab initio* molecular dynamics unifies the classical molecular dynamics and density-function theory, and takes into account the electronic structure when calculating the forces on the atomic nuclei. Only a brief introduction to the classical molecular dynamics simulation method, which is used in this dissertation, will be given in this section.

In a molecular dynamics simulation, an atomic or molecular system is first constructed and its initial state is specified in terms of positions and velocities of the

constituent atoms or molecules. The interactions among atoms or molecules are simulated by a model potential that should obey the fundamental laws of physics and chemistry and grasp the important feature of the intermolecular interactions that determine the property of interest. Starting from the initial set-up of the system with the given intermolecular potentials, Newton's equations of motion are integrated for each atom or molecule to calculate the positions and velocities of atoms or molecules in the system as time propagates. After the system reaches equilibrium, the properties of the model system can be extracted from the motion of the atoms or molecules using statistical mechanics methods.

Equations of Motion

For a system composed of N atoms, after constructing the initial microscopic state by specifying the positions and momenta of all atoms under certain constrains such as the given total energy and volume, the behavior of the system is fully determined by the classical equations of motion for the atoms

$$m_i \ddot{\mathbf{r}}_i = \mathbf{f}_i , \tag{4.1}$$

$$\mathbf{f}_i = -\frac{\partial V}{\partial \mathbf{r}_i} , \tag{4.2}$$

where m_i and $\mathbf{r}_i$ are the mass and Cartesian coordinates of atom i; $\mathbf{f}_i$ represents the total force acting on atom i by all other atoms in the system and can be derived from the potential energy function $V(r_1, r_2, \cdots, r_N)$.

Interaction Potential

A set of realistic intermolecular potentials are arguably the most important part of a successful molecular dynamics simulation. For a simple atomic system, the potential energy can be written in terms of the coordinates of individual atoms, atom pairs, and atom triplets etc (Allen & Tildesley, 1989):

$$V(r_1, r_2, \cdots, r_N) = \sum_i v_1(r_i) + \sum_i \sum_{j>i} v_2(r_i, r_j) + \sum_i \sum_{j>i} \sum_{k>j>i} v_3(r_i, r_j, r_k) + \cdots. \quad (4.3)$$

The notation $\sum_i$ in the first term indicates a summation over all atoms in the system and $v_1(r_i)$ represents the potential in an external force field. The second term, usually called the pair potential, is probably the most important energy term in a molecular dynamics simulation. The pair potential sums over all distinct atom pairs *i* and *j* without counting any pair twice. The function $v_2(r_i, r_j)$ depends only on the separation between atoms *i* and *j* and hence can also be expressed as $v_2(r_{ij})$. The three-body and other multi-body potentials are normally avoided in a molecular dynamics simulation since they are difficult to implement and could be extremely time consuming. The multi-body effects are usually taken into account by modifying the pair potential, i.e. using an 'effective' pair potential, which is not the exact interaction potential between the two atoms. According to the range of the interactions, the pair potential can be divided into two categories, i.e., short-range interaction potentials and long-range interaction potentials. Different algorithms are adopted to treat the short-range and long-range interaction potentials.

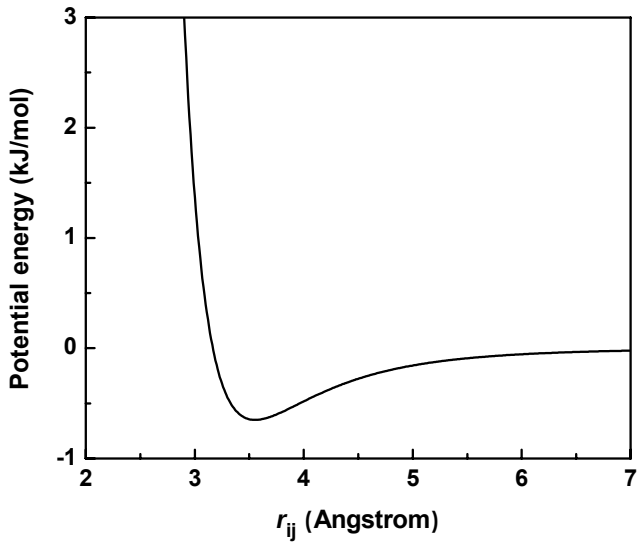

Figure 4.1 The Lennard-Jones interaction potential

A. Short-Range Interaction Potentials

Short-range interaction potentials denote those interactions that attenuate rapidly as the distance between two atoms increases. The most commonly used short-range interaction potential is the Lennard-Jones 12-6 potential (as shown in Fig. 4.1)

$$v_2^{LJ}(r_{ij}) = 4\varepsilon_{ij}\left[\left(\frac{\sigma_{ij}}{r_{ij}}\right)^{12} - \left(\frac{\sigma_{ij}}{r_{ij}}\right)^{6}\right]. \tag{4.4}$$

Lennard-Jones potential includes a strongly repelling term proportional to $1/r_{ij}^{12}$, which represents the excluded volume by an atom, and a long attractive tail of the form $-1/r_{ij}^{6}$, which models the effect of attractive interactions between induced dipoles due to fluctuating charge distributions. The parameters σ_{ij} and ε_{ij}, the effective diameter and the depth of the potential well between different atoms, can be calculated by using the

combination rules since normally the effective diameter and the depth of the potential well are only available for the atoms of a single element. The most frequently used combination rule is the Lorentz-Berthelot formula

$$\sigma_{ij} = \frac{\sigma_{ii} + \sigma_{jj}}{2}. \tag{4.5}$$

$$\varepsilon_{ij} = \sqrt{\varepsilon_{ii}\varepsilon_{jj}}. \tag{4.6}$$

In a molecular dynamics simulation, it takes a double loop to calculate the potential energy or force and the time for this calculation is proportional to N^2, which is the most time-consuming and computationally expensive part in the simulation and limits the speed of the program execution. For short-range interactions, since the potential value drops to zero very rapidly as the distance increases, it is a common practice to restrict the evaluation of the interaction potential to a limited region of space. A cutoff radius, R_c, is usually introduced, beyond which the interaction potential is set to zero. The common choice is $R_c = 2.5\sigma_{\max}$, where $\sigma_{\max}$ is the maximum value of the effective diameters for all atom pairs in the system.

The cutoff radius approach reduces the computation time significantly since the potential/force calculations are skipped for those atoms that are not in the cutoff sphere. However, the separations of all distinct pairs still have to be calculated at each time step to examine if they are in the interaction range or not, which also takes a lot of time. The situation gets worse rapidly for larger system since this calculation scales with N^2. In order to solve this problem, Verlet introduced a technique in 1967 (Verlet, 1967) and the

strategy is to construct a neighbor list for each atom, which stores the indices of all neighbor atoms falling in the sphere with a radius of $R_c + R_s$. Here R_s is called skin radius. Therefore, in a force routine, not all atoms but only those in the neighbor list will be tested to see if they are in the range $r_{ij} < R_c$. The neighbor list is reconstructed as less frequently as possible but have to be done before any unlisted atoms come into the interaction region.

B. Long-Range Interaction Potentials

Long-range interaction potentials denote those interactions that attenuate slowly as the distance between the atoms increases. A very common long-range interaction potential is the Coulomb potential, which scales as $1/r_{ij}$. Therefore, for a system containing ions or polarizable molecules such as water, the Coulomb potential must be taken into account for all atoms in the system and can be expressed by

$$v^C = \frac{1}{2}\sum_{i \neq j} \frac{q_i q_j}{|\mathbf{r}_{ij}|}, \tag{4.7}$$

where q_i and q_j are charges on atoms *i* and *j*, respectively.

The trouble with long-range interaction potentials is not only the time-consuming calculation over all atom pairs in the simulation system, but also comes from the fact that when simulating bulk liquids with a small system, periodic boundary conditions must be used to avoid the surface effects. The simulation box is replicated throughout the space to form an infinite lattice. During a simulation, when an atom moves out of the central

box, its periodic images in other replicated boxes move exactly in the same way. In this case, not only the long-range interactions among the atoms in the central box but also those between the atoms in the central box and the image atoms in all replicated boxes must be taken into account in the Coulomb potential calculation. Therefore, a lattice sum has to be calculated as

$$v^C = \frac{1}{2}\sum_{\mathbf{n}}{}' \sum_{i,j=1}^{N} \frac{q_i q_j}{\left|\mathbf{r}_{ij} - \mathbf{n}L\right|}, \tag{4.8}$$

where $\mathbf{n}$ is a lattice vector and L is the length of the simulation box which is assumed to be cubic here. The prime on the first summation means $i \neq j$ for $\mathbf{n} = 0$. It is known that the above lattice sum is only conditionally convergent and the result depends on the summation order. Different techniques have been developed in the literature to overcome this difficulty, which can be classified into three categories (Gibbon & Sutmann, 2002): (i) Ewald summation method, (ii) Particle-mesh method, and (iii) Multipole method. Ewald summation method is adopted in this work and will be briefly described here.

The basic idea of Ewald summation is to break the lattice sum in Eq. (4.8) into two parts: (i) a short-range interaction potential that can be treated with a simple cutoff scheme, and (ii) a long-range interaction potential that is periodic, slowly varying, and can be represented to an acceptable accuracy by a finite Fourier series. The strategy is to construct a cloud of screening charge of opposite polarity so that each charge in the system is screened by this charge cloud, which makes the electrostatic potential due to the

charge at position $\mathbf{r}_i$ decay rapidly to nearly zero at a short prescribed distance. This approach makes the potential of this composite charge distribution a short-range interaction and can be calculated in the real space. The screening charges are compensated using a smoothly varying periodic charge density that can be summed up in the reciprocal Fourier space. The final form of the Ewald summation can be written as (Gibbon & Sutmann, 2002)

$$v^C = \frac{1}{2}\left[\sum_{\mathbf{n}}{}' \sum_{i,j=1}^{N} \frac{q_i q_j \, erfc(\alpha|\mathbf{r}_{ij} - \mathbf{n}L|)}{|\mathbf{r}_{ij} - \mathbf{n}L|} + \frac{4\pi}{L^3} \sum_{\mathbf{k}\neq 0} \sum_{i,j=1}^{N} \frac{q_i q_j}{|\mathbf{k}|^2} e^{-|\mathbf{k}|^2/4\alpha^2} e^{i\mathbf{k}\mathbf{r}_{ij}} - \frac{2\alpha}{\sqrt{\pi}} \sum_{i=1}^{N} q_i^2 \right]. \quad (4.9)$$

Integration Algorithm

From the initial configuration and the given potential functions, the equations of motion can be integrated using finite difference methods. The integration algorithm, which is normally called the integrator, must be accurate since it determines the accuracy of the simulation results. However, no integration algorithm can provide an exact solution due to the round-off error of the finite number representation and the finite difference scheme. The integrator must be accurate in the sense of approximating the true trajectory of the system as closely as possible, which requires the use of a short time step. On the other hand, the integrator also has to pursue the use of a long time step δt for the computing efficiency. Therefore, there is a tradeoff between accuracy and efficiency when selecting the integration time step.

The most widely used integration algorithm for the equations of motion is the Verlet

algorithm, including the original scheme, the leap-frog scheme, and the velocity Verlet algorithm. They are essentially equivalent and the leap-frog scheme is adopted in this work and can be given as

$$\mathbf{v}(t+\frac{1}{2}\delta t) = \mathbf{v}(t-\frac{1}{2}\delta t) + \delta t \cdot \mathbf{a}(t), \tag{4.10}$$

$$\mathbf{r}(t+\delta t) = \mathbf{r}(t) + \delta t \cdot \mathbf{v}(t+\frac{1}{2}\delta t), \tag{4.11}$$

where $\mathbf{r}$, $\mathbf{v}$, and $\mathbf{a}$ are the position, velocity, and acceleration vectors, respectively. In this scheme, the stored quantities are the current position, $\mathbf{r}(t)$, acceleration, $\mathbf{a}(t)$, and the half-step velocity, $\mathbf{v}(t-\frac{1}{2}\delta t)$. In order to calculate the kinetic energy at time *t*, the current velocity may be calculated by

$$\mathbf{v}(t) = \frac{1}{2}\left[\mathbf{v}(t+\frac{1}{2}\delta t) + v(t-\frac{1}{2}\delta t)\right]. \tag{4.12}$$

Statistical Ensemble

If there is no time dependent external force, dynamics of a molecular system will evolve on a constant-energy surface. Therefore, the natural choice of the statistical ensemble in molecular dynamics simulation is the microcanonical ensemble (NVE). Other types of ensembles, such as the canonical ensemble (NVT) and the isothermal-isobaric ensemble (NPT), can also be realized by controlling corresponding thermodynamic variables. For the last two ensembles, the temperature of the ensemble needs to be controlled and four different control mechanisms, namely differential control, proportional control, integral control, and stochastic control have been developed in the

literature (Sutmann, G. 2002). A proportional thermostat for the NVT ensemble, which is used in this dissertation, will be briefly discussed as follows.

In order to correct the deviation of the actual system temperature from the prescribed one, T_0, Berendsen et al. (1984) introduced a proportional method in which the system is weakly coupled to an external heat bath and at each time step, the velocities of the atoms in the system are multiplied by a scaling factor

$$\lambda = \left[1 + \frac{\delta t}{\tau}\left(\frac{T_0}{T} - 1\right)\right]^{\frac{1}{2}}. \tag{4.13}$$

In this way, the kinetic energy of the system is scaled and the temperature of the system is forced to approach the prescribed temperature. The coupling time constant, τ, represents the time scale in which the system reaches the prescribed temperature. For a larger τ, it takes a longer time for a system to reach the desired temperature. Using the Berendsen thermostat, the system temperature is allowed to fluctuate instead of being set as a constant. At each time step, the temperature is corrected to a value closer to T_0.

Effect of Ion-Water Interaction Potentials on Ion Distribution in Nanochannels

Molecular dynamics has been proved to be a powerful tool to investigate the ion and fluid transport in nanochannels. One critical issue in molecular dynamics is the selection of the interaction potentials between different molecules and the accuracy of the results highly depends on the extent of how the selected interaction potentials are able to mimic the real system in the simulation. While molecular dynamics has been used to

study water for a long time and the numerous models for water molecules have converged to several most common potentials (Jorgensen, 1983), the inclusion of ions in the water and simulation of electric double layer happened only recently and the potential to represent ion-water interactions is still in discussion.

In this dissertation, we applied two different ion-water interaction potentials to study their effects in molecular dynamics simulations of ion distribution in the nanochannel between two parallel charged surfaces. One potential is based on the simple Lennard-Jones potential, which is widely used in most literature on this topic, and the other is Bounds' potential (Bounds, 1985), which is adopted to explore the hydration effects. Bounds' potential is based on *ab initio* calculations for ion-TIP4P water complexes and takes into account the structure of the hydrated shells around the ion. The details of Bounds' potential will be given in the next section.

Molecular Dynamics Simulation Details

Molecular dynamics simulations were conducted for the model system consisting of a slab of sodium chloride solution sandwiched by two parallel silicon plates. Figure 4.2 shows a schematic diagram of the molecular system under investigation. Each wall is composed of four layers of silicon atoms (totally 512 atoms) oriented in the <100> direction. The silicon atoms are fixed to their original positions during the simulation. The system contains 2008 water molecules, 84 sodium ions, and 36 chlorine ions. Total negative surface charges of 48 units of elementary charge are uniformly distributed on the

two innermost layers of silicon atoms, giving a surface charge density of -0.2 C/m^2. Similar to the former work in the literature, the selection of the numbers of counter-ions, co-ions, and surface charges meets the requirement of overall charge neutrality of the system. The channel width L_z, defined as the distance between the two innermost layers, is 3.18 nm. The dimensions of the simulation box in the x and y directions are L_x=4.34 nm and L_y=4.34 nm, respectively. For the coordinate system chosen in Fig. 4.2, z =0 corresponds to the innermost layer of the lower channel wall.

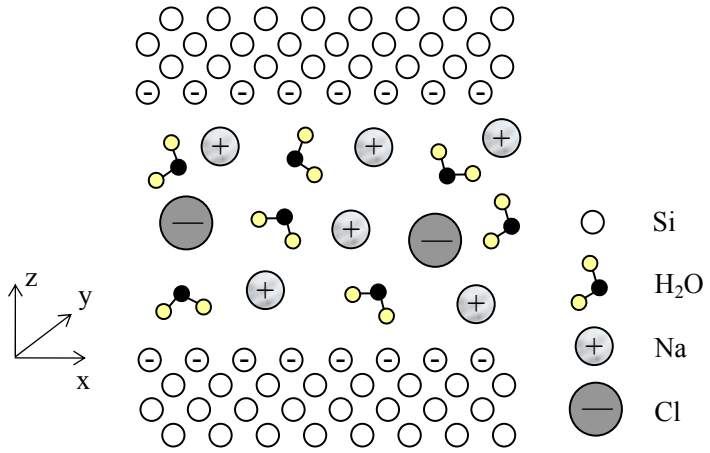

Figure 4.2 Schematic diagram of the molecular system under investigation. The silicon atoms in each plate are oriented in <100> direction.

Equilibrium molecular dynamics simulations are performed with a parallel replicated data program modified from a code that has been used to model the hydration structure of water and ions confined between mica surfaces (Leng & Cummings, 2005; Leng & Cummings, 2006). For one case, the most widely adopted force field is used,

i.e., the intermolecular interactions are expressed as a sum of the Lennard-Jones potential and the electrostatic potential. Both TIP4P (Jorgensen, 1983) and SPC/E ((Berendsen et al., 1987)) models are used in this case to simulate the water molecules. For the other case, Bounds' potential is adopted to calculate the interactions between ions and TIP4P water molecules to compare with the results based on the simple Lennard-Jones potential. A SETTLE algorithm (Miyamoto & Kollman, 1992) is adopted to maintain the geometry water molecules.

Table 4.1 Lennard-Jones potential parameters $\phi^{LJ}(r)=E/r^{12}-D/r^{6}$

Atom pair	D (kcal Å^6/mol)	E (kcal Å^{12}/mol)	σ (Å)
O-O^T	610.0	6.0×10^5	3.15
O-O^S	625.8	6.3×10^5	3.17
O-Na	103.8	5.6×10^4	2.86
O-Cl	1436.7	4.0×10^6	3.75
O-Si	1484.5	1.8×10^6	3.27
Na-Na	17.2	5.0×10^3	2.57
Na-Cl	238.4	3.6×10^5	3.39
Na-Si	246.4	1.6×10^5	2.95
Cl-Cl	3298.3	2.6×10^7	4.45
Cl-Si	3408.2	1.2×10^7	3.88

^{T} stands for TIP4P model. ^{S} stands for SPC/E model.

For the former case, the Lennard-Jones potential is considered for any atom pair except those pairs including hydrogen atom and the Si-Si pair. The parameters for the Lennard-Jones potential are the same as those used by Qiao and Aluru (2003) and listed in Table 4.1. The electrostatic interactions between all the charges in the system

(including mobile ions, charged sites in TIP4P or SPC/E water molecules, and surface charges) are calculated by using the Ewald summation algorithm with the slab correction (Yeh & Berkowitz, 1999).

In Bounds' model, the van der Waals interaction between the sodium ion and the water molecule is represented by the sum of sodium–hydrogen soft repulsion

$$\phi_{\mathrm{NaH}}(r) = A_{\mathrm{NaH}} \exp(-b_{\mathrm{NaH}} r), \tag{4.14}$$

and sodium-oxygen attractive-repulsive interaction

$$\phi_{\mathrm{NaO}}(r) = A_{\mathrm{NaO}} \exp(-b_{\mathrm{NaO}} r) - C_{\mathrm{NaO}} / r^4 - D_{\mathrm{NaO}} / r^6 . \tag{4.15}$$

Bounds' potential for the chlorine-water molecule interaction consists of an exponential repulsion and an induction type term for the chlorine-oxygen interaction

$$\phi_{\mathrm{ClO}}(r) = A_{\mathrm{ClO}} \exp(-b_{\mathrm{ClO}} r) - C_{\mathrm{ClO}} / r^4 , \tag{4.16}$$

together with a Morse potential between chlorine and hydrogen

$$\phi_{\mathrm{ClH}}(r) = A_{\mathrm{ClH}} \exp[-b_{\mathrm{ClH}} (r - R_{\mathrm{e}})] \{\exp[-b_{\mathrm{ClH}} (r - R_{\mathrm{e}})] - 2\} . \tag{4.17}$$

Table 4.2 Parameters* for Bounds' potential (Symbol I represents Na or Cl)

	A_{IO}	b_{IO}	C_{IO}	D_{IO}	A_{IH}	b_{IH}	R_{e}
Na	27343.0	3.5455	435.0	-840.0	2064.0	3.394	—
Cl	8025.0	2.151	361.0	—	1.2	2.8	2.22

* The values in this table give the potential in kcal/mol if r is in Å.

The parameters in Bounds' potential are summarized in Table 4.2. The electrostatic

interactions between all the charges in the system (including mobile ions, charged sites in TIP4P water molecules, and surface charges) are also calculated by the Ewald summation algorithm with the slab correction.

The equations of motion are integrated by using a leap-frog algorithm with a time step of 2.0 fs. The temperature of the system is maintained at 298 K by using a Berendsen thermostat (Berendsen et al., 1984) with a time constant of 0.1 ps. A cutoff radius of 11 Å is used for the calculation of the Lennard-Jones potential and the electrostatic potential in the real space. Starting from a random configuration, the system is allowed to reach equilibrium for 1 ns. A production run of 4 ns is then followed to gather the statistically converged results. The ion and water concentration profiles are obtained by using the binning method. All the modeling has been done on the central computing facilities at Vanderbilt University, which is a computer cluster consisting of over 1500 processors running Linux. Our parallel code used 8 nodes with an improved performance of 5.8 times compared with the serial version of the code.

Ion and Water Distribution across the Nanochannel

Figure 4.3 shows the ion and water concentration profiles across the nanochannel obtained by using TIP4P model to simulate water molecules and the Lennard-Jones potential to model the ion-water interaction. Water concentration is only uniform in the center of the channel and a layering effect of water molecules near the channel wall is observed, which has been well reported in the literature (for example, Mattke & Kecke,

1998; Spohr, 1999; Freund, 2002; Qiao & Aluru, 2003). This feature is normally attributed to the non-electrostatic interactions between the solid atoms and water molecules and exists no matter if the surface is charged or not. A sharp peak occurs in the concentration profile of sodium ions at a position 3.66 Å away from the silicon wall. The peak value is 23.6 M and the peak width is about 3 Å. There is no chlorine ion within 2.86 Å from the channel wall. In the central region of the channel, the concentration of chlorine ions is almost the same as that of sodium ions, which is consistent with the classical Poisson-Boltzmann prediction. SPC/E model is also used to simulate water molecules for this case. The result is similar to Fig. 4.3, as shown in Fig. 4.4.

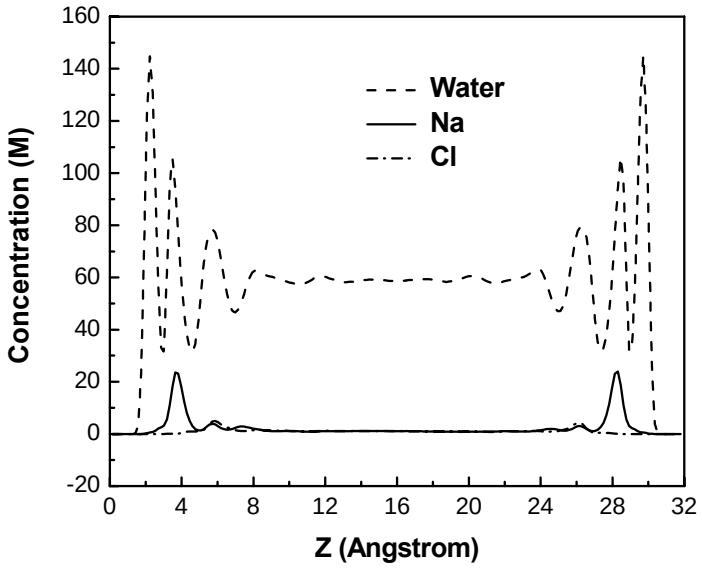

Figure 4.3 Ion and water concentration profiles across the nanochannel. The ion-water interaction is calculated with the Lennard-Jones potential and the water model is TIP4P.

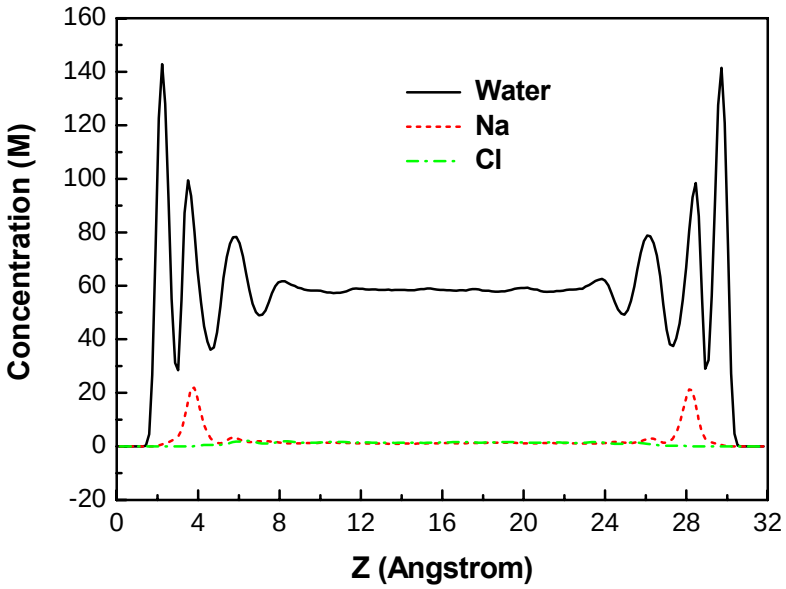

Figure 4.4 Ion and water concentration profiles across the nanochannel. The ion-water interaction is calculated with the Lennard-Jones potential and the water model is SPC/E.

Figure 4.5 shows the ion and water concentration profiles across the nanochannel obtained from Bounds' potential. The water model is TIP4P. The water concentration profile is in general similar to the Lennard-Jones case. However, the second water concentration peak is lower than the third peak, which is not expected and contradicts to the common understanding. The ion distribution in the nanochannel deviates from that obtained with the Lennard-Jones potential in several aspects: (i) The sodium concentration peak is located at 7.47 Å away from the wall, and the peak value and width are 11.47 M and 6 Å respectively. This peak is farther from the wall and much lower and wider compared with that in Fig. 4.3. (ii) In the region 10.8 Å away from the channel wall, the concentration of chlorine ions is higher than that of sodium ions; that is

to say, charge inversion occurs in the central region of the nanochannel, which is completely contradictory to the Poisson-Boltzmann prediction.

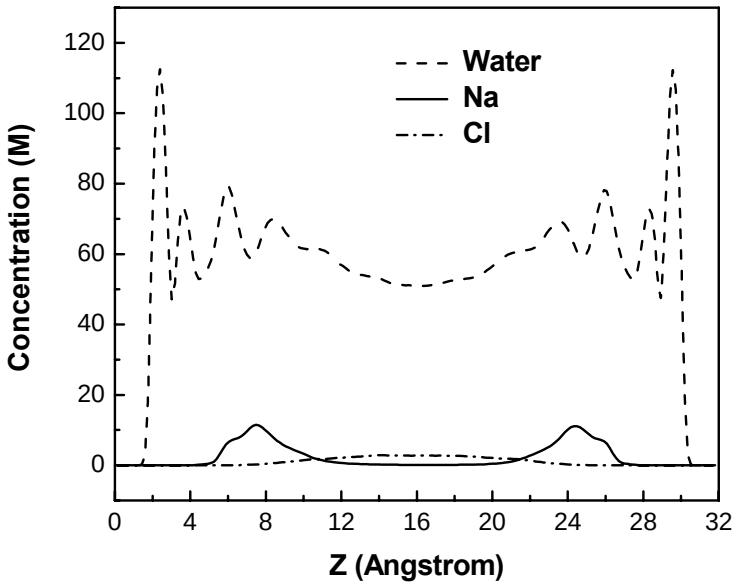

Figure 4.5 Ion and water concentration profiles across the nanochannel. Bounds' potential is used to calculate the ion-water interaction. The water model is TIP4P.

Observation (i) can be understood as follows. Since Bounds' potential takes into account the hydration effect, each sodium ion is actually surrounded by several water molecules. The strong interactions between the sodium ion and water molecules prevent the ion from moving towards the channel wall, so the peak location is significantly away from the channel wall. On the other hand, the diameter of hydrated ions is larger compared with bare ions, which means that the hydrated ions can't be packed very closely, so the peak value in Fig. 4.5 is much lower than Fig. 4.3 and the peak width is wider. As to the observation (ii), charge inversion phenomenon has been

explained by the finite size of ions (Greberg & Kjellander, 1998) and the discreteness of water molecules (Qiao & Aluru, 2004) in the literature. It is noticed that the sodium ion concentration in the channel center is almost zero in Fig. 4.5, which is caused by the subtle balance between ion-wall interactions and ion-water interactions. The charge inversion in our case may also be related to the depletion of sodium ions in the channel center.

Although it is not clear yet whether the Lennard-Jones potential or the Bound's potential is more accurate for the molecular dynamics simulation of ion distribution in the nanochannel, the current work presents the possibility that the ion-water interaction potentials could greatly affect the ion distribution thus electroosmotic flow in nanochannels. In the following works, Lennard-Jones potential is adopted to simulate ion and water interactions since it is the most commonly used potential in similar works in the literature. In addition, the ion distribution results obtained by using Lennard-Jones potential as the ion-water interaction potential are more consistent with the results predicted by continuum theories.

Ion Distribution in Nanochannels

Ion distribution in nanochannels has been extensively studied in recent years by using the molecular dynamics simulation method (Mattke & Kecke, 1998; Spohr, 1999; Spohr, 2002; Freund, 2002; Spohr, 2003; Qiao & Aluru, 2003; Zhu et al., 2005; Qiao & Aluru, 2004; Qiao & Aluru, 2005). While a common drawback in the above works is

that the number of counter-ions and co-ions in the simulation system is assigned somewhat arbitrarily as discussed in the introduction section. In this section, a three-region simulation system is adopted to attack this fundamental problem.

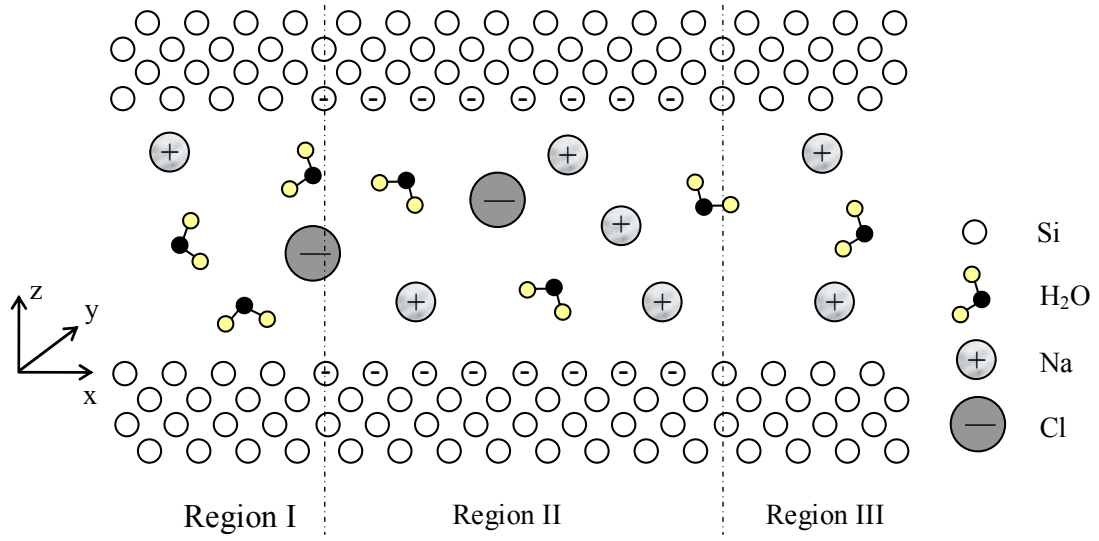

Figure 4.6 Schematic diagram of the simulation domain, which includes three regions: no surface charge and electric double layer exist in Regions I and III so the electrolyte in these regions represents bulk solution. Negative surface charges are presented in Region II, leading to electric double layers in this region.

Three-Region Simulation Domain

A schematic of the simulation domain is shown in Fig. 4.6, which also consists of a slab of sodium chloride solution confined between two parallel silicon plates. The simulation domain is divided into three regions and for regions I and III, no surface charge is assigned to the silicon wall. Therefore, no electric double layer will form in these two regions and the solution can be treated as "bulk" as long as our interest is the

structure of the electric double layer, which is induced by surface charges. In region II, however, silicon atoms on the innermost layers of the top and bottom plates are partially charged with a given surface charge density, leading to electric double layers in this region. The overall electrical neutrality is satisfied by keeping a balance of cations, anions and surface charges in the whole simulation system. In this way, when the system reaches equilibrium, the concentrations of counter-ions and co-ions in the nanochannel region, as well as the concentration of the bulk region emerge naturally.

Molecular Dynamics Simulation Details

Each silicon plate is composed of four layers of silicon atoms (totally 1024) oriented in the <100> direction. The position of silicon atoms is given according to the silicon crystal structure. The silicon atoms in the lower plate are kept fixed during the simulation and the upper silicon plate can move in the z-direction to maintain the pressure in the simulation system to be 0.1 MPa. For the coordinate system chosen in Fig. 4.6, z =0 corresponds to the innermost layer of the lower plate. Periodic boundary conditions are applied in the x and y directions. The dimensions of the simulation box are L_x=8.69 nm, L_y=4.34 nm, and L_z=4.34 nm, respectively.

Equilibrium molecular dynamics simulations are performed to investigate the ion distribution in nanochannels. Water is modeled with the SPC/E model. SETTLE algorithm is also used to maintain the geometry of rigid water molecules. The intermolecular interactions are calculated as the sum of the Lennard-Jones potential and

the electrostatic potential. The parameters for the Lennard-Jones potential are listed in Table 4.1 and electrostatic interactions between all charges in the system (including mobile ions, O and H atoms in water molecules, and surface charges) are calculated using the Ewald summation algorithm with the slab correction (Yeh & Berkowitz, 1999). The equations of motion are integrated using the leap-frog algorithm with a time step of 2.0 fs. The temperature of the system is maintained at 298 K using a Berendsen thermostat with a time constant of 0.1 ps. Starting from a random configuration, the molecular system is allowed to equilibrate for 1 ns and a production run of 2 ns is followed to gather the statistically converged results. Table 4.3 summarizes the two cases examined in this study for ion concentration and distribution profile in nanochannels with two different surface charge densities.

Table 4.3 List of the simulated cases for ion distribution in nanochannels

Case #	σ_s (C/m^2)	# of Water	# of Na^+	# of Cl^-
1	-0.2034	4016	140	92
2	-0.2882	4016	152	84

Ion and Water Distribution in Bulk Region

The ion and water concentration profiles in the bulk region for case 1 are shown in Fig. 4.7, which is representative for both cases in the bulk region. The water concentration oscillation is still observed near the silicon plate since the layering effect is

due to the non-electrostatic interactions between the solid wall and water molecules. The concentration profiles of Na^+ and Cl^- ions in the bulk region almost coincide with each other, indicating the same concentration everywhere, as expected for the bulk electrolyte.

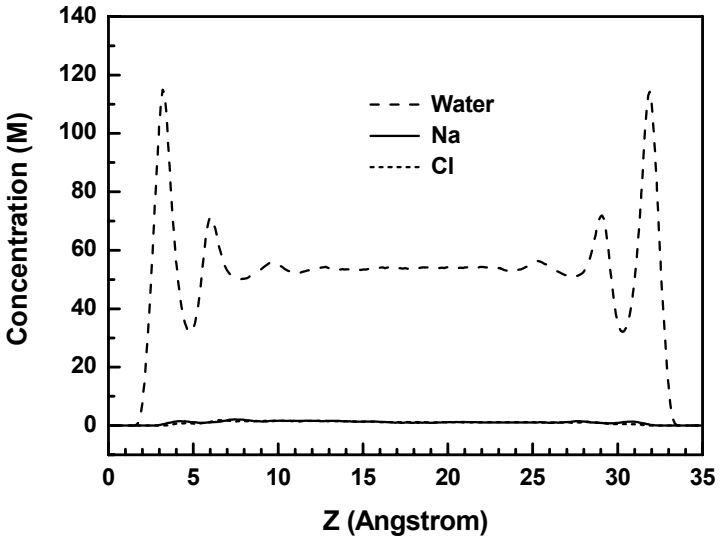

Figure 4.7 Ion and water concentration profiles in the bulk region for case 1.

Ion Distribution in the Nanochannel

Figure 4.8 (a) shows the ion concentration profiles in the central nanochannel region with a surface charge density of -0.2034 C/m^2 (case 1). The concentration profile of the co-ions (Cl^-) in this region is similar to that in the bulk region (see Fig. 4.7), while the concentration profile of the counter-ions (Na^+) is significantly different from the bulk result because of the electric double layer. A pronounced peak of Na^+ ion concentration occurs at a position of 3.80 Å away from the channel wall as a result of the Na^+-silicon

wall and Na^+-water interactions. A very weak second peak of Na^+ concentration is observed at a position of 5.70 Å away from the channel wall.

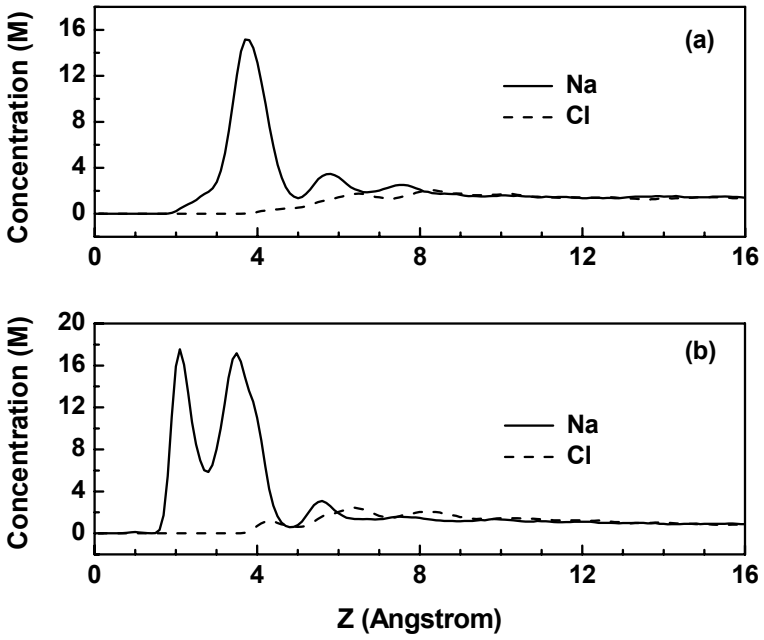

Figure 4.8 Ion concentration profiles in the nanochannel for case 1 (a) and case 2 (b).

Figure 4.8 (b) shows the ion concentration profiles in the central nanochannel with a surface charge density of -0.2882 C/m^2 (case 2). Different from case 1, two distinct peaks are observed for Na^+ ion concentration, i.e., a first peak at 2.10 Å and a second peak at 3.50 Å away from the channel wall. The double peak phenomenon is not predicted by the classical electric double layer theory, but has been observed in several molecular dynamic simulations (Spohr, 2002; Mattke & Kecke, 1998; Qiao & Aluru, 2003; Qiao & Aluru, 2004; Qiao & Aluru, 2005). We believe that it is due to the fact

that under high surface charge density, one layer of Na^+ ions are dehydrated and adsorbed onto the negatively charged solid wall, which forms the inner Helmholtz plane. The second peak is formed by hydrated Na^+ ions, which corresponds to the outer Helmholtz plane.

Table 4.4 Numbers of ions and water molecules in the three regions

Case #	Regions	# of Water	# of Na^+	# of Cl^-
1	I + III	1946.76	56.16	52.68
	II	2069.24	83.84	39.32
2	I + III	1929.81	51.00	46.95
	II	2086.19	101.00	37.05

Average Ion Concentrations in Bulk and Nanochannel Regions

The ion concentration profiles in the nanochannel with charged surfaces are similar to those reported in the literature, while the overall ion concentrations in the central nanochannel region and the bulk region reveal more interesting information. The statistical numbers of counter-ions and co-ions and water molecules in the bulk and central nanochannel regions are given in Table 4.4. While the numbers of Na^+ and Cl^- ions in the bulk region are very close to each other, it is interesting to note that for both cases the number of Na^+ ions in the bulk region (region I+III) is slightly (less than 10%) larger than the number of Cl^- ions. This feature may be due to the statistical error or it may be related to some other factors, which needs further investigation. In the central

nanochannel region, neither the number of Na^+ ions nor that of Cl^- ions is close to those in the bulk region. Using the dimensions of the simulation box, the average ion concentrations in the bulk and central nanochannel regions are calculated as shown in Table 4.5.

Table 4.5 Average ion concentrations in the bulk and nanochannel regions. C_{Na^+} and C_{Cl^-} represent the concentrations of Na^+ and Cl^- ions in the nanochannel.

Case #	C_{bulk} (M)	C_{Na^+} (M)	C_{Cl^-} (M)
1	1.37	2.11	0.99
2	1.23	2.54	0.93

The bulk concentrations are calculated with the average numbers of Na^+ and Cl^- ions in regions I and III. Table 4.5 clearly shows that because of the presence of electric double layers, the concentrations of both counter-ions and co-ions can be significantly different from the bulk electrolyte, which indicates that it might not be correct to take the co-ion concentration as the bulk electrolyte concentration, as practiced in the literature. A three-region simulation domain including bulk electrolyte on each side of the nanochannel can provide the ion concentration in nanochannels with charged surfaces corresponding to a certain bulk concentration. This work addresses the fundamental issue of ion number selection in molecular dynamics simulations of electric double layers, which can be important for modeling electroosmotic flow and macromolecule

translocation through a nanochannel.

Effect of Surface Charge Densities on the Ion and Water Distribution near the Charged Surfaces

The structure of water at the solid and liquid interface attracted significant research interests in the past decades. It is believed that the structure of water within a few nanometers of a solid surface determines the wetting properties, i.e., hydrophobicity or hydrophilicity, and other solid-liquid interfacial properties such as solute adsorption, dielectric properties, and so on. In this section, a series of molecular dynamics simulations are performed to study the effect of surface charge densities on the ion and water structures close to a charged surface. Results show that surface charges not only interact with mobile ions in the electrolyte, but also interact with water molecules due to their polar nature, and hence influence the orientation and structure of water molecules in the near wall region.

Simulation Details

The schematic diagram of the molecular system under investigation in this work is similar to the system shown in Fig. 4.2. The system consists of sodium ions, chloride ions, and water molecules confined in two parallel silicon plates. Each silicon plate is composed of four layers of silicon atoms oriented in either <100> or <111> direction. The position of each atom is given according to the silicon crystal structure. The

schematic of the (100) Si plates is shown in Fig. 4.2, for which each layer contains 128 atoms and the simulation box is a cube with an edge length of 4.34 nm. While for the (111) Si plates, there are 154 atoms in each layer and the dimensions of the simulation box are L_x=4.66 nm, L_y=4.22 nm, and L_z=4.22 nm, respectively. During the simulation, the silicon atoms in the lower plate are kept fixed, while the upper silicon plate is allowed to move in z-direction to maintain the pressure in the simulation system to be 0.1 MPa. Surface charges (if any) are evenly distributed among the innermost silicon layers as shown in Fig. 4.2. z=0 corresponds to the innermost layer of the lower silicon plate and periodic boundary conditions are applied in both the x and y directions.

Table 4.6 List of the simulated cases for the (100) silicon surface

Case	σ_s (C/m^2)	# of water	# of Na	# of Cl
1	0	2008	36	36
2	-0.0508	2008	48	36
3	-0.1017	2008	60	36
4	-0.1525	2008	72	36
5	-0.2034	2008	84	36

Ion and Water Structures near the (100) Silicon Surface

In order to investigate the effect of surface charge densities on the ion and water structures near a charged (100) silicon surface, five cases are simulated in this work as summarized in Table 4.6. In all cases, the molecular system includes 2008 water molecules and the number of chloride ions is kept as 36. The surface charge density is

different for each case and the number of sodium ions is adjusted correspondingly to guarantee the overall charge neutrality of the simulation system. Starting from a random configuration, the molecular system is allowed to equilibrate for 1 ns and a production run of 3 ns is followed to gather the statistically converged results.

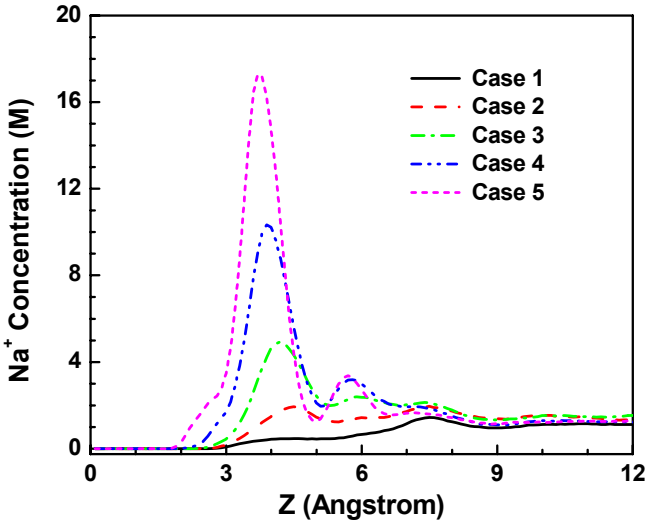

Figure 4.9 Na^+ concentration profiles near the lower (100) silicon plate.

The counter-ion (Na^+) distribution profiles near the lower (100) silicon plate are shown in Fig. 4.9 for the five cases listed in Table 4.6. For all five cases, the co-ion concentration profiles are very similar to the concentration profile of Na^+ ions in the case of no surface charge (Case 1, solid line in Fig. 4.9) and are not presented here. As shown in Fig. 4.9, if there is no surface charge on the silicon plate (Case 1), sodium ions tend to stay away from the solid wall as evidenced by the fact that the concentration of Na^+ ions in the near wall region (Z<7Å) is smaller than the bulk concentration in the

central region of the channel (~ 1 M). If the silicon plate is negatively charged, however, counter-ions accumulate near the charged wall due to the electrostatic interactions between surface charges and counter-ions. In this case, a Na^+-concentration peak is developed within 5 Å from the charged (100) silicon wall. With the increase of the surface charge density ($|\sigma_s|$), the position of the Na^+-concentration peak shifts towards the charged silicon plate and the height of the concentration peak gets larger. For example, when the surface charge density is -0.2034 C/m^2 (Case 5), the sodium concentration can be as high as 17.3 M at a position of 3.7 Å away from the silicon plate. The above phenomena are expected as the electrostatic interaction between surface charges and sodium ions is stronger when the surface charge density is higher and more counter-ions are attracted to the near wall region to shield surface charges. In addition, for all cases, sodium ions are depleted in the region within 2 Å from the silicon surface due to the finite sizes of silicon and sodium atoms and the sodium concentrations in the central region are almost the same for all the cases.

The water density profiles near the lower (100) silicon plates are shown in Fig. 4.10 for the cases with different surface charge densities. In addition to the well-understood layering effect, we observe from Fig. 4.10 that as the negative surface charge density increases, water molecules move further towards the charged (100) silicon surface due to the electrostatic interactions between surface charges and water molecules. More interestingly, for cases 3, 4, 5, the water molecules within ~ 5 Å from the charged surface evolve from one layer into two layers because of the electrostatic interaction between

surfaces charges and water molecules. To our knowledge, this extra water layer due to the effect of surface charges has not been reported for the silicon surfaces yet. Experimental results have been reported in the literature (Cheng et al., 2001) for interfacial water adjacent to a mica surface, which show an additional layer of water molecules. Two layers of water molecules are observed within 4 Å from the mica surface in their experiments and they claimed that the first layer is the adsorbed water layer and the second one is the hydrated water layer. One difference between their experimental results and our simulation results is that the density peak height of the first water layer is smaller than that of the second layer in their experiments, while it is larger than the height of second water density peak in our simulation results. The reason for

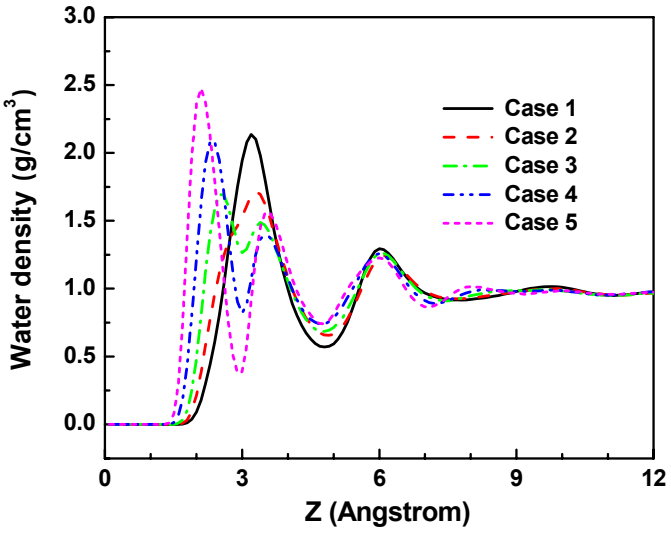

Figure 4.10 Water density profiles near the lower (100) silicon plate

the above discrepancy is not clear yet, but it may be related to the different structures between the mica surface and the (100) silicon surface.

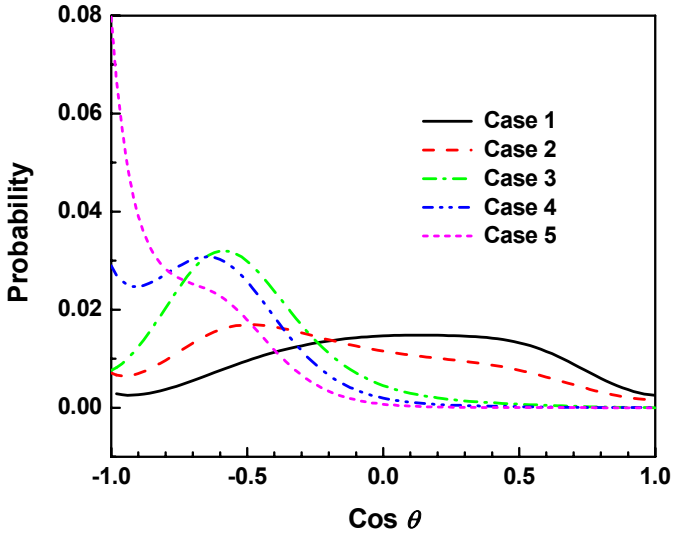

Figure 4.11 The orientation of water molecules in the first layer close to the lower (100) silicon plate. θ is the angle between the normal of the lower plate and the water dipole momentum.

To further understand the water structure in the near wall region, the statistical results of the orientation of water molecules in the first layer close to the lower (100) silicon plate are presented in Fig. 4.11 for all five cases. θ is the angle between the normal vector of the lower plate and the dipole momentum of a water molecule. Comparing Fig. 4.10 and Fig. 4.11, we believe that when the surface charge density is low (Case 1 and 2), the water molecules near the charged silicon plate are more randomly oriented as evidenced by the broad distribution of $\cos\theta$ from -0.9 to +0.9 and form a thick layer of water molecules. However, for cases with higher surface charge densities (Case

3, 4, and 5), the strong electrostatic interaction between surface charges and hydrogen/oxygen atoms leads to more aligned water molecules with hydrogen atoms facing the silicon plate ($\cos\theta < 0.0$ as shown in Fig. 4.11), which helps to split the water molecules into two distinct layers. This layering effect may have important implications to the electroosmotic flow through nanochannels since the extra water layer may affect the viscosity of the fluid in the near wall region. It may also affect the heat transfer between the silicon surface and the liquid.

It is worth noting that the above phenomenon was not observed in the similar work with the (111) silicon plate in the literature (Qiao & Aluru, 2004), while the surface charge density in their work was similar to those in our cases for the (100) silicon surface. To examine if the difference is due to the different numerical schemes used in their work, we also examined the ion and water distribution near the (111) silicon surface with similar surface charge densities with those in Table 4.6 for a (100) silicon surface.

Ion and Water Structures near the (111) Silicon Surface

Three cases were simulated to investigate the effect of surface charge densities on the ion and water structures near the (111) Si surface as listed in Table 4.7. For all the cases, the molecular system contains 2008 water molecules and 36 chloride ions. The numbers of sodium ions in Case 2 and Case 3 are slightly different from those cases with similar surface charge densities (Case 3 and Case 5, respectively) in Table 4.6 since the surface area of (111) silicon plates are larger than (100) silicon plates and more

counter-ions are needed to keep the whole system electrically neutral. The molecular system was allowed to equilibrate for 1 ns and a production run of 4 ns was followed to extract the ion and water distribution profiles across the nanochannel.

Table 4.7 List of the simulated cases for the (111) silicon surface

Case	σ_s (C/m^2)	# of water	# of Na	# of Cl
1	0	2008	36	36
2	-0.1058	2008	62	36
3	-0.2034	2008	86	36

The counter-ion (Na^+) distribution profiles near the lower (111) silicon plate are shown in Fig. 4.12 for the three cases listed in Table 4.7. The co-ion (Cl^-) concentration profiles for all three cases are similar to the sodium concentration profile for Case 1 and are not given here. Similar to the results for (100) silicon plates, when the surface is negatively charged, the counter-ions (Na^+) move towards the charged (111) silicon surface and a remarkable concentration peak is formed within 5 Å from the wall. For the case with a higher surface charge density ($|\sigma_s|$), the position of the Na^+-concentration peak is closer to the silicon plate and the peak value is also larger. When the surface charge density is -0.2034 C/m^2 (Case 3), the sodium concentration profile shows a peak of 22.5 M at a position of 4.1 Å away from the silicon plate. Compared to the case with the same surface charge density (-0.2034 C/m^2, Case 5 in Fig. 4.9) for (100) silicon surfaces, we notice that the sodium ion layer formed near a (111) surface is thinner than

the counterpart close to a (100) surface and therefore the peak is higher correspondingly, which may be related to the different water structures near two kinds of surfaces as shown later.

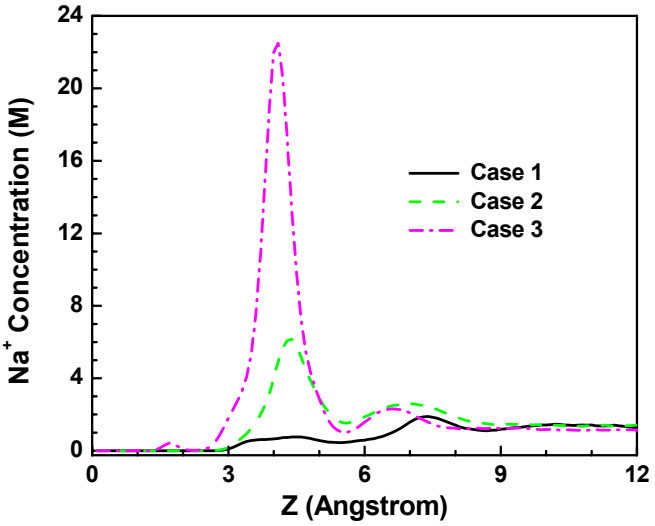

Figure 4.12 Counter-ion (Na^+) concentration profiles near the (111) silicon plate.

The water density profiles near the lower (111) silicon plate are shown in Fig. 4.13 for the three cases listed in Table 4.7. Water molecules also move further towards the (111) silicon plates with the increase of the surface charge density due to the electrostatic interaction between surface charges and water molecules. However, different from the results for charged (100) silicon surfaces, no extra water layer is observed near a (111) silicon surface when surface charge density is high, which is consistent with the previously reported work in the literature (Qiao & Aluru, 2004). Instead, a much wider valley between the first and second water layers is formed for the case with a surface

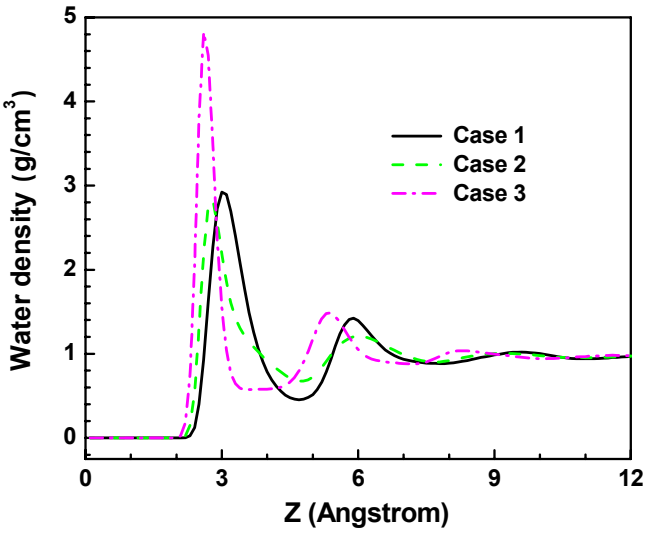

Figure 4.13 Water density profiles near the (111) silicon plate

charge density of -0.2034 C/m^2. It is well-known that the water density valley is energetically favorable for accommodating the ions, which explains why the counter-ions are confined in the region between 3 Å and 5 Å from the wall and form a thin layer. While for the (100) silicon surface, the water density valley is much narrower due to the extra water layer and the counter-ions could not only be accommodated in the water density valley but also in the region close to peaks. The statistics of the orientation of water molecules in the first layer close to the (111) silicon surface is given in Fig. 4.14. Comparing Fig. 4.11 and Fig. 4.14, it is clearly shown that the orientation of water molecules near a charged (111) silicon surface is more randomly distributed than the orientation of water molecules near a charged (100) silicon surface. It can be attributed to the weaker electrostatic interaction between surface charges and water molecules near the (111) silicon surface since water molecules stay farther away from the silicon surface

as evidenced by the larger distance between the water density peak and the wall in Fig. 4.13.

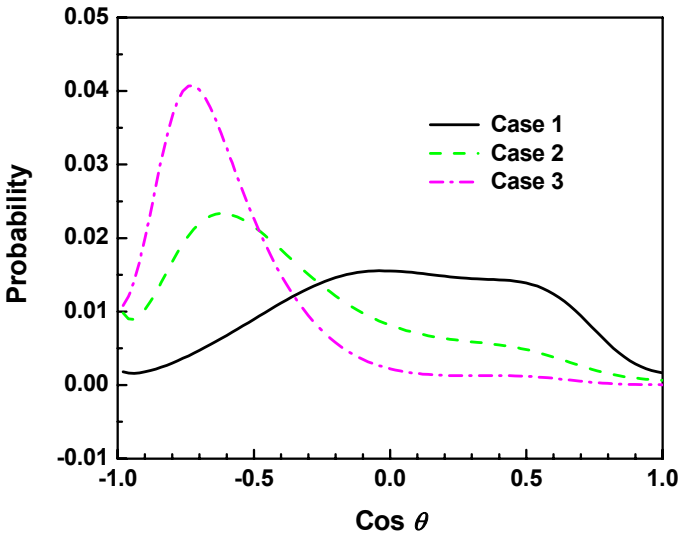

Figure 4.14 The orientation of water molecules in the first layer close to the (111) silicon plate.

Different water structures near the charged (100) and (111) silicon surfaces may be related to the different surface atom densities of these two kinds of surfaces. The atom density of a (100) silicon surface is ~ 6.80 atom/nm^2, while it is around 7.83 atom/nm^2 for a (111) silicon surface. Therefore, silicon atoms are less densely packed on a (100) silicon surface and contain more cavities than a (111) silicon surface. Those cavities are favorable to form the adsorbed water layer when water molecules are attracted to the near wall region under high surface charge density. However, densely packed silicon atoms on a (111) silicon surface tend to repel the water molecule away from the wall and no

adsorbed water layer is formed in the near wall region even under a very high surface charge density.

Summary

In summary, equilibrium molecular dynamics simulations have been performed to study ion and water distribution in nanochannels. First, the effect of ion-water interaction potentials on the ion distribution in a nanochannel is investigated and results show that Lennard-Jones potential and Bounds' potential could generate very different ion distribution profiles in the nanochannel. A fundamental problem in the molecular dynamics simulation, i.e. the selection of the number of counter-ions and co-ions in the nanochannel, is also studied with a three-region simulation domain. The counter-ion and co-ion concentration and distribution in the nanochannel with electric double layers are obtained corresponding to a bulk electrolyte of known concentration. It is shown that both the counter-ion and co-ion concentration in the nanochannel could be significantly different from that of the bulk electrolyte. This approach is in contrast to the common practice in the literature where the ion numbers in the nanochannel are assigned somewhat arbitrarily and corresponding to an unknown bulk concentration.

The effects of surface charge densities on the ion and water structures near the charged (100) and (111) silicon surfaces are also examined in this chapter. It is shown that, under high surface charge densities, the water molecules within ~ 5 Å from the charged (100) silicon surface can be split from one layer into two layers due to the strong

electrostatic interaction between surfaces charges and water molecules, while this phenomenon is not observed for the (111) silicon surface consistent with the results reported in the literature. This layering effect may have important implications to the electroosmotic flow through nanochannels since the extra water layer may affect the viscosity of the fluid in the near wall region. It may also affect the heat transfer between the silicon surface and the liquid.

CHAPTER V

CONCLUSIONS

A new sensing scheme has been developed in this work by integrating a fluidic circuit and a MOSFET and detecting particles by measuring the drain current of the MOSFET. This new sensing scheme has been implemented at the microscale level and a MOSFET-based microfluidic sensor with PDMS microchannels has been fabricated to detect various micron-sized particles. The amplification effects from the fluidic circuit and the MOSFET have been demonstrated both theoretically and experimentally. The lowest volume ratio detected is 0.006%, 10 times lower than the detection limit based on the traditional resistive pulse sensors as reported in the literature. The device sensitivity has been characterized as the function of the MOSFET gate potential and the applied electrical bias across the fluidic circuit. It is shown that the sensitivity is higher when the MOSFET is operating in sub-threshold regime than in the saturation regime. Moreover, we demonstrated that the device is capable to distinguish particles of similar sizes but different surface charges. By integrating with the fluorescence detection system, the device can also be used to determine the percentage of the cells tagged with a specific fluorescence dye.

The same sensing scheme is also implemented at the nanoscale and a nanofluidic sensor is developed for the detection of nanoparticles. Fluorescent nanoparticles with

high negative surface charges are translocated through the fluidic channels by the electrophoretic migration. Preliminary results show that a 210 nm-diameter nanoparticle can be detected by using a device with a sensing channel of 5 μm in length, 500 nm in width, and also 500 nm in depth. Future research plans are proposed to further improve the sensitivity of the nanofluidic sensor.

To understand the fundamental phenomena occurring at the solid-liquid interface or in nanochannels, equilibrium molecular dynamics simulations have been performed to investigate the ion concentration and distribution in nanochannels with a three-region simulation domain. The counter-ion and co-ion concentrations and distributions in the nanochannel with electric double layers are obtained corresponding to a bulk electrolyte of known concentration. It is shown that both the counter-ion and co-ion concentrations in the nanochannel could be significantly different from that of the bulk electrolyte. This approach is in sharp contrast to the common practice in the literature where the ion numbers in the nanochannel are assigned somewhat arbitrarily and corresponding to an unknown bulk concentration.

The effects of surface charge densities on the ion and water structures near the charged (100) and (111) silicon surfaces are examined. It is shown that under high surface charge densities, the water molecules within ~ 5 Å from the charged (100) silicon surface can be split from one layer into two layers due to the strong electrostatic interaction between surface charges and water molecules, while this phenomenon is not observed for the (111) silicon surface, consistent with that reported in the literature.

Different water structures near the charged (100) and (111) silicon surfaces may be related to the different surface atom densities of these two different surfaces. This extra layer effect indicates that not only the surface charge density, but also the atomic density of the solid surface can affect the ion and water structures in the near wall region.

REFERENCES

Allen, M.P., Tildesley, D.J. 1989. *Computer simulation of liquids* pp. 7. Oxford University Press, New York

Bayley, H., Martin, C.R. 2000. Resistive-pulse sensing—from microbes to molecules. *Chem. Rev.* **100**:2575-2594

Bayley, H., Cremer, P.S. 2001. Stochastic sensors inspired by biology. *Nature* **413**:226-230

Beckman Coulter, Inc. 2007. http://www.beckman.com/products/instrument/partChar/pc_multisizer3.asp

Behrens, S.H., Grier, D.G. 2001. The charge of glass and silica surfaces. *J. Chem. Phys.* **115**:6716-6721

Berendsen, H.J.C., Postma, J.P.M., van Gunsteren, W.F., DiNola, A., Haak, J.R. 1984. Molecular dynamics with coupling to an external bath. *J. Chem. Phys.* **81**:3684-3690

Berendsen, H.J.C., Grigera, J.R., Straatsma, T.P. 1987. The missing term in effective pair potentials. *J. Phys. Chem.* **91**:6269-6271

Berge, L.I., Feder, J., Jøssang, T. 1989. A novel method to study single-particle dynamics by the resistive pulse technique. *Rev. Sci. Instrum.* **60**:2756-2763

Bezrukov, S.M. 2000. Ion Channels as Molecular Coulter counters to probe metabolite transport. *J. Membrane Biol.* **174**:1-13

Bezrukov, S.M., Vodyanoy, I., Parsegian, V.A. 1994. Counting polymers moving through a single ion channel. *Nature* **370**:279-281

Bounds, D.G. 1985. A molecular dynamics study of the structure of water around the ions Li^+, Na^+, K^+, Ca^{++}, Ni^{++} and Cl^-. *Molec. Phys.* **54**:1335-1355

Bunville, L.G. 1984. Commercial instrumentation for particle size analysis. *In*: Modern Methods of Particle Size Analysis. Barth, H.G., editor. pp. 1-42. John Wiley, New York

Carbonaro, A., Sohn, L.L. 2005. A resistive-pulse sensor chip for multianalyte immunoassays. *Lab Chip* **5**:1155-1160

Casey, H.C. 1999. *Devices for integrated circuits: silicon and III-V compound semiconductors* pp. 353 & 385. Wiley, New York

Chang, H., Kosari, F., Andreadakis, G., Alam, M.A., Vasmatzis, G., Bashir, R. 2004. DNA-mediated fluctuations in ionic current through silicon oxide nanopore channels. *Nano Lett.* **4**:1551-1556

Chen, P., Mitsui, T., Farmer, D.B., Golovchenko, J., Gordon, R.G., Branton, D. 2004. Atomic layer deposition to fine-tune the surface properties and diameters of fabricated nanopores. *Nano Lett.* **4**:1333-1337

Chen, P., Gu, J., Brandin, E., Kim, Y.-R., Wang, Q., Branton, D. 2004. Probing single DNA molecule transport using fabricated nanopores. *Nano Lett.* **4**:2293-2298

Cheng, L., Fenter, P., Nagy, K.L., Schlegel, M.L., Sturchio, N.C. 2001. Molecular-scale density oscillations in water adjacent to a mica surface. *Phys. Rev. Lett.* **87**:156103

Coulter, W.H. 1953. Means for counting particles suspended in a fluid. U.S. Patent No. 2,656,508, issued 20 Oct. 1953

Coulter, W.H. 1956. High speed automatic blood cell counter and cell size analyzer. *Proc. Natl. Electron. Conf.* **12**:1034-1040

Deamer, D.W., Akeson, M. 2000. Nanopores and nucleic acids: prospects for ultrarapid sequencing. *Trends Biotechnol.* **18**:147-151

DeBlois, R.W., Bean, C.P. 1970. Counting and sizing of submicron particles by the resistive pulse technique. *Rev. Sci. Instrum.* **41**:909-916

DeBlois, R.W., Wesley, R.K.A. 1977. Sizes and concentrations of several type C oncornaviruses and Bacteriophage T2 by the resistive-pulse technique. *J. Virol.* **23**:227-233

Duffy, D.C., McDonald, J.C., Schueller, J.A., Whitesides G.M. 1998. Rapid prototyping of microfluidic systems in poly(dimethylsiloxane). *Anal. Chem.* **70**:4974-4984

Fan, R., Karnik, R., Yue, M., Li, D., Majumdar, A., Yang, P. 2005. DNA translocation in inorganic nanotubes. *Nano Lett.* **5**:1633-1637

Fologea, D., Gershow, M., Ledden, B., McNabb, D.S., Golovchenko, J.A., Li, J. 2005. Detecting single stranded DNA with a solid state nanopore. *Nano Lett.* **5**:1905-1909

Freund, J.B. 2002. Electro-osmosis in a nanometer-scale channel studied by atomistic simulation. *J. Chem. Phys.* **116**:2194-2200

Gibbon, P., Sutmann, G. 2002. Long-range interactions in many-particle simulation. *In*: Quantum simulations of complex many-body systems: from theory to algorithms. Grotendorst, J., Marx, D., Muramatsu, A., editors. vol. 10. pp. 467-506. John von Neumann Institute for Computing, Jülich

Goldberger, J., Fan, R., Yang, P. 2006. Inorganic nanotubes: a novel platform for nanofluidics. *Acc. Chem. Res.* **39**:239-248

Greberg, H., Kjellander, R. 1998. Charge inversion in electric double layers and effects of different sizes for counterions and coions. *J. Chem. Phys.* **108**:2940-2953

Heng, J.B., Ho C., Kim, T., Timp, R., Aksimentiev, A., Grinkova, Y.V., Sligar, S., Schulten, K., Timp, G. 2004. Sizing DNA using a nanometer-diameter pore. *Biophys. J.* **87**:2905-2911

Ito, T., Sun, L., Crooks, R.M. 2003. Simultaneous determination of the size and surface charge of individual nanoparticles using a carbon nanotube-based Coulter counter. *Anal. Chem.* **75**:2399-2406

Ito, T., Sun, L., Henriquez, R.R., Crooks, R.M. 2004. A carbon nanotube-based Coulter nanoparticle counter. *Acc. Chem. Res.* **37**:937-945

Jagtiani, A.V., Zhe, J., Hu, J., Carletta, J. 2006. Detection and counting of micro-scale particles and pollen using a multi-aperture Coulter counter. *Meas. Sci. Technol.* **17**:1706-1714

Jagtiani, A.V., Sawant, R., Zhe, J. 2006. A label-free high throughput resistive-pulse sensor for simultaneous differentiation and measurement of multiple particle-laden analytes. *J. Micromech. Microeng.* **16**:1530-1539

Jorgensen, W.L., Chandrasekhar, J., Madura, J.D., Impey, R.W., Klein, M.L. 1983. Comparison of simple potential functions for simulating liquid water. *J. Chem. Phys.* **79**: 926-935

Karnik, R., Fan, R., Yue, M., Li, D., Yang, P., Majumdar, A. 2005. Electrostatic control of

ions and molecules in nanofluidic transistors. *Nano Lett.* **5**:943-948

Kasianowics, J.J., Brandin, E., Branton, D., Deamer, D.W. 1996. Characterization of individual polynucleotide molecules using a membrane channel. *Proc. Natl. Acad. Sci.* **93**:13770-13773

Kobayashi, Y., Martin, C.R. 1997. Toward a molecular Coulter counter type device. *J. Electroanal. Chem.* **431**:29-33

Koch, M., Evans, A.G.R., Brunnschweiler, A. 1999. Design and fabrication of a micromachined Coulter counter. *J. Micromech. Microeng.* **9**:159-161

Kubitschek, H.E. 1958. Electronic counting and sizing of bacteria. *Nature* **182**:234-235

Larsen, U.D., Blankenstein, G., Branebjerg, J. 1997. Microchip Coulter particle counter. Technical digest, Transducers '97, Chicago, USA, 16-19 June 1997, pp. 1319-1322

Leng, Y.S., Cummings, P.T. 2005. Fluidity of hydration layers nanoconfined between mica surfaces. *Phys. Rev. Lett.* **94**:026101

Leng, Y.S., Cummings, P.T. 2006. Hydration structure of water confined between mica surfaces. *J. Chem. Phys.* **124**:074711

Li, D. 2004. *Electrokinetics in Microfluidics*, vol. 2 of *Interface Science and Technology* pp. 542, Elsevier Academic Press, Amsterdam

Li, J., Stein, D., McMullan, C., Branton, D., Aziz, M.J., Golovchenko, J.A. 2001. *Nature* **412**:166-169

Li, J., Gershow, M., Stein, D., Brandin, E., Golovchenko, J.A. 2003. DNA molecules and configurations in a solid-state nanopore microscope. *Nature Mat.* **2**:611-615

Mattke, T., Kecke, H.-J. 1998. Molecular Dynamics simulations of single, interacting, and sheared double layers-1. Configuration of a double layer. *J. Colloid Interface Sci.* **208**:555-561

Mattke, T., Kecke, H.-J. 1998. Molecular Dynamics simulations of single, interacting, and sheared double layers-2. Influence of system properties, overlap, and shear. *J. Colloid Interface Sci.* **208**:562-569

Meller, A., Branton, D. 2002. Single molecule measurements of DNA transport through a

nanopore. *Electrophoresis* **23**:2583-2591

Meller, A. 2003. Dynamics of polynucleotide transport through nanometer-scale pores. *J. Phys.*: *Condens. Matter* **15**:R581-R607

Miyamoto, S., Kollman, P.A. 1992. SETTLE: an analytical version of the SHAKE and RATTLE algorithm for rigid water models. *J. Comput. Chem.* **13**:952-962

Nakane, J.J., Akeson, M., Marziali, A. 2003. Nanopore sensors for nucleic acid analysis. *J. Phys.*: *Condens. Matter* **15**:R1365-R1393

Peterman, M.C., Ziebarth, J.M., Braha, O., Bayley, H., Fishman, H.A., Bloom, D.M. 2002. Ion channels and lipid bilayer membranes under high potentials using microfabricated apertures. *Biomed. Microdevices* **4**:231-236

Qiao, R., Aluru, N.R. 2003. Ion concentrations and velocity profiles in nanochannel electroosmotic flows. *J. Chem. Phys.* **118**:4692-4701

Qiao, R., Aluru, N.R. 2004. Charge inversion and flow reversal in a nanochannel electro-osmotic flow. *Phys. Rev. Lett.* **92**:198301

Qiao, R., Aluru, N.R. 2005. Atomistic simulation of KCl transport in charged silicon nanochannels: interfacial effects. *Colloids Surf., A* **267**:103-109

Rhee, M., Burns, M.A. 2007. Nanopore sequencing technology: nanopore preparations. *Trends Biotechnol.* **25**:174-181

Rodriguez-Trujillo, R., Mills, C.A., Samitier, J., Gomila, G. 2006. Low cost micro-Coulter counter with hydrodynamic focusing. *Microfluidics and Nanofluidics* **3**:171-176

Saleh, O.A., Sohn, L.L. 2001. Quantitative sensing of nanoscale colloids using a microchip Coulter counter. *Rev. Sci. Instrum.* **72**:4449-4451

Saleh, O.A., Sohn, L.L. 2003. An artificial nanopore for molecular sensing. *Nano Lett.* **3**:37-38

Sikdar, S.K., Webster, S.H. 1980. Coulter particle counting at high counting rates. *J. Phys. E: Sci. Instrum.* **13**:1075-1077

Siwy, Z., Fuliński, A. 2002. Origin of $1/f^{\alpha}$ noise in membrane channel currents. *Phys. Rev. Lett.* **89**:158101

Smeets, R.M.M., Keyser, U.F., Krapf, D., Wu, M.-Y., Dekker, N.H., Dekker C. 2006. Salt dependence of ion transport and DNA translocation through solid-state nanopores. *Nano Lett.* **6**:89-95

Smeets, R.M.M., Keyser, U.F., Wu, M.Y., Dekker, N.H., Dekker, C. 2006. Nanobubbles in solid-state nanopores. *Phys. Rev. Lett.* **97**:088101

Spohr, E. 1999. Molecular simulation of the electrochemical double layer. *Electrochimica Acta* **44**:1697-1705

Spohr, E. 2002. Molecular Dynamics simulations of water and ion dynamics in the electrochemical double layer. *Solid State Ionics* **150**:1-12

Spohr, E. 2003. Some recent trends in computer simulations of aqueous double layers. *Electrochimica Acta* **49**:23-27

Stein, D., Kruithof, M., Dekker, C. 2004. Surface-charge-governed ion transport in nanofluidic channels. *Phys. Rev. Lett.* **93**:035901

Storm, A.J., Storm, C., Chen, J., Zandbergen, H., Joanny, J.-F., Dekker, C. 2005. Fast DNA translocation through a solid-state nanopore. *Nano Lett.* **5**:1193-1197

Sun, L., Crooks, R.M. 2000. Single carbon nanotube membranes: a well-defined model for studying mass transport through nanoporous materials. *J. Am. Chem. Soc.* **122**:12340-12345

Sutmann, G. 2002. Classical molecular dynamics. In lecture notes on *quantum simulations of complex many-body systems: from theory to algorithms*, eds. Grotendorst, J., Marx, D., Muramatsu, A. NIC Series Vol. 10, Julich, pp. 211-254

Sze, S.M. 1981. *Physics of semiconductor devices* 2nd ed. pp. 442 & 446. Wiley, New York

Tabard-Cossa, V., Trivedi, D., Wiggin, M., Jetha, N.N., Marziali, A. 2007. Noise analysis and reduction in solid-state nanopores. *Nanotechnology* **18**: 305505

Verdaguer, A., Sacha, G.M., Bluhm, H., Salmeron, M. 2006. Molecular structure of water

at interfaces: wetting at the nanometer scale," *Chem. Rev.* **106**:1478-1510

Verlet, L. 1967. Computer experiments on classical fluids I, thermodynamical properties of Lennard-Jones molecules. *Phys. Rev.* **159**:98-103

Yeh, I., Berkowitz, M.L. 1999. Ewald summation for systems with slab geometry. *J. Chem. Phys.* **111**:3155-3162

Zhang, Z., Zhe, J., Chandra, S., Hu, J. 2005. An electronic pollen detection method using Coulter counting principle. *Atmos. Environ.* **39**:5446-5453

Zhe, J., Jagtiani, A., Dutta, P., Hu, J., Carletta, J. 2007. A micromachined high throughput Coulter counter for bioparticle detection and counting. *J. Micromech. Microeng.* **17**:304-313

Zhu, W., Singer, S.J., Zheng, Z., Conlisk, A.T. 2005. Electro-osmotic flow of a model electrolyte. *Phys. Rev. E* **71**:041501